LARGE EDDY SIMULATION OF FLOW IN WATER AND WASTEWATER DISINFECTION REACTORS

A Thesis
Presented to
The Academic Faculty

by

Dongjin Kim

In Partial Fulfillment
of the Requirements for the Degree
Doctor of Philosophy in the
School of Civil and Environmental Engineering

Georgia Institute of Technology
August 2011

LARGE EDDY SIMULATION OF FLOW IN WATER AND WASTEWATER DISINFECTION REACTORS

Approved by:

Dr. THORSTEN STOESSER, Advisor
School of Civil and Environmental Engineering
Georgia Institute of Technology

Dr. DONALD R. WEBSTER
School of Civil and Environmental Engineering
Georgia Institute of Technology

Dr. JAEHONG KIM
School of Civil and Environmental Engineering
Georgia Institute of Technology

Dr. SURESH MENON
School of Aerospace Engineering
Georgia Institute of Technology

Dr. PHILIP J. ROBERTS
School of Civil and Environmental Engineering
Georgia Institute of Technology

Date Approved: May 9th, 2011

[To Sara Soyun]

ACKNOWLEDGEMENTS

I would like to thank all the committee members, Dr. Thorsten Stoesser, Dr. Jae-Hong Kim, Dr. Philip J. Roberts, Dr. Donald R. Webster, and Dr. Suresh Menon for their support and advice for my research. Especially, I express my sincere gratitude to my advisor, Dr. Stoesser, for his constant guidance and support. I cannot forget the moment when we first met each other. His kindness and ardor for research immediately captured me. It was my great pleasure to do research with him over the last four years. I also acknowledge my co-advisor, Dr. Jae-Hong Kim, for his extraordinary support. His comments on the drafts for journal papers have improved my writing skills and perception on research. Provision of experimental data by Dooil Kim of Dankook University and Varun Gandhi in Dr. Kim's group is gratefully acknowledged. I am really indebted to my research group, Su-Jin Kim, Sandeep Kumar, Mustafa and Sibel Kara, and Zhuo Chen who shared joys and sorrows with me.

For the consistent prayer and support by Pastor Bong-Su Choi, Sung-Jin Park, Hyung-Seok Seo and Jong-Ho Kim, and church members of the Sugarloaf Korean Baptist Church, I am truly appreciative. Particular thanks to Yánbiān and Kenya-II Mok-Jang members, who have been my local family.

My greatest thanks goes to my lovely wife, Sara Soyun Kil Kim, for her continuous and constant support and love. She gladly brought strong prop to me over the past two years when I was very fatigued. Special thanks to my parents, older brother and sister-in-law, younger brother, grandparents, uncles, aunts, niece and nephew for their steady advocacy and confidence. Warm and tearful affections of parents, two older sisters and their husbands, uncles, aunts, cousins, and three nephews -in-law were devoutly to be grateful for.

Finally, I would like to ascribe this glory to my Lord, God Emmanuel.

TABLE OF CONTENTS

LIST OF TABLES

LIST OF FIGURES

LIST OF SYMBOLS AND ABBREVIATIONS

A	Cell face area; Matrix in linear equations
A_c	Cross sectional area at the inlet sluice gate
a_i and b_i	Weighting constant in low-storage multistage scheme
b	Boundary or source terms in linear equations
C	Coarse grid model
C	Instantaneous tracer concentration; constant of dynamic SGS model
C_i	Instantaneous tracer concentration of i^{th} numerical point
C_{in}	Bulk tracer concentration
C_μ, $C_{1\varepsilon}$, and $C_{2\varepsilon}$	Constants for the standard k-ε model
C_t	Instantaneous tracer concentration at time t
C_s	Smagorinsky constant
CC	Model for coarser grid than C model
$\bar{c}$	The filtered tracer concentration
D	Lower baffle height ; molecular diffusivity
D_t	Turbulent diffusivity
d	Normal distance from a wall
E	Normalized CT of RTD
$E_{\max}$	Peak value of E
F	Fine grid model
F	Cumulative RTD; Flux
f	Integrand

$\overline{G}$	The grid filter function
$\overline{\overline{G}}$	The grid test filter function
H	Water surface level
Hz	Frequency unit, Hertz
h	Sluice gate height
h_R	Hydraulic diameter
k	Turbulent kinetic energy
k_r	Residual kinetic energy
k_s	Roughness length-scale
l	The subgrid scale length
L	Turbulent characteristic length
L_{ij}	Resolved turbulent stress
n	Iteration number (superscript); Maximum nodal point (subscript)
Pe	Peclet number
p or $\overline{p}$	Resolved pressure divided by the density
Q	Volume flow rate; the square of the error for a least square approach
q	Storage for velocity in low storage multistage scheme
Re	Reynolds number
Re_m	Reynolds number based on the channel half-width
ρ	Fluid density
Sc	Molecular Schmidt number
Sc_t	Turbulent Schmidt number
S_{ij}	Filtered strain-rate tensor

$\|S\|$	The characteristic filtered strain rate
T_{10} or t_{10}/τ	Dimensionless time of t_{10}
t	Time
t_f	Time at which the tracer first appears at the outlet
t_p	Time at which the peak concentration of the tracer is observed
t_{10}	Time required for 10% of the tracer injected as a pulse to exit the reactor
t_{90}	Time required for 90% of the tracer injected as a pulse to exit the reactor
t_{HRT} or τ	Theoretical residence time
U	Instantaneous absolute velocity
$\overline{U}$ or $\bar{u}$	Time averaged absolute velocity
U_{bulk} or U_m	Bulk velocity in x direction at the inlet gate
u	Instantaneous velocity component in x direction
u_i and u_j	Instantaneous velocity vector
$\overline{u_i u_j}$	Reynolds stress tensor
$u'u'$	Reynolds stress in x-direction
u_τ and u_*	Wall shear velocity
V	Reactor or chamber volume
$V(abs)$	Instantaneous absolute velocity
v	Instantaneous velocity component in y direction
vm and $\bar{v}$	Time- and spanwise-averaged through-flow velocity
$v'v'$	Reynolds stress in y-direction
w	Instantaneous velocity component in z direction

$w(in)$	Bulk velocity at the inlet of a reactor in z direction
$w(bulk)$	Bulk velocity based on a cross sectional area of each chamber in z direction
W	Baffle spacing
W_e	Effective flow width
x	Spatial position in x direction
x_i	Spatial position vector
$x_{p,j}$	Instantaneous spatial position of particle
y	Spatial position in y direction
y^+	Dimensionless grid space as a boundary condition evaluation factor
z	Spatial position in z direction
Z	Water surface level
$w'w'$	Reynolds stress in z-direction
α_{ij} and β_{ij}	Symbols to represent independent equations for traceless tensors
δ	Channel half-width
δ_{ij}	Kroneker delta
Δ and $\overline{\Delta}$	Anisotropic characteristic filter size
$\overline{\overline{\Delta}}$	Test filter size
Δt	Time step size
Δx , Δy , and Δz	Characteristic filter width in x, y, and z direction
ε	Turbulent dissipation rate
κ	von Karmann constant
μ	Fluid dynamic viscosity
ν	Fluid molecular viscosity

ν_t or $\nu_{t,sgs}$	Sub-grid scale eddy viscosity
π	Mathematical constant approximately equal to 3.14159
ϕ	A scalar quantity in linear equations
θ	Normalized residence time; mean residence time
σ_k and σ_ε	Constants for the standard k-ε model
τ	Theoretical residence time
τ_{ij}	Reynolds stress tensor
τ_{ij}^a	Anisotropic stress tensor
τ_{kk}	Subgrid Scale kinetic energy
τ_w	Wall shear stress
ADI	Alternating direction iteration
CBSMC	Constant Baffle Spacing Multi-Chamber
CDS	Central Differencing Scheme
CFD	Computational Fluid Dynamics
CSTR	Continuous Stirred Tank Reactors
CT	Concentration times residence time
DNS	Direct Numerical Simulations
FDM	Finite Difference Method
FEM	Finite Element Method
FFT	Fast Fourier Transform
FVM	Finite Volume Method
HS	Half Spacing
HLPA	Hybrid Linear/Parabolic Approximation
LES	Large Eddy Simulations

MI	Morill Index
NS	Normal Spacing
PDS	Power Density Spectra
QUICK	Quadratic Upwind Differencing Scheme for Convective Kinetics
RANS	Reynolds Averaged Navier-Stokes
RTD	Residence Time Distribution
SIMPLE	Semi-Implicit Method for Pressure-Linked Equations
SIP	Strong Implicit Procedure
SGS	Sub-Grid Scale
TDMA	Tri-diagonal matrix
3DLIF	Three dimensional laser induced fluorescence
UDS	Upwind Differencing Scheme
VBSM	Variable Baffle Spacing ozone contactor Model

SUMMARY

Hydrodynamic behavior in reactors used for water treatment, particularly in ozone contactors with serpentine flow, is known to strongly affect the process efficiency. However, exact flow characteristics inside these reactors are not well understood, as traditional approach either considers these reactors as black box or relies on less accurate Reynolds-Averaged Navier-Stokes (RANS) simulation. This research aims at (1) providing a better understanding of the hydrodynamics and solute transport phenomena in water and wastewater treatment reactors by employing the Large Eddy Simulation (LES) method, (2) assessing the accuracy and universality of the LES method by comparing the simulation results of transport characteristics to experimental three dimensional laser induced fluorescence (3DLIF) studies, (3) addressing design options such as an optimal baffle spacing to minimize undesired flow conditions such as short-circuiting and internal recirculation, and (4) investigating the baffle-spacing-specific simulation parameters for the RANS simulation method which is more widely used for ozone contactor design by the industry, although it cannot explicitly capture the unsteady flow and turbulence.

The reactor geometries investigated in this research are Constant Baffle Spacing Multi-Chamber (CBSMC) ozone contactors and a Variable Baffle Spacing ozone contactor Model (VBSM). CBSMCs are simplified models of four normal-spacing chambers (NS) and eight half-spacing chambers (HS). These models are based on a twelve-chamber various baffle spacing lab-scale model in order to simulate the net flow characteristics without any effects from inlet and outlet conditions, as well as to reduce

the computational cost. The VBSM is developed to investigate the baffle spacing effect on hydrodynamics and solute transport in a reactor and to suggest the optimal design baffle spacing which maximizes the efficiency. The VBSM is also modeled for the purpose of examining the optimal turbulent diffusion coefficient with respect to baffle spacing for the RANS simulation.

The LES of the two multi-chamber ozone contactors (CBSMC-NS and -HS) suggest the occurrence of deficient flow conditions and non-ideal solute transport behaviors. Specifically, the flow through these reactors is characterized by the presence of extensive short-circuiting from one chamber to the next through a relatively narrow baffle gap, large internal recirculation that contributes to back-mixing and a dead zone in the center of each chamber. The LES results also suggest that the flow is highly three dimensional with a pair of symmetric counter-rotating secondary vortices and nodal points in the centre of the recirculation zones. The LES results also show that these hydrodynamic deficiencies could be partially prevented by decreasing the baffle spacing (i.e., from NS model to HS model). Residence time distributions from the LES and comparative RANS studies concluded that the tracer transportation should be based on an instantaneous flow field in which the unsteadiness and turbulence are adequately reflected.

Several LES studies based on VBSM, the baffle spacing of which varies between 0.5 times to 5 times the chamber entrance gate height, suggest the width of a large recirculation grows at about the same rate as the baffle spacing increases. As a result, the width of the short-circuiting path in each chamber increases only a little, leading to severe short-circuiting in the chamber. Instantaneous turbulent eddies are prevalent in the

chamber and increase turbulent mixing. The turbulence statistics are characterized by the flow unsteadiness, and elevated levels of turbulence are found in the short-circuiting flow path. The investigation of the transport of a passive tracer indicates that the tracer is dispersed along the short-circuiting path and spreads into the recirculation zone due to turbulent diffusion. The LES simulation results compare quite well with experimentally obtained results. The base chamber, the baffle spacing of which corresponds to the chamber entrance gate height, clearly exhibits the most favorable behavior having a minimum amount of short circuiting and almost no internal recirculation. Baffle spacing greater than the entrance gate height, but also smaller baffle spacing, worsens the performance in terms of the residence time distribution (RTD). The method of three dimensional LES has proven to be a reliable tool for predicting ozone contactor performance without the need for calibration of model constants.

Finally, the turbulent Schmidt number of RANS simulation was investigated by employing the previously validated LES simulation. Due to strong turbulent mixing, the turbulent Schmidt number was calibrated and found to be much less than the values commonly used in RANS. It was also found that the turbulent Schmidt number is baffle-spacing specific; hence, no universal turbulent Schmidt number exists. Additional studies with different grid resolutions and time step sizes revealed that the turbulent diffusivity in RANS methods also depend strongly on numerical input parameters.

CHAPTER 1

INTRODUCTION

1.1 Motivation

There has been increasing concern about inefficient use of disinfectants for drinking water and wastewater purification processes due to the formation of carcinogenic by-products. These potentially harmful by-products originate from the residual disinfectants in a contact tank (Hart & Gupta 1978; Sepp 1981). Optimal deisgn and control of disinfection process is required to reduce the formation of by-products and maximize disinfection efficiency. However, achieving these two goals are complicated. Various parameters, such as raw water quality, operating temperature, and hydrodynamics in a reactor, affect both processes simultaneously. In particular, reactor hydrodynamics play a significant role in disinfection performance (Roustan et al. 1993; Kim et al. 2004; Tang et al. 2005; Kim et al. 2007a). The ideal flow condition is a plug flow for disinfection reactors without flow recirculation. However, non-ideal flow conditions, i.e., a significant deviation of the hydrodynamics from that of plug flow, exist in most reactors due to the presence of turbulence.

A recent three dimensional laser induced fluorescence (3DLIF) study by Kim et al. (2007a) suggested that flow irregularities such as short-circuiting, internal recirculation within the chamber, and dead zone formation could be prevalent in multi-chamber ozone contactors. In particular, the baffle spacing (i.e. the distance between consecutive baffle walls) was identified as one of the critical design factors that determine the extent of short-circuiting and recirculation. Heathecote et al. (1994) conducted tracer tests for several baffle designs using a down scaled ozone contactor

model and found an efficient baffle arrangement would significant enhance the tracer residence time. The above evidences and other past experimental studies were obtained from a limited set of experiments using lab-scale model reactors, thus the extrapolation of the findings to a wider range of design options and operating conditions is inherently limited.

Computational Fluid Dynamics (CFD) models also have been applied to verify the existence of these flow irregularities with the ultimate goal of developing a versatile tool for reactor flow diagnosis and design (Wang et al. 1998a, 1998b; Gualtieri 2006a, 2006b, 2007). Past CFD simulations on disinfection contactors have been exclusively based on the Reynolds Averaged Navier-Stokes (RANS) equations, in which only the time-averaged velocity field is computed and all the unsteady effects of turbulence are accounted for by turbulence models. RANS modeling is appropriate in flows where the instantaneous flow behaves similarly compared to the time-averaged flow. However, in serpentine contactors, the flow is dominated by the fluctuation and vortex shedding of large-scale turbulent structures, and these flow features pose a significant challenge to RANS approaches.

As an alternative to RANS-based CFD models, the method of Large Eddy Simulation (LES), which lies between two extremes of CFD approaches, i.e. models based on the aforementioned RANS equations and direct numerical simulation (DNS), is employed. DNS calculates all turbulent scales (spatial and temporal) directly; therefore DNS involves extremely high computational costs, which makes this an impractical choice except for simple geometries or fundamental studies of turbulence. In contrast, LES aims at directly simulating large-scale flow structures that are affected by the geometry and boundaries, and models only the small scales (Figure 1.1). Hence, LES offers a substantial increase in accuracy over time-averaged approaches with much less

computational cost than DNS. Furthermore, LES delivers an enormous amount of information on the mean and instantaneous flow field.

1.2 Objectives

The first objective of this research is to provide insight into the hydrodynamics and solute transport phenomena in water and waste water treatment reactors by performing large eddy simulations to capture the unsteady, turbulent flow in ozone contactors. Two Constant Baffle Spacing Multi-Chamber (CBSMC) ozone contactors, which are simplified models of a twelve various baffle spacing multi chamber lab-scale model (Kim 2007), with four normal baffle spacing chambers (NS) and eight half baffle spacing chambers (HS) are generated. The net flow characteristics without any effects from inlet and outlet conditions are simulated by using periodic boundary conditions (Chapter 4). Comparative RANS simulations are conducted to provide quantitative evidence of superiority of LES over RANS models (Chapter 5).

The second objective is to verify the accuracy and the universality of the LES method as a simulation tool in designing a reactor and in diagnosing the disinfection performance. A Variable Baffle Spacing Model (VBSM) is developed for these purposes, and the LES results of this model are compared with the experimental results of transport characteristics from previous three dimensional laser induced fluorescence (3D-LIF) studies (Kim et al. 2010a). The investigation of six different baffle spacing provides quantitative evidence of the optimal design baffle spacing in a tank which maximizes disinfection efficacy with less residual disinfectants. Additionally, turbulence statistics and details of the hydrodynamics for each of the six cases are provided and discussed with regard to the observed tracer break through curves (Chapter 6).

Finally, RANS simulations are carried out to investigate the effect of numerical and physical parameters on the accuracy of RANS (Chapter 7).

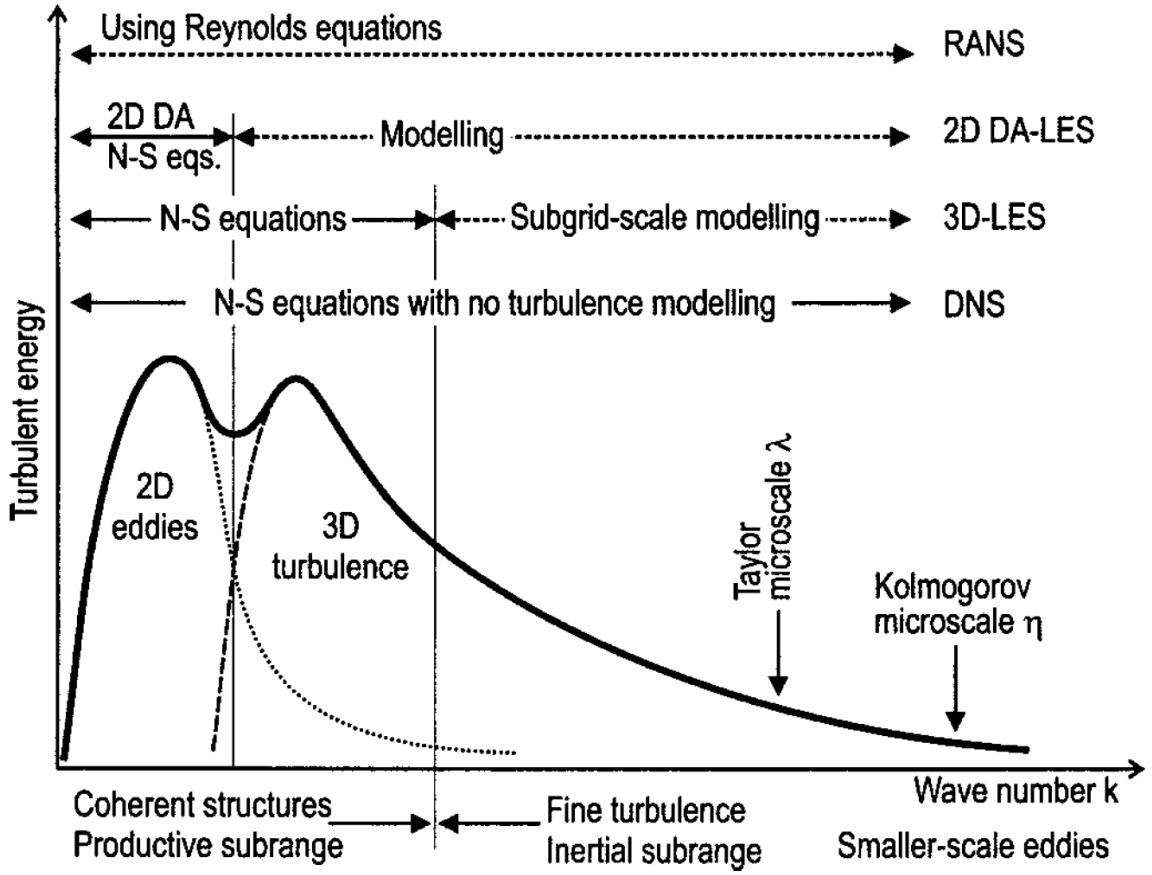

Figure 1.1 Various types of calculation methods and the turbulence spectrum range for proper applications (Nezu and Nakagawa, 1993)

CHAPTER 2

BACKGROUND/LITERATURE REVIEW

2.1 Description of Reactor Hydraulics

The ideal situation in dealing with the hydraulic behavior of any continuous flow reactor is that the velocity profile is known at any point within the reactor. In reality this is not the case, and instead the flow characteristics are indirectly described by the residence time distribution (RTD). Considering the time that each element resides in the reactor, the frequency distribution of these times forms the RTD curve (Figure 2.1). When the system is at steady-state and there is no reaction taking place, the tracer RTD is normalized so that the normalized concentration of the RTD, E, can be represented in such a way that the area under the curve is equal to unity:

$$\int_0^\infty E dt = 1 \qquad \textbf{(2.1)}$$

where t is time, and the mean residence time, θ, of the RTD may be determined as:

$$\theta = \int_0^\infty tE dt \qquad \textbf{(2.2)}$$

It was shown that θ is identical to the ratio of volume divided by the discharge (V / Q) in reactor systems (Levenspiel, 1972). The determination of system RTD provides the information on the spread of actual residence times, and thus the evaluation of a specific reactor.

2.1.1 Determination of the RTD Curve

The method of tracer introduction to the fluid will influence the type of response observed at the outlet of the reactor. Typically, there are two types of tracer input. The first is the injection of tracer in a relatively short period of time to the influent and is called 'pulse input' shown in Figure 2.2(a). The response of this input type is referred to as a C-curve. The second is 'step input'. In this case, the tracer is introduced as a constant input. The response of this input is the time record of the concentration at the outlet reaching a certain adjusted level as shown in Figure 2.2(b). This response referred to as an The F-curve can be transformed to the C-curve by taking its derivative, $dF/dt = C$.

2.1.2 Analysis of the RTD Curves

The RTD curve has been used as a tool for reactor design and as a diagnostic in determining the hydraulic performance in a reactor. The curve shape and the area under the curve may describe much of the hydraulic characteristics of a system and indicate its adequacy for a proper disinfection process. The theoretical residence time of the reactor is defined as the chamber volume, V, divided by the discharge, Q

$$T = V/Q \tag{2.3}$$

The mean residence time, θ, is the centroid of the curve distribution

$$\theta = \int_0^\infty tCdt \Big/ \int_0^\infty Cdt \tag{2.4}$$

and is approximated by discrete time intervals:

$$t_m = \frac{\sum tC\Delta t}{\sum C\Delta t} \tag{2.5}$$

The rest of the parameters for the RTD curve shown in Figure 2.1 are defined as: t_f = time at which the tracer first appears at the outlet; t_p = time at which the peak concentration of the tracer is observed; t_{10} = time at which 10 percent of the tracer has passed through the reactor; and t_{90} = time at which 90 percent of the tracer has passed through the reactor. These parameters can be combined into a series of indices to describe the hydraulic behavior in a reactor (Rebhun and Argaman, 1965): 't_f / T' measures the most severe short-circuiting. In an ideal plug flow reactor, the ratio is one, and with increased mixing it approaches zero. 't_p / T' indicates the average degree of short-circuiting, and also provides an estimate of the effective volume of the reactor. This ratio approaches one in a plug flow and zero with increased mixing. 't_{90} / t_{10}' is the Morrill Dispersion Index, and it is a measure of the spread of the curve. The value will be one in the ideal plug flow case, while it increases for mixing. This index should be less than 2.0 for an effective design. 'θ / T' should equal one (or 't_m / T' should be approximately one) for any reactor to imply the full volume is used. If this value is significantly less than 1.0, the effective volume is much less than the actual volume.

2.2 Numerical simulation techniques of turbulent flow field

Three main approaches to predict turbulent flows are introduced in this section, and Figure 2.3 gives an overview of these methodologies.

2.2.1 Direct Numerical Simulation (DNS)

In principle, incompressible, viscous, and turbulent flow field can be described with the Navier-Stokes equations. The numerical techniques of completely resolving the equations without modeling are called direct numerical simulations (DNS). The DNS captures all significant scales of motion. Therefore, DNS needs very fine mesh size and is still limited to low Reynolds number flows. Rogallo and Moin (1984) estimated that a DNS of the flows requires four grid points in each direction to resolve an eddy, time step to be on the order of $(\delta / u_\tau)\mathrm{Re}_m^{-1/2}$; here Re_m is the Reynolds number based on the channel half-width, δ, and the average flow speed, U_m; and u_τ is the wall shear velocity. With the practical Reynolds number 10^4, 5×10^{10} grid points and 2×10^4 time steps are required to reach a statistically fully developed flow. This computational cost is still too expensive for the capacities of current high performance computers for the industrial applications.

2.2.2 Reynolds Averaged Navier-Stokes Simulation (RANS)

One way to calculate a turbulent flow is time averaging of the Navier-Stokes equations. This kind of simulation is called RANS, and this idea was firstly proposed by Osborne Reynolds (1842-1912). The instantaneous quantity is decomposed into its time-averaged and fluctuating terms. Rearranging the decomposed equation leads to an additional nonlinear term, the so-called Reynolds stresses. Predicting these stresses is called turbulence modeling. This is usually accomplished empirically or by using detailed time-dependent simulation results. The use of RANS implies that flow phenomena are averaged over time, and hence the instantaneous flow dynamics are not captured. Further, most RANS uses the eddy viscosity concept that is not adequate for predicting

anisotropic flows, e.g. flows with high streamline curvature or flows where separation occurs. However, due to the advantage in terms of computational cost, this method has been widely used in many practical high Reynolds number flow simulations.

2.2.3 Large Eddy Simulation (LES)

LES lies between the two extremes of CFD approaches, i.e., the aforementioned DNS and RANS. A spatial filtering procedure is applied based on the fact that the energy contained in the large-scale motions in a flow is much more dominant than that in the small-scale ones (Leonard, 1974). LES was initially proposed by Joseph Smagorinsky (1963) and first applied for the simulation of a small straight channel flow at high Reynolds numbers by Deardorff (1970). LES explicitly simulates large scale eddies, which are responsible for the majority of momentum transport and turbulent diffusion (Ferziger and Peric, 1996), and treats the smaller scale eddies with approximate models, called Sub Grid Scale Model (SGS Model). The results of LES are relatively insensitive to the contribution of the small-scale eddies. Also, the statistics of small-scale turbulence is more universal than those of the large scale motions (Ferziger, 1993). Hence, LES promises a wider generality and greater accuracy compared to a solution of the RANS. In the past, LES was limited to small scale simulations and performed on supercomputers only. With increasing computer speed and the provision of parallel processing techniques (Table 2.1), it has become possible to apply LES to more complex geometries even in the industrial area.

2.3 Experimental studies on the disinfection reactors

The tracer RTD curves provide the reactor disinfection efficiency and allow designers or users to assess its feasibility to their usage purposes. Heathecote et al. (1994) conducted tracer studies for several baffle designs based on a down scaled ozone contactor model and found that an efficient baffle arrangement would have a significant enhancement in tracer residence time. However, to better understand and improve the reactor's performance, the RTD curves are too limited. Hence, there have been many efforts to visualize the reactor hydrodynamics. A Laser Doppler Anemometer studies conducted by Shiono and Teixeira (2000) suggest that a multi-chamber reactor used for chlorine disinfection with horizontally meandering flow could be susceptible to the formation of recirculation within the chamber. Kim et al. (2008) employed a three dimensional laser induced fluorescence (3DLIF) method and suggested that flow irregularities such as short-circuiting and internal recirculation within the chamber could be prevalent in multi-chamber ozone contactors. In particular, the baffle spacing (i.e. the distance between consecutive baffle walls) was identified as one of the critical design factors that determine the extent of short-circuiting and recirculation. This evidence was obtained from a limited set of experiments performed using lab-scale model reactors, thus the extrapolation of the findings to a wider range of design options and operating conditions is inherently limited.

2.4 Numerical studies on the disinfection reactors

In addition to only a few experimental studies, computational fluid dynamics (CFD) models have been applied to verify the existence of internal recirculation in multi chamber reactors. Henry and Freeman (1995) applied a two dimensional finite element model which is based on the Reynolds-Averaged Navier Stokes equations (RANS) with

standard k-ε turbulence model to study flow in an ozone contactor. They found that an additional guide vane would improve the disinfection performance more than corner and edge curvature modifications. Two dimensional CFD simulations with a number of different turbulence models (e.g., depth-averaged viscosity model, k-ε model, and Smagorinsky model) and different convection schemes (e.g., first- or third-order upwind schemes and QUICK scheme) have been attempted for flow simulation of multi-chamber chlorine contactors (Wang et al. 1998a, 1998b; Gualtieri 2006a, 2006b, 2007). A three dimensional CFD simulation was conducted by Murrer et al. (1995) investigating mixing behavior in an existing ozone contact tank by modifying the position of gas injection. Zhang et al. (2007) developed a three dimensional CFD model using a commercial CFD code (CFX 10) with standard k-ε model to address the major components of ozone disinfection processes in an existing water treatment plant. They could improve contactor performance by installing four additional baffles in the last chamber with reduced dead zone and short-circuiting. Wols et al. (2008) investigated the hydraulics and RTD characteristics in a full-scale ozone contactor numerically and experimentally. They used a finite-element flow simulation code (Finlab) with standard k-ε model. The turbulent Schmidt number they employed was 1.0. They also studied a particle tracking method using time-averaged velocity vectors and a random displacement. The random displacement consists of the diffusion coefficient which was also employed for tracer diffusion. Their results suggest that the simulation results compared at earlier chambers (up to the third one) were not able to detect the highly fluctuating measured data. In addition, the 2D code was less accurate than the 3D simulation due to the lack of detecting three dimensionality induced by the side walls. They could improve the contactor performance by adding a horizontal baffle to interrupt the main flow.

The CFD simulations of flow and solute transport in ozone contactors mentioned so far have been exclusively based on solving the RANS equations, in which only the

time-averaged velocity field is computed and all the unsteady effects of turbulence are accounted for by turbulence models. The flow in an ozone contact chamber is characterized by unsteady large-scale flow structures due to flow separation and vortex formation. The accurate prediction of their effects on the time-averaged flow is a significant challenge for RANS turbulence closure models. Moreover, the calculation of the unsteady transport of a tracer using a RANS-based model can only be accurate if the instantaneous flow is similar to the time-averaged flow or if the effect of turbulence is accounted for through an adequate (calibrated) turbulent diffusivity.

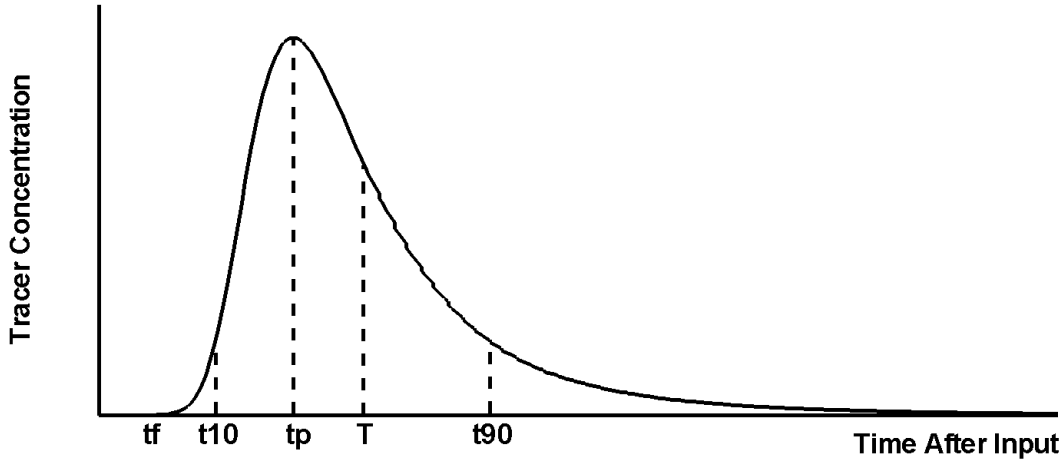

Figure 2.1 Schematic of tracer RTD curve

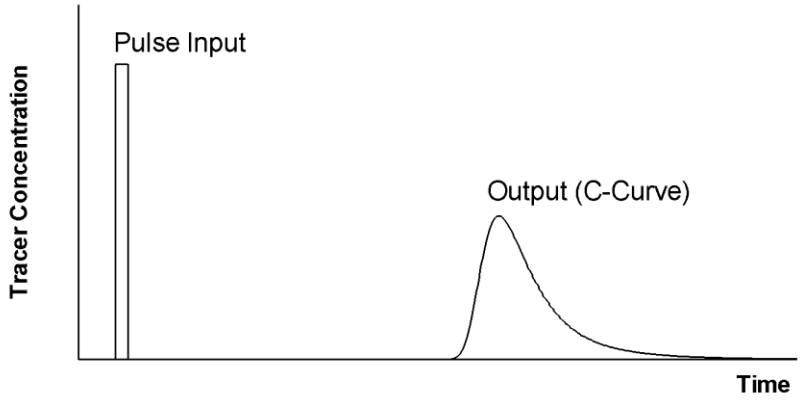

(a)

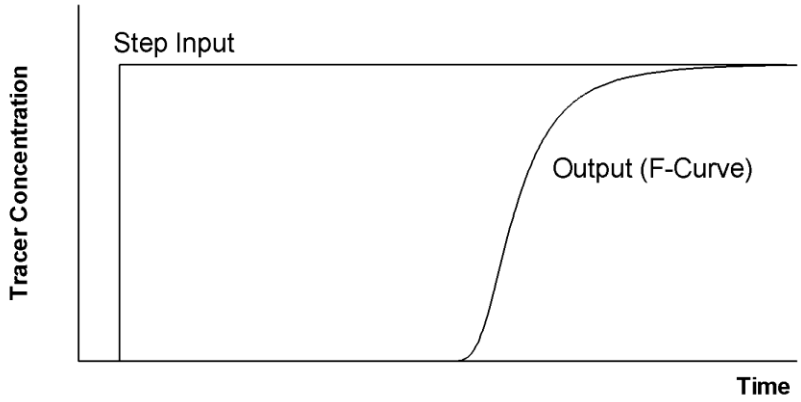

(b)

Figure 2.2 Examples of pulse and step input and resulting outputs

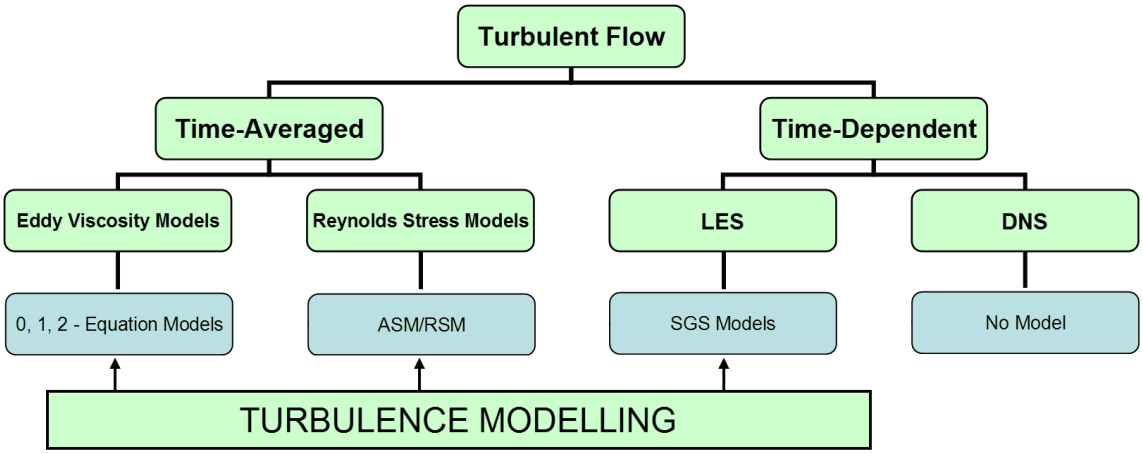

Figure 2.3 Treatment of turbulent flows (Sturm, 2010)

Table 2.1 List of available CFD codes for turbulent flows

CODE	Provider	Turbulence Models	Parallel Computing
STAR-CD	CD-adapco	RANS	Included
CFX-5	AEA Technology Engineering Software Ltd	RANS • Standard k-ε, k-ω, RNG k-ε • Second Moment Closer (SMC) • Shear Stress Transport Model (SST)	Included
FLUENT	ANSYS	RANS • Standart k-ε, k-ω, Spalart-Allmaras • RSM LES • Smagorinsky-Lilly model • Dynamic Smagorinsky-Lilly model • WALE model • Dynamic kinetic energy model	Included
CFD-ACEU	ESI Group	RANS • Standard k-ε, k-ω, RNG k-ε • Kato-Launder k-ε • Low Reynolds Number k-ε • Two-layer k-ε • Spalart-Allmaras LES • Smagorinsky Model • Germano's Dynamic Model • Menon's Localized Dynamic	Included

CHAPTER 3

NUMERICAL SETUP AND FRAMEWORKS

3.1 Computational models

The investigated reactor models are two uniform baffle spacing models and a variable baffle spacing model.

3.1.1 Constant Baffle Spacing Multi Chamber (CBSMC) ozone contactor model

The CBSMC contactors are simplified models of a various baffle spacing multi chamber lab-scale model. Figure 3.1 shows the lab-scale replica of the ozone contactor model constructed by Kim et al. (2010a). This model consists of twelve different width chambers, and its overall volume is approximately 0.0755 m^3. In order to reduce the computational cost, the twelve chamber model was simplified to a four chamber reactor maintaining the same chamber dimensions. This simplified model is referred to as Normal Spacing (NS) model. Another reactor with half the channel width referred to as Half Spacing (HS) model was also examined (Figure 3.2).

3.1.2 Variable baffle spacing ozone contactor model (VBSM)

The VBSM is developed to investigate the baffle spacing effect on hydrodynamics and solute transport in a reactor and to suggest the optimal baffle spacing which maximizes the efficiency. Figure 3.3a shows the schematic of the lab-scale contactor constructed by Kim et al. (2010). The contactor consists of two upstream chambers for flow development, a main chamber the baffle spacing of which is variable by re-locating a removable baffle, and downstream chambers. In this study, the main baffle spacing varies between 15mm and 150mm (Figure 3.3b).

3.2 Governing equations

In this chapter, the equations and numerical treatments of the fluid flow are introduced.

3.2.1 Navier-Stokes equation

The flow field is described by the Navier-Stokes equations for mass and momentum conservation which were derived from Newton's laws of motion.

The continuity equation is based on the idea that the change of mass in a control volume is equal to the difference of the total mass which enters and leaves through the faces of the volume, and can be written in multi-dimensional tensor form as

$$\frac{\partial u_i}{\partial x_i} = 0, \tag{3.1}$$

where x_i is the co-ordinates and u_i is the velocity components in each direction with index i is 1,2, or 3.

The momentum equation is based on the idea that the rate of change of momentum of a control volume is equal to the resultant force acting on the volume in each direction of the force, and can be written as

$$\frac{\partial u_i}{\partial t} + \frac{\partial (u_i u_j)}{\partial x_j} = -\frac{1}{\rho}\frac{\partial p}{\partial x_i} + \nu \frac{\partial^2 u_i}{\partial x_j^2}, \tag{3.2}$$

where t is the time, ρ is the water density, p is the pressure, and ν is the dynamic viscosity.

3.2.2 Advection-diffusion equation

Transport of a conservative tracer was described by solving the following advection-diffusion equation for the concentration, C:

$$\frac{\partial C}{\partial t} + u_i \frac{\partial C}{\partial x_i} = (D + D_t) \frac{\partial^2 C}{\partial x_i^2}, \tag{3.3}$$

where D is the molecular diffusivity and D_t is the turbulent eddy diffusivity. D is the ratio of molecular viscosity to the molecular Schmidt number (Sc), D_t is calculated as the ratio of the turbulent subgrid-scale viscosity $\nu_{t,sgs}$ to the turbulent Schmidt number (Sc_t).

3.3 Treatment of turbulent flows

3.3.1 LES Subgrid Scale (SGS) Models

The flow variables are decomposed into a large scale or resolved component (denoted by an overbar), and a subgrid-scale component. The resolved component is defined by the filtering operation:

$$\bar{f}(x) = \int \overline{G}(x, x') f(x') dx' \tag{3.4}$$

where $\overline{G}$ is the grid filter function satisfying the relation, $\int \overline{G}(x, x') dx' = 1$. The most commonly used filter function is the box filter in real space:

$$G(x, x') = \begin{cases} 1/\Delta : if \left| x - x' \right| < \Delta / 2 \\ 0 : \text{otherwise} \end{cases} \tag{3.5}$$

where $\overline{\Delta}$ is the filter width or a typical grid spacing.

The filtered continuity and Navier-Stokes equation can be written in tensor form as (Germano et al., 1991):

$$\frac{\partial \overline{u}_i}{\partial x_i} = 0, \tag{3.6}$$

$$\frac{\partial \overline{u}_i}{\partial t} + \frac{\partial}{\partial x_j}\left(\overline{u}_i \overline{u}_j\right) = -\frac{\partial \overline{p}}{\partial x_i} - \frac{\partial \tau_{ij}}{\partial x_j} + \frac{1}{\mathrm{Re}} \frac{\partial^2 \overline{u}_i}{\partial x_j \partial x_j} \tag{3.7}$$

where i and j = 1, 2, and 3 correspond to x, y, and z coordinates, respectively; and Re is the Reynolds number. $\overline{u}_i$ is the instantaneous filtered velocity component in the i direction, $\overline{p}$ represents the filtered pressure, and t is the non-dimensional time. The equations have been non-dimensionalized by appropriate velocity and length scales.

Smagorinsky SGS model

The anisotropic part of the subgrid-scale (SGS) Reynolds stresses, $\tau_{ij} = \overline{u_i u_j} - \overline{u}_i \overline{u}_j$, are formulated using the Smagorinsky eddy-viscosity model (Smagorinksy, 1963) to yield

$$\tau_{ij}^a = \tau_{ij} - \frac{1}{3}\delta_{ij}\tau_{kk} = -2\nu_t \overline{S}_{ij} = -2C\overline{\Delta}^2 \left|\overline{S}\right| \overline{S}_{ij} \tag{3.8}$$

where δ_{ij} is the Kronecker delta and ν_t is the eddy viscosity. $\overline{S}_{ij} = \frac{1}{2}\left(\partial \overline{u}_i / \partial x_j + \partial \overline{u}_j / \partial x_i\right)$ represents the filtered strain-rate tensor, $\left|\overline{S}\right| = \left(2\overline{S}_{ij}\overline{S}_{ij}\right)^{1/2}$ is the magnitude of the resolved-scale strain-rate tensor. The subgrid-scale kinetic energy, τ_{kk}, is added to the pressure term. The eddy viscosity is a function of the strain-rate tensor and the subgrid length l as $\nu_t = l^2 \left|\overline{S}_{ij}\right|$, and the l is assumed to be proportional to the filter width as $l = C_s \overline{\Delta}$. Here C_s is called the Smagorinsky constant and usually set to be 0.1 (Smagorinsky, 1963; Lilly, 1966; Deardorff, 1970; Mason and Callen, 1986; Piomelli et al., 1988).

Dynamic SGS model

There are some drawbacks of the Smagorinsky model such as the dependency of the model constant on the flow condition, the necessity of additional assumptions for taking into account the flows undergoing transition or near wall, and the lack of describing the transfer of energy from unresolved to resolved scales (called backscatter). Instead of using a single positive value for the model constant C_s, Germano et al. (1991) proposed a dynamic procedure which implicitly computes C in Eq. (3.8) and also captures backscatter (i.e., energy transfer from small scales to large scales). A second filter, referred to as a test filter and denoted by $\overline{\overline{G}}$, is applied to the filtered equations, Eqs. (3.6) and (3.7), with the characteristic length scale of $\overline{\overline{G}}$, denoted by $\overline{\overline{\Delta}}\left(>\overline{\Delta}\right)$. Germano et al. (1991) suggested the best scaling factor, $\overline{\overline{\Delta}}/\overline{\Delta}$, to be 2 which is employed in the present study. The resolved turbulent stress, $L_{ij} \equiv \overline{\overline{\overline{u}_i \overline{u}_j}} - \overline{\overline{\overline{u}}}_i \overline{\overline{\overline{u}}}_j$, representing the energy scales between the test and the grid filters is then related as:

$$T_{ij} = \overline{\overline{\overline{u_i u_j}}} - \overline{\overline{\overline{u}}}_i \overline{\overline{\overline{u}}}_j \tag{3.9}$$

$$\overline{\overline{\tau}}_{ij} = \overline{\overline{\overline{u_i u_j}}} - \overline{\overline{\overline{u}_i \overline{u}_j}} \tag{3.10}$$

and

$$L_{ij} \equiv T_{ij} - \overline{\overline{\tau}}_{ij} \tag{3.11}$$

Substituting the anisotropic sub-scale stresses, τ_{ij}^a and T_{ij}^a, in the same functional form of Eq. (3.8) into Eq. (3.11) results in

$$L_{ij} - \frac{1}{3}\delta_{ij} L_{kk} = \alpha_{ij} C - \overline{\overline{\beta_{ij} C}} \tag{3.12}$$

where $\alpha_{ij} = -2\overline{\overline{\Delta}}^2 \left|\overline{\overline{S}}\right| \overline{\overline{S}}_{ij}$ and $\beta_{ij} = -2\overline{\Delta}^2 \left|\overline{S}\right| \overline{S}_{ij}$. Eq. (3.12) represents five independent equations for symmetric and traceless tensors involving only one unknown C. Lilly (1992) proposed to choose C so as to minimize its error by a least squares approach. If

define $Q = \left(L_{ij} - \frac{1}{3}\delta_{ij} L_{kk} - \alpha_{ij} C + \overline{\overline{\beta_{ij} C}} \right)^2$ as the square of the error of Eq. (3.12), *i.e.*, , C is evaluated as:

$$C = \frac{M_{ij} L_{ij}}{M_{kl} M_{kl}} \tag{3.13}$$

where $M_{ij} = \alpha_{ij} - \overline{\overline{\beta}}_{ij}$.

3.3.2 Standard k-ε closure model for RANS

Instead of decomposing the flow variables into a large and a subgrid-scale components, the instantaneous quantity is decomposed into its time-averaged and fluctuating components. As the spatial filtering step in the LES, after rearranging the decomposed equation, an additional nonlinear term, called Reynolds stresses, is yielded. Like most of the turbulent models, the standard k-ε model for RANS employs the eddy-viscosity concept of Boussinesq (1877):

$$-\overline{u_i u_j} = \nu_t \left(\frac{\partial \overline{u_i}}{\partial x_j} + \frac{\overline{\partial u_j}}{\partial x_i} \right) - \frac{2}{3} k \delta_{ij} \tag{3.14}$$

where $k = \frac{1}{2}\left(\overline{u_i' u_i'}\right)$ is the turbulent kinetic energy. Here the eddy viscosity ν_t is defined as a scalar quantity (not a fluid property but depends strongly on the nature of turbulence, Nezu et al., 1993), and thus ν_t is the same for all stress components meaning which is isotropic. ν_t is considered to be proportional to a velocity and a typical length scale of fluctuating motion.

Prandtl (1920) employed mixing length theory for the turbulent characteristic length $L = \sqrt{\nu_t / (\partial y / \partial \bar{u})}$. This is called 'zero equation model' because it does not use a transport equation of turbulent quantity. When the definition of turbulent kinetic energy ($k = \frac{1}{2}\left(\overline{u_i' u_i'}\right)$) is used, and $\sqrt{k}$ is defined as velocity scale, the length scale is obtained as $L = \nu_t / (C_\mu \sqrt{k})$. This is rearranged using turbulent dissipation rate ε, usually modeled as $L \sim k^{3/2} / \varepsilon$, for the eddy viscosity as $\nu_t = C_\mu k^2 / \varepsilon$ (Launder 1972 and Spalding 1974). The distribution of the kinetic energy is:

$$\bar{u}_i \frac{\partial k}{\partial x_i} + \frac{\partial k}{\partial t} = \frac{\partial}{\partial x_i}\left(\frac{\nu_t}{\sigma_k}\frac{\partial k}{\partial x_i}\right) + \nu_t\left(\frac{\partial \bar{u}_i}{\partial x_j} + \frac{\partial \bar{u}_j}{\partial x_i}\right)\frac{\partial \bar{u}_i}{\partial x_j} - \varepsilon \qquad \textbf{(3.15)}$$

and the distribution of the dissipation rate is:

$$\bar{u}_i \frac{\partial \varepsilon}{\partial x_i} + \frac{\partial \varepsilon}{\partial t} = \frac{\partial}{\partial x_i}\left(\frac{\nu_t}{\sigma_\varepsilon}\frac{\partial \varepsilon}{\partial x_i}\right) + C_{1\varepsilon}\frac{\varepsilon}{k}\nu_t\left(\frac{\partial \bar{u}_i}{\partial x_j} + \frac{\partial \bar{u}_j}{\partial x_i}\right)\frac{\partial \bar{u}_i}{\partial x_j} - C_{2\varepsilon}\frac{\varepsilon^2}{k} \qquad \textbf{(3.16)}$$

The equations contain five empirical constants, and the standard k-ε model employs values for the constants that are arrived at by comprehensive data suitable for a wide range of the turbulent flows.

Table 3.1 Constants for the standard k-ε model (Versteeg and Malalasekera, 1995)

C_μ	σ_k	σ_ε	$C_{1\varepsilon}$	$C_{2\varepsilon}$
0.09	1.0	1.3	1.44	1.92

3.4 Discretization schemes

The mathematical formulas of the fluid flow are partial differential equations, and they express the variation of the dependent variables throughout the domain.

3.4.1 Space discretization

The continuum should be discretized spatially with mesh fine enough to satisfy numerical stability and maintain conservation of mass. There are three most commonly applied types of grids: structured, unstructured, and block structured grids as shown in Figure 3.4. Structured grid is the simplest case of grid generation; however this simplicity is also a disadvantage when it is applied to complex geometries. For complex geometry with high curvature or sharp corners, unstructured grid might be the best choice. On the other hand, unstructured grid needs much more computer memory as neighboring point information has to be stored explicitly (Oertel et al., 1995). For the present study, the last gird type of block structured is much more proper. Although the geometry seems a simple rectangular box, the volume is divided into smaller size blocks with structured grids to represent several numbers of emptied volumes of baffles. The domain needs to be divided also in order to run the simulation on multiple processors using parallel processing module. Figure 3.5 and 3.6 show the resulting grids for both application contactor models.

3.4.2 Equation discretization

Once the mesh has been defined the equations consisting of the partial derivatives are discretized to be solved for the flow variables at discrete grid points. Three methods

for discretization of the governing equation exist: Finite Difference Method (FDM), Finite Element Method (FEM), and Finite Volume Method (FVM) as shown in Figure 3.7. Because FEM is based on unstructured grids, this method is highly flexible, but more expensive to solve the problem. FDM and FVM are both based on structured grids, and FVM is more flexible than FDM. FDM is a relatively simple method, but requires uniform meshes with high degree of regularity of mesh to satisfy conservation of mass. Hence, current study applied FVM. In FVM, the integral formulas of Navier Stokes equation are directly discretized in physical space. This is obtained by integrating the differential form over a control volume and applying the Gauss theorem to transform volume integrals into surface integrals. The surface integrals are approximated by the midpoint rule as:

$$F_{i+1/2} = \int_{A_{i+1/2}} f \cdot dA \approx f_{i+1/2} \cdot A_{i+1/2} \qquad \textbf{(3.17)}$$

where F is fluxes, A is the cell face area, and f is the integrand. This approximation has second-order accuracy in space if the value f is known at the cell faces. For the non-staggered or collocated grid arrangement, f can be obtained by interpolation. There have been five different approximations for the value $f_{i+1/2}$.

HYBRID scheme

The HYBRID scheme (Spalding 1972) is, as the name indicates, a combined method of two schemes: the upwind differencing schem (UDS) and the second order central differencing scheme (CDS-2) depending on the local Peclet number ($\mathrm{Pe} = u\Delta x / \nu$). If the Peclet number is greater than 2.0, it switched from CDS-2 to UDS so that the scheme is unconditionally stable. However, due to the usage of UDS, this method is known to be numerically diffusive and therefore not well suited for LES.

$$\begin{cases} \frac{1}{2}(f_i + f_{i+1}) : \mathrm{Pe}_{i+1/2} \le 2.0 \\ f_i : \text{otherwise} \end{cases} \quad \textbf{(3.18)}$$

CDS-2 scheme

The CDS-2 scheme interpolates the value f at the cell face linearly, and this scheme has been usually used for LES.

$$\frac{1}{2}(f_i + f_{i+1}) \quad \textbf{(3.19)}$$

HLPA scheme

The Hybrid Linear/Parabolic Approximation (HLPA) is the method which combines a second order upstream-weighted approximation and first-order upwind differencing scheme under the criterion. Zhu (1991) who proposed this scheme claims that HLPA is low diffusive and unconditionally stable.

$$f_i + \gamma(f_{i+1} - f_i)(\frac{f_i - f_{i-1}}{f_{i+1} - f_{i-1}}) \quad \textbf{(3.20)}$$

where

$$\gamma = \begin{cases} 1 : 0 < \dfrac{f_i - f_{i-1}}{f_{i+1} - f_{i-1}} < 1 \\ 0 : \text{otherwise} \end{cases}$$

QUICK scheme

The Quadratic upwind differencing scheme for convective kinetics (QUICK) scheme suggested by Leonard (1979) uses a three-point upstream-weighted quadratic interpolation for the value $f_{i+1/2}$. Although quadratic interpolation has a third-order truncation error, this method has second-order accuracy if it is used with the midpoint rule of the surface integral.

$$\frac{3}{8} f_{i+1} + \frac{3}{4} f_i - \frac{1}{8} f_{i-1} \tag{3.21}$$

CDS-4

The CDS-4 (Breuer 1994) uses four nodes with a third-order polynomial: two nodes from the upstream side and two nodes from the downstream side. As CDS-2 does, CDS-4 is independent of the flow direction, since this is a symmetric interpolation. However, this scheme also has second-order accuracy if it is combined with the midpoint rule.

$$-\frac{1}{16} f_{i+2} + \frac{9}{16} f_{i+1} + \frac{9}{16} f_i - \frac{1}{16} f_{i-1} \tag{3.22}$$

3.4.3 Time discretization

For time-dependent problems an intermediate step between space and equation discretization must be introduced. Through integration in time, the equations will lead to an algebraic system for unknowns. There are many criteria for choosing a scheme for integrating systems of differential equations, but the storage requirements are critical when very large systems are considered. If the predictor-corrector scheme is used, it may need the storage of a sizable history of the system. However, Runge-Kutta schemes, if appropriately designed, higher order schemes may require no more storage than 2N locations, one for each of the N coordinates and N velocities:

$$q_i = a_i q_{i-1} + hf(x_{i-1}) \tag{3.23}$$

$$x_i = x_{i-1} + b_i q_i \tag{3.24}$$

with $a_1 = 0$. Values of q_i and x_i overwrite the previous ones so that only 2N storage locations q and x are required at each stage. This explicit low-storage multistage scheme

was suggested by Willimson (1979), and the present study applies three steps with second-order accuracy.

3.5 Implementation of Boundary Conditions

Control volumes, which coincide with the domain boundaries, require specifications of a certain boundary condition. The boundary condition must be a known value (i.e., Dirichlet condition), a combination with data of an interior cell (i.e., Neuman condition), or mixed type of these two.

3.5.1 Dirichlet boundary

The first boundary condition type, named after Johann Peter Gustav Lejeune Dirichlet (1805-1859), specifies the values with a solution on the boundary of the domain. This type is mainly used for the heat conduction problem with constant boundary temperature, the inflow boundary condition with the mean velocity over the entire inlet area of the flow field, and wall boundaries with no-slip conditions (i.e., zero velocity in all directions at the boundary surfaces).

3.5.2 Neumann boundary

The Neumann boundary condition is named after Carl Neumann (1832-1925). This type involves a derivative of a solution to be taken on the boundary of the domain. This type is often used for the heat conduction problem when heat flux at boundary surface is given or outflow conditions with zero gradient (i.e., $u_{ni} = u_{ni-1}$).

3.5.3 Free surface boundary

If wind induced shear stresses on the surface are neglected, free surface or symmetry boundary is a suitable setting for water surface. The conditions at a symmetry boundary are: (a) no convective flux across the boundary and (b) no normal gradient at the boundary. Normal velocities are set to zero at a symmetry boundary and the values just outside the domain are set be equal to the values just inside the domain.

3.5.4 Periodic boundary

When flow and boundary conditions repeat such as swirling flow in a cylindrical furnace or the domain of interest is only a small part of a large system far from its edge, periodic or cyclic boundary conditions can be used by considering a sector of a full domain. The flux at the outlet boundary is set to be equal to the flux entering the inlet boundary.

3.5.5 Wall function boundary

Under the high Reynolds number flow condition, integrating the grid over the whole viscous sub-layer (Figure 3.8) is undesirable since the velocity profile inside the layer is steep, and many grid points should be placed in this layer which makes the computation very expensive. However, according to Launder and Spalding (1974) the wall law, which is sufficiently universal, can be taken to connect wall shear stress to the dependent variable outside the viscous sub-layer. In this study, a wall function given by Schlichting (1979) is used for RANS:

$$\frac{\bar{u}}{u_*} = \frac{1}{\kappa}\ln\left(\frac{30y}{k_s}\right) \qquad \textbf{(3.25)}$$

where u_* is the resultant shear velocity, κ is the von Karman constant (~ 0.4), and k_s is roughness length-scale.

3.6 Solution of the algebraic equation

There are two typical methods for solving linear equations $A\phi = b$. One is 'direct method', which solves the equations at once using inverse matrix such as $\phi = A^{-1}b$. However, this method is unfavorable in both data storage and computation time aspects. Another way is 'iterative method' which assumes the solution ϕ^0 and solves the equation to find better solution ϕ^1. This step is repeated until $\phi^n - \phi^{n-1}$ becomes negligible, where the superscript n indicates iteration number. The convergence varies from methods to methods of solving a matrix.

The simplest iterative method is Gauss-Seidel method suggested by Nekrasov (1885). This method calculates the unknown value ϕ^P at each grid node P from the guessed or assumed value ϕ^* at the neighboring grid nodes. Using this method, two dimensional discritized-equation

$$a_P\phi_P = a_E\phi_E + a_W\phi_W + a_N\phi_N + a_S\phi_S + b_P \quad \textbf{(3.26)}$$

can be restated as

$$a_P\phi_P = a_E\phi_E^* + a_W\phi_W^* + a_N\phi_N^* + a_S\phi_S^* + b_P \quad \textbf{(3.27)}$$

and Figure 3.9 (a). If only ϕ_N^* and ϕ_S^* are used as guessed value as shown in the Figure 3.9 (b), the equation becomes the tri-diagonal matrix (TDMA) as

$$a_P\phi_P = a_E\phi_E + a_W\phi_W + a_N\phi_N^* + a_S\phi_S^* + b_P \quad \textbf{(3.28)}$$

and only ϕ_P, ϕ_E, and ϕ_W are treated as unknown values. Peaseman and Rachford (1955) proposed a method which uses sweeping (applying a method for a grid-line and moving for the next grid-line) with the TDMA, and this version is call the alternating direction iteration (ADI) or Line-By-Line method. TDMA and ADI method are more implicit that Gauss-Seidel method, and thus show higher convergence rate. In other words, each step is more close to 'direct method'. Stone (1968) proposed even more strong implicit procedure (SIP) than ADI deriving from the *LU* decomposition a kind of direct method, which results in significantly greater convergence. As the Figure 3.9 (c) indicates, this equation has the form as

$$a_P\phi_P = a_E\phi_E + a_W\phi_W + a_N\phi_N + a_S\phi_S + \beta_{NW}\phi_{NW}^* + \beta_{SE}\phi_{SE}^* + b_P \quad \textbf{(3.29)}$$

and uses guessed values ϕ^*_{NW} and ϕ^*_{SE} which locate at farther nodes. Generally, these two values are approximated with respect to ϕ_P, ϕ_E, ϕ_W, ϕ_N, and ϕ_S, and also a relaxation factor (this factor is also called as partial cancellation factor since the exact guessed values are partially cancelled out by the approximated values in the equation). In this study, the relaxation factor is set to by 0.92.

3.7 Accuracy of LES simulation assessment

3.7.1 Near wall grid spacing

The quality of the near wall grid resolution is assessed based on the distribution of the dimensionless grid spacing, y^+, defined as follows (Versteeg and Malasekera, 2007):

$$y^+ = \frac{d}{\nu}\sqrt{\frac{\tau_w}{\rho}} \tag{3.30}$$

$$\tau_w = \mu\frac{u_p}{\Delta y_p} \tag{3.31}$$

The no-slip wall boundary condition is mathematically correct only if the first grid point off the wall is placed within the viscous sub-layer (i.e., $y^+ \leq 11$), in which the effects of turbulence are negligible compared to viscous effects.

3.7.2 Power density spectra (PDS)

The energy prevailing in large eddies with lower frequency is successfully cascaded to smaller eddies with higher frequency. When the PDS is plotted versus frequency both in logarithmic scales, the simulated decay should follow the Kolmogorov -5/3 slope to confirm that the energy transfer from large scales to small scales is physically realistic (Pope, 2005). For the PDS computation, the Matlab R2010b program is employed in this study which supports Welch's method (Welch, 1967). The Welch's method applies the fast Fourier transform (FFT) algorithm to estimate power spectra. The

principal advantage of this method is a reduction in the number of computations by sectioning the record and averaging modified periodograms of the sections. The method splits the data into overlapping segments, calculates modified periodograms of the overlapping segments, and averages the periodograms to produce the power spectral density estimate. The Matlab command, [Pxx,f] = pwelch(x, window, noverlap, nfft, fs), indicates that Pxx = the power spectral density; x = the input signal vector; window = the length of the Hamming window; noverlap = the number of signal samples (elements of x); nfft = the length of FFT; and fs = the sampling frequency in hertz (Hz), respectively (Matlab, 2011).

3.8 Closure

Table 3.2 Selected features of the CFD code in this work

APPLICATION NUMERICAL MODEL
• Constant baffle spacing multi chamber ozone contactor model • Variable baffle spacing ozone contactor model
DISCRETIZATION IN SPACE
• Finite Volumes on block-structured grids • Collocated and Cartesian variable arrangement • Cartesian coordinate system
EQUATION DISCRETIZATION
• CONVECTIVE TERMS: CDS • DIFFUSIVE TERMS: CDS • PRESSURE COUPLING: SIMPLEC Algorithm • TIME: Low-storage explicit three step Runge-Kutta Method
TURBULENCE CLOSURE
• LES: Smagorinsky and Dynamic SGS closure • RANS: k-ε model
BOUNDARY CONDITIONS
• Diriclet: Inflow, No-slip wall (LES) • Neumann: Outflow • Free Surface Boundary: Water surface • Wall Boundary: No-slip wall (RANS) • Periodic Boundary: Inflow and outflow (CBSMC)
LINEAR SOLVER
• SIP

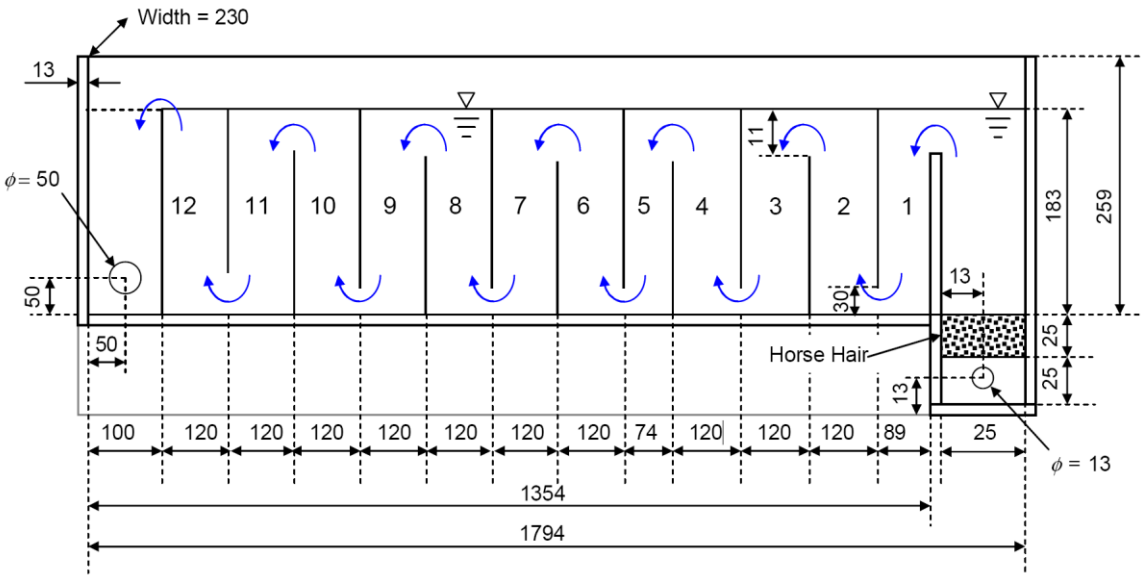

Figure 3.1 Schematic diagram of the twelve-chamber ozone contactor lab-scale model (Kim et al., 2010) (units in mm)

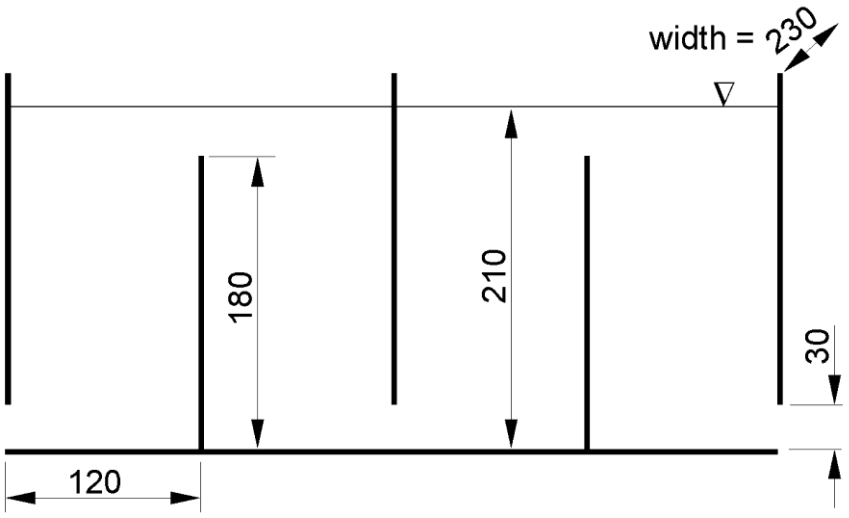

(a)

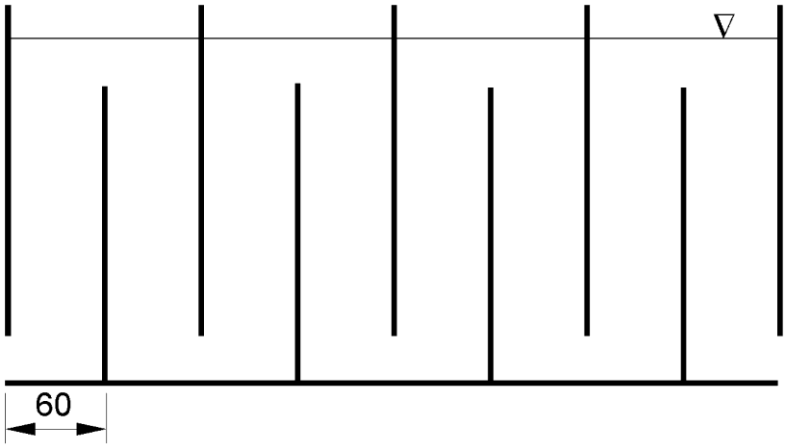

(b)

Figure 3.2 Constant Baffle Spacing Multi Chamber (CBSMC) ozone contactor computational models: (a) four chamber Normal Spacing (NS) model and (b) eight chamber Half Spacing (HS) model (units in mm)

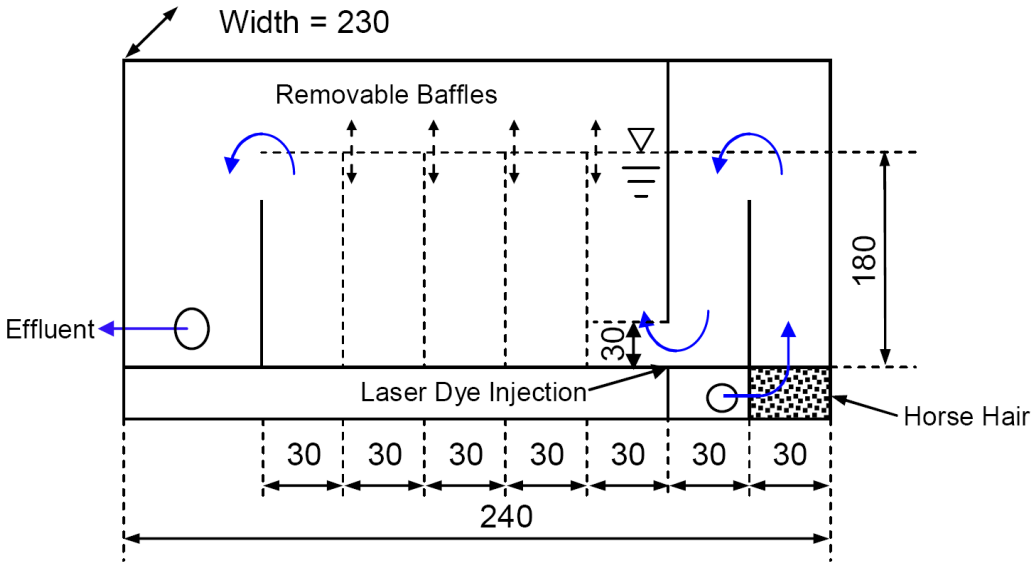

(a)

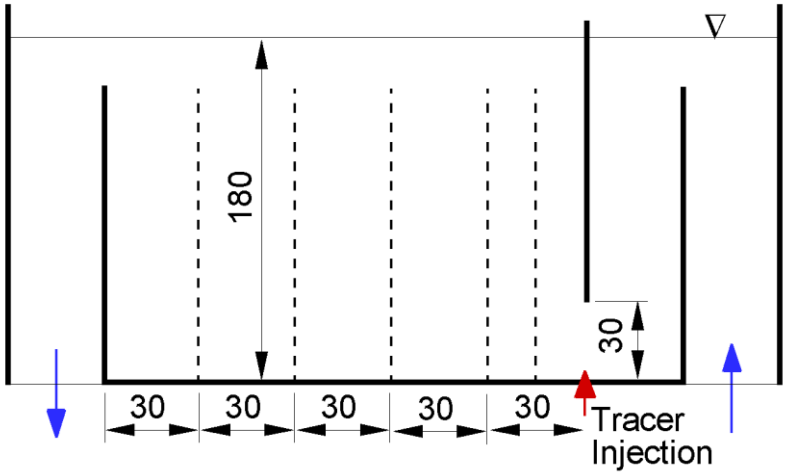

(b)

Figure 3.3 Schematic diagram of (a) the lab-scale variable baffle spacing ozone contactor model (VBSM) with a removable baffle (Kim et al, 2010) and (b) the computation model (units in mm)

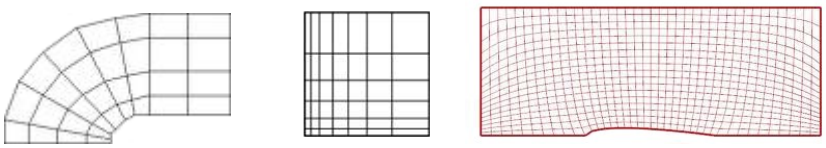

(a)

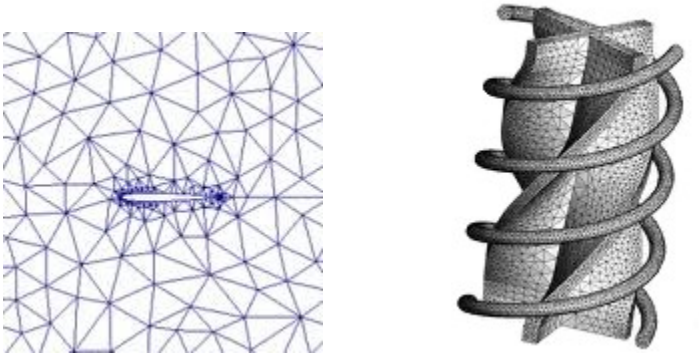

(b)

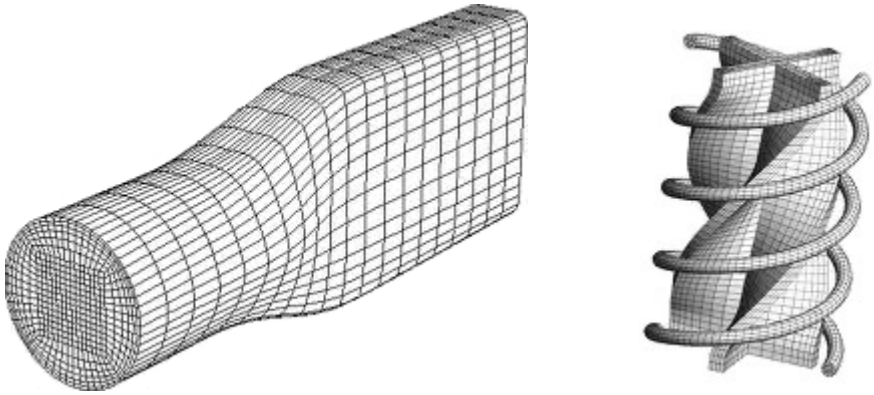

(c)

Figure 3.4 Examples of grid type: (a) structured grid, (b) unstructured grid, and (c) block-structured grid

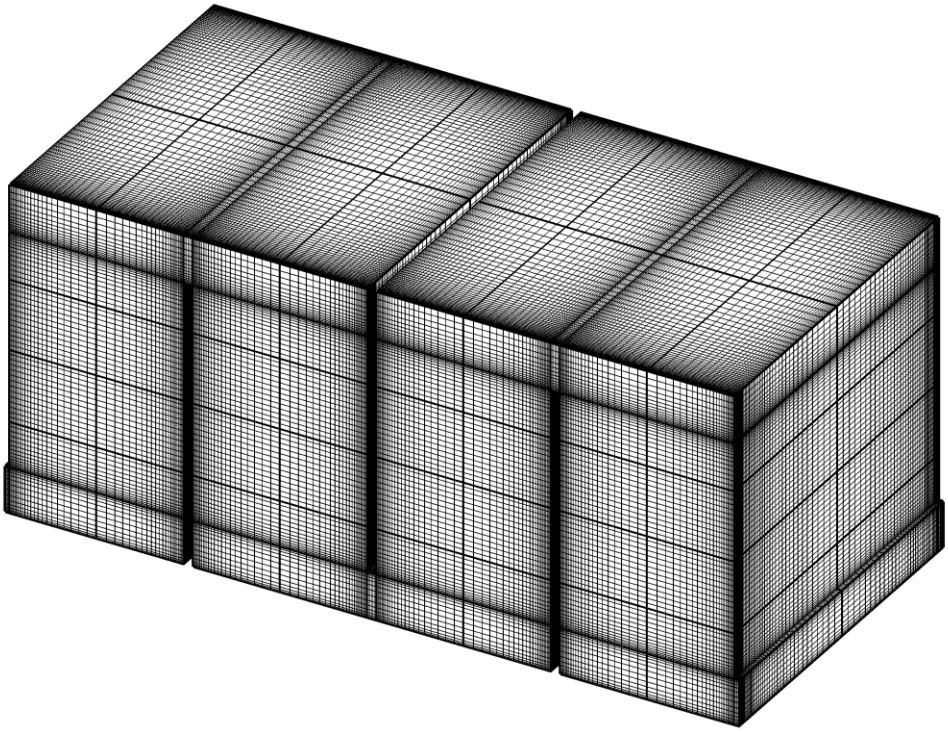

(a)

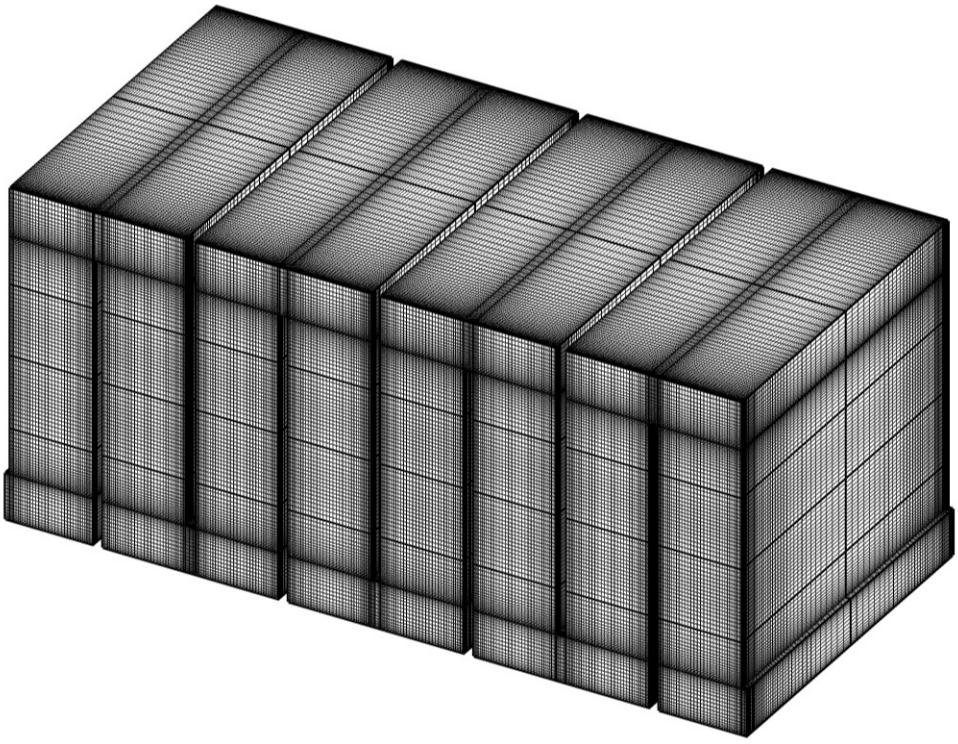

(b)

Figure 3.5 Block-structured grids for CBSMC models: (a) NS and (b) HS

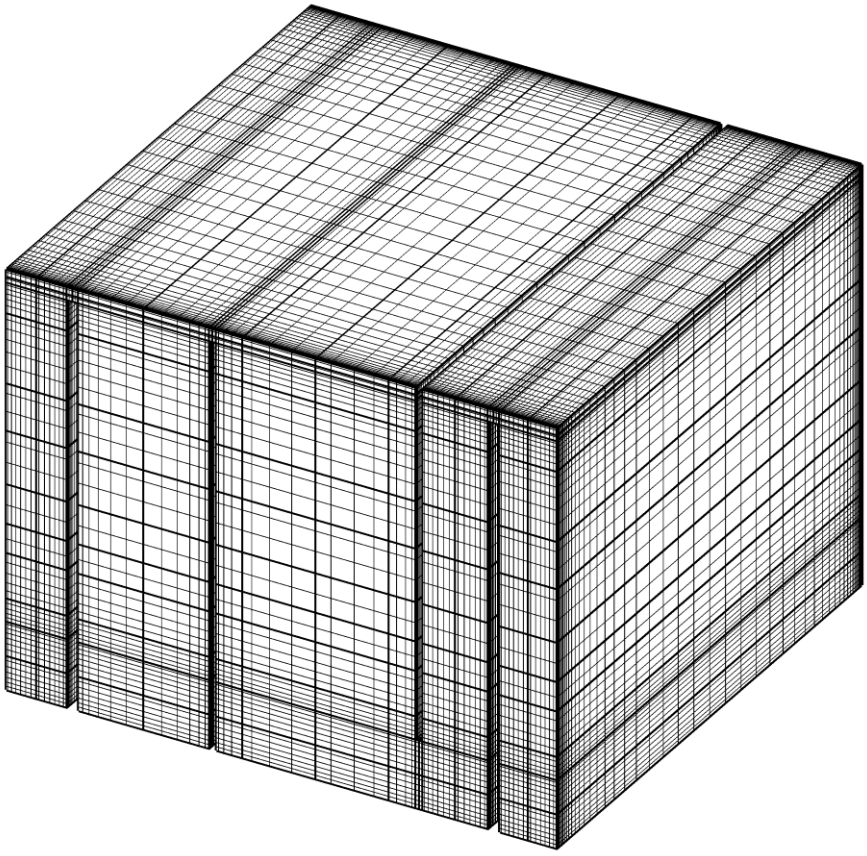

Figure 3.6 Block-structured grids for VBSM-3W models (only every 5th grids are shown)

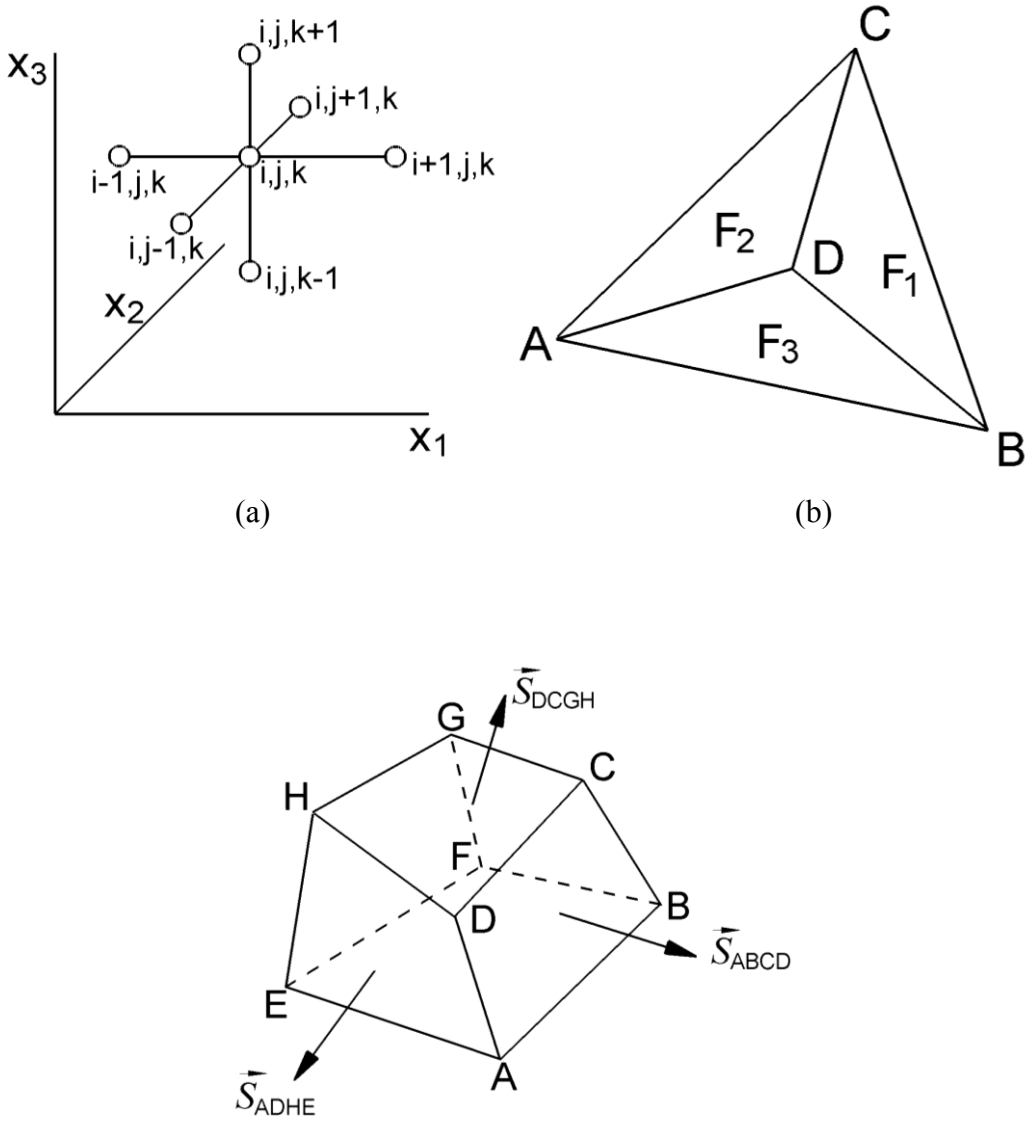

Figure 3.7 Equation discretization types: (a) FDM, (b) FEM, and (c) FVM (Stoesser, 2001)

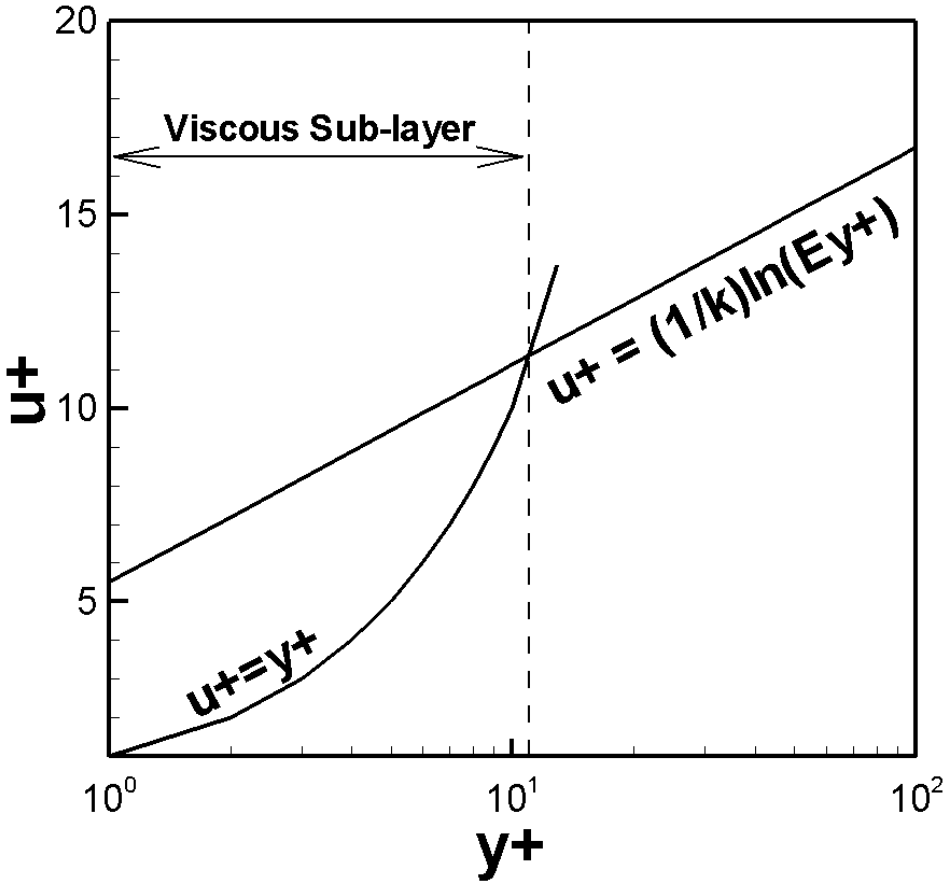

Figure 3.8 Turbulent boundary layer

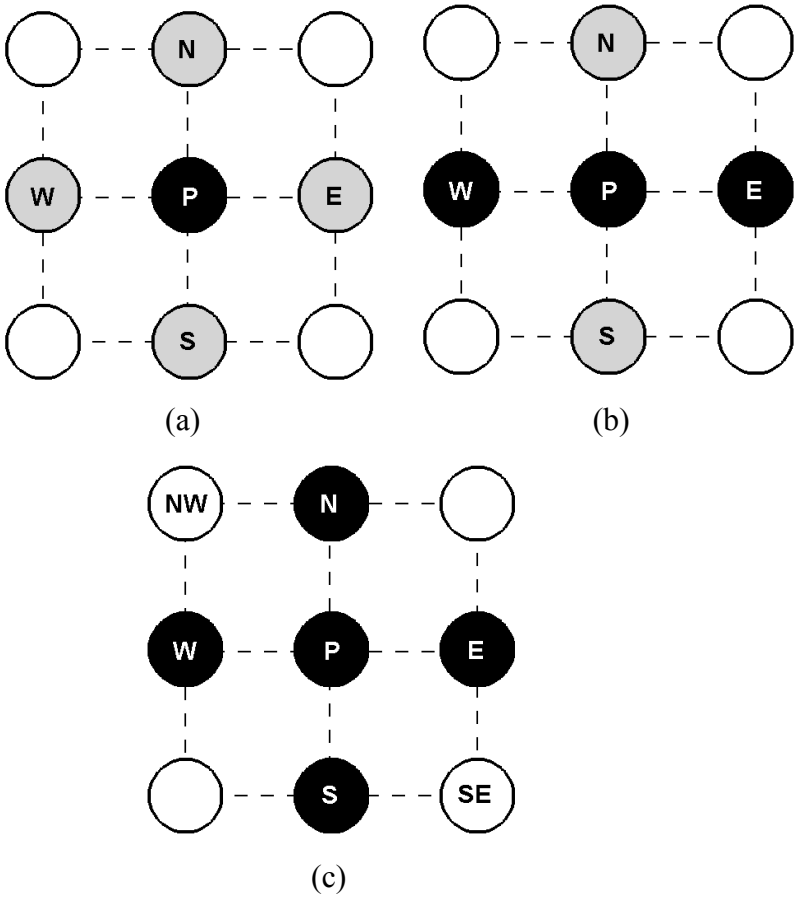

Figure 3.9 Schematic representation of algebraic solver types: (a) Gauss-Seidel (b) TDMA or ADI, and (c) SIP (Kim, 1998) (black circle= unknown; gray=guessed, and white=non-participating)

CHAPTER 4

LARGE EDDY SIMULATION OF FLOW AND TRACER TRANSPORT IN MULTI-CHAMBER OZONE CONTACTORS

4.1 Introduction

Past studies have suggested that the hydrodynamics of an ozone contactor has a significant impact on its process efficiency (Kim et al. 2004; Tang et al. 2005; Kim et al. 2007a). A plug flow is the preferred flow condition in order to maximize the inactivation of pathogens such as *Cryptosporidium parvum* oocyst and to minimize the formation of undesired disinfection byproducts such as bromate. Consequently, a meandering plug flow through multiple chambers in series, typically divided by vertical baffles, has been the target flow condition for most ozone disinfection reactors. Despite the intent of the design, however, non-ideal flow conditions may exist in multi-chamber ozone contactors, resulting in a significant deviation of the hydrodynamics from that of plug flow.

A recent three dimensional laser induced fluorescence (3DLIF) study by Kim et al. (2008) suggested that flow irregularities such as short-circuiting (i.e. a preferential flow through a part of the reactor), internal recirculation within the chamber, and dead zone formation (i.e. area of the reactor with insufficient mixing) could be prevalent in multi-chamber ozone contactors. In particular, the baffle spacing (i.e. the distance between consecutive baffle walls) was identified as one of the critical design factors that determine the extent of short-circuiting and recirculation. A corresponding reactive

transport model simulation further suggested that these flow conditions would have a significantly negative impact on the overall disinfection efficiency of the multi-chamber reactor (Kim et al. 2008). Heathecote et al. (1994) conducted tracer studies for several hanging baffle designs based on a down scaled ozone contactor model and found that an efficient baffle arrangement would have a significant enhancement in tracer residence time. An earlier Laser Doppler Anemometer study by Shiono and Teixeira (2000) also suggested that a multi-chamber reactor used for chlorine disinfection with horizontally meandering flow could be also susceptible to the formation of recirculation within the chamber. The above evidences were obtained from a limited set of experiments performed using lab-scale model reactors, thus the extrapolation of the findings to a wider range of design options and operating conditions is inherently limited.

Computational fluid dynamic (CFD) models have been applied to verify the existence of these flow irregularities in multi chamber reactors, with the ultimate goal of developing a versatile tool for reactor flow diagnosis and design. Two dimensional CFD simulations with a number of different turbulence models (e.g., depth-averaged viscosity model, k-ε model, and Smagorinsky model) and different convection schemes (*e.g.*, first- or third-order upwind schemes and QUICK scheme) have been attempted for flow simulation of multi-chamber chlorine contactors (Wang et al. 1998a, 1998b; Gualtieri 2006a, 2006b, 2007). For multi-chamber ozone contactors, Henry and Freeman (1995) applied a two dimensional finite element analysis (FEA) based on the Reynolds-Averaged Navier Stokes equations (RANS) and standard k-ε turbulence model. They found that an additional guide vane would improve the disinfection performance more than corner and edge curvature modifications. Furthermore, a three dimensional CFD

simulation was conducted by Murrer et al. (1995) to investigate mixing behavior at three different spanwise locations by modifying the position of gas injection in an existing ozone contact tank.

Past CFD simulations on ozone contactors have been exclusively based on RANS, in which only the mean velocity field is computed and all the unsteady effects of turbulence are accounted for by turbulence model. RANS modeling is appropriate in flows where the instantaneous flow behaves similarly compared to the time-averaged flow. However, the complexity of turbulence in flows that are dominated by large-scale turbulence structures poses a significant challenge to any RANS turbulence model. For instance, the flow around bluff bodies (e.g., baffle walls in a multi-chamber reactor) may not be accurately simulated by a RANS-based model (Rodi et al., 1997).

An alternative to RANS-based CFD models is the method of Large Eddy Simulation (LES). LES lies between two extremities of CFD approaches, *i.e*. models based on the aforementioned RANS equations and a direct numerical simulation (DNS). A DNS calculates all turbulent scales (spatial and temporal) directly; therefore DNS involves extremely high computational costs, which make this an impractical choice except for simple geometries or fundamental studies on turbulence. In contrast, LES aims at simulating large-scale flow structures that are directly affected by the geometry and boundaries. Hence, LES offers a substantial increase in accuracy over time-averaged approaches, particularly when momentum transfer processes are dominated by large-scale turbulent structures (Rogallo and Moin, 1984) at much less computational cost than DNS. Furthermore, providing relatively high spatial and temporal resolution, LES delivers an enormous amount of information on the mean and instantaneous flow field.

The objective of the present study is to employ the LES method for the first time to simulate the unsteady and complex turbulent flow behavior in open channel, multi-chamber ozone contactors. LES is of particular interest, since the experimental work by Kim et al. (2008) suggested that the flow in multi-chamber reactors was governed by large-scale turbulent structures, such as internal recirculation, and short-circuiting. Two design variations with different baffle spacings are examined. The dimensions and the flow conditions are identical to those of the experimental study performed with scaled model contactors by Kim et al. (2008).

4.2 Numerical Approach

The LES code (Hydro3D-GT) used in this study is the in-house code which employs a finite volume method on a Cartesian grid with collocated variable arrangement. The convection and diffusion terms in the Navier-Stokes equations are approximated by central differences with second-order accuracy. An explicit 3-step Runge–Kutta scheme is used to discretize the equations in time. The Smagorinsky sub-grid scale (SGS) model (Smagorinsky, 1963) is employed to calculate sub-grid stresses. The Hydro3D-GT code solves the following filtered Navier-Stokes equations for incompressible fluid flow (Pope, 2005):

$$\frac{\partial u_i}{\partial x_i} = 0 \qquad \textbf{(4.1)}$$

$$\frac{\partial u_i}{\partial t} + \frac{\partial u_i u_j}{\partial x_j} = -\frac{\partial p}{\partial x_j} + \frac{\partial (2\nu S_{ij})}{\partial x_j} - \frac{\partial \tau_{ij}}{\partial x_j} \qquad \textbf{(4.2)}$$

$$S_{ij} = \frac{1}{2}\left(\frac{\partial u_i}{\partial x_j} + \frac{\partial u_j}{\partial x_i} \right) \quad \textbf{(4.3)}$$

$$\tau_{ij}^{a} = \tau_{ij} - \frac{2}{3}\delta_{ij} k_r \, (= -2\nu_t S_{ij}) \quad \textbf{(4.4)}$$

$$\nu_t = (C_s \Delta)^2 |S| \quad \textbf{(4.5)}$$

$$\Delta = (\Delta x \Delta y \Delta z)^{1/3} \quad \textbf{(4.6)}$$

$$|S| = (2 S_{ij} S_{ij})^{1/2} \quad \textbf{(4.7)}$$

where u_i and u_j (i or j = 1, 2, or 3) are the resolved velocity vectors (i.e. $u_1 = u$, $u_2 = v$, and $u_3 = w$ denoting the velocity components in x, y and z axis direction, respectively) and p is the resolved pressure divided by the density. These quantities are filtered in space. Similarly, x_i and x_j represent the spatial location vectors in x, y, and z axis direction, respectively. ν is the dynamic viscosity and S_{ij} is the filtered strain-rate tensor. The τ_{ij} term results from the unresolved sub-grid scale fluctuations and needs to be modeled by a SGS model. The Smagorinsky SGS model employed in the present study approximates the anisotropic part via τ_{ij}^{a} ('a' indicates 'anisotropic') where δ_{ij} is Kronecker delta and k_r is the residual kinetic energy. Then, an anisotropic filter, Δ, is used with characteristic filter widths, Δx, Δy, and Δz. ν_t is the sub-grid scale eddy viscosity where the Smagorinsky constant, C_s, is fixed at 0.1. $|S|$ is the characteristic filtered rate of strain.

LES simulations were performed for the laboratory-scale multi-chamber ozone reactor the flow characteristics of which were extensively evaluated using a 3DLIF technique. The twelve chamber model reactor used by Kim et al. (2008) was simplified to

a four chamber reactor with the same chamber dimension. This simplified model is referred to as a Normal Spacing (NS) model in this study, whereas another reactor with half the baffle spacing, also examined in this study, is referred to as a half-spacing (HS) model. A schematic view of the flow domain including detailed dimensions is provided in Figure 4.1.

The computational grid together with applied boundary conditions for the NS model is shown in Figure 4.2. Several preliminary simulations on successively finer grids were performed and the results of the finest grid consisting of 1,396,050 total grid points (195 x 88 x 82 in *x*-*y*-*z* direction) are presented herein. The grid is stretched toward the bottom and the baffle walls where velocity gradients are expected to be relatively steep. A no-slip boundary condition is used at these wall boundaries. The grid in the vicinity of the water surface is somewhat coarser than near the wall boundaries, since shear forces are negligible at fluid-air interfaces. Accordingly, a symmetry boundary condition is applied at this free surface. Periodic boundary conditions are used in the streamwise direction to simulate a geometrically periodic and infinitely long domain. This boundary condition prevents unwanted non-physical disturbance of the flow which is expected to occur when artificial inflow and outflow boundary conditions are applied. The Reynolds number based on the hydraulic diameter ($h_R = \sqrt{(4)(A_c)/(\pi)}$, where A_c = cross section area at the inlet sluice gate) is 2,740 for both models corresponding to one of the experiments performed by Kim et al. (2008).

Transport of a conservative tracer was simulated by solving the following three-dimensional advection-diffusion equation:

$$\frac{\partial C}{\partial t} + u_j \frac{\partial C}{\partial x_j} = D_t \frac{\partial^2 C}{\partial x_j^2} \quad \textbf{(4.8)}$$

where D_t is the turbulent diffusivity of the filtered tracer concentration, C. The tracer at constant concentration was introduced at the inlet of the reactor initially for 500 time steps (i.e. for the duration of approximately 2.35 s) to represent a pulse injection. The residence time distribution (RTD) was normalized by the total introduced tracer concentration such that the area under the curve was equal to unity. The time scale was normalized based on the theoretical residence time (τ) per chamber, which was 27.3 s and 12.8 s for the NS and HS reactors, respectively.

4.3 Results and Discussion

4.3.1 Accuracy of LES Simulation

Even though LES has already had tremendous success in accurately predicting the flow for a number of different applications, there is a need for re-assessing the accuracy of the LES approach and the numerical methods involved especially for in complex flows (Rodi et al. 1997). In this study, commonly used quality indicators such as the distribution of dimensionless grid spacing along the walls and the energy spectra of the flow were used. The quality of the utilized grids was assessed based on the distribution of dimensionless grid spacing, y^+, defined as follows:

$$y^+ = \frac{d}{\nu}\sqrt{\frac{\tau_w}{\rho}} \quad \textbf{(4.9)}$$

$$\tau_w = \mu \frac{\overline{U}}{\Delta y} \tag{4.10}$$

where τ_w is the wall shear stress, d is the distance of the first grid point off the wall, and $\overline{U}$ is the time averaged velocity at the corresponding grid node. ρ and μ are the density and the dynamic viscosity of fluid, respectively. Using the mathematically correct formulation of the no-slip wall boundary condition is justified only if the first grid point off the wall is placed within the viscous sublayer in which the effects of turbulence are negligible compared to viscous effects. In order to avoid the influence of near wall turbulence modeling, a DNS-like resolution is desired i.e. y^+ should be less than approximately 11.0. Figure 4.3 shows y^+ values near the chamber bottom and the left side wall of a baffle. The values of y^+ are consistently below 3, hence considerably smaller than 11.0, ensuring adequate near-wall resolution and justifying the no-slip wall boundary condition.

Power Density Spectra (PDS) were also examined to evaluate whether the inertial subrange of the turbulent energy transfer was adequately resolved in the present LES. Figure 4.4 shows the PDS of *x* and *z* velocity components (*u* and *w*, respectively) at selected locations, where the flow is accelerating and the turbulent energy are relatively large. The energy prevailing in large eddies with lower frequency is successively cascaded to smaller eddies with higher frequencies. The simulated decay follows the Kolmogorov's slope of $-5/3$, when the PDS is plotted versus frequency both in logarithmic scales, confirming that the energy transfer from large scales to small scales is physically realistic. A sudden drop of the spectra represents the virtue of the SGS model

dissipating the remaining energy. Noteworthy are peaks in the spectrum of the *u*-velocity signal in the NS reactor at around 200 Hz. These are small scale numerical oscillations that are caused by the higher-order central-differencing scheme used for the convective terms. These oscillations, however, do not affect the simulation results since they contain very little energy and are rather considered numerical artifacts. Using upwind-based schemes for the convective terms may remove these oscillations. However, they would also introduce numerical dissipation and considerably less accurate results at the same time.

4.3.2 Flow Characteristics

Figure 4.5 shows the distribution of time-averaged normalized absolute velocity ($\overline{U}/U_{bulk}$) along with two dimensional streamlines in the right half portion of each figure. Areas of higher velocity (white contours) are found along the outer regions of the meandering flow path (i.e. near the right side of each chamber), clearly suggesting the occurrence of short-circuiting through each chamber. As the flow exits each chamber near the bottom or near the free-surface, it accelerates to twice the average bulk velocity (U_{bulk}) due to the presence of the sharp crest of the baffles. The streamlines indicate that a large recirculation zone occupies approximately two thirds of the baffle spacing in the chambers of the NS reactor (Figure 4.5(a)). Noteworthy is the fact that the effective flow width (W_e) is approximately equal to the gate height (h) in both cases. A small counter-rotating secondary recirculation zone occurs at the corners of bottom and the baffle wall on both sides of the baffle. Such a secondary recirculation zone is not observed near the water surface. A third cell is observed at the downstream side and near the free end of the baffle the streamlines of which resemble those of the flow in a lid driven cavity (Ghia et

al., 1982). These counter- rotating inner cells are driven by the larger clockwise rotating outer cell.

The HS reactor exhibits similar flow features with some noteworthy differences. The effective flow width is very similar, while the size of the primary recirculation zone is considerably narrower comparing to the NS model. In addition, the primary recirculation zone of the HS model does not occupy the entire chamber height (*H*), in contrast to the NS-model, but extends only about two thirds of the height of the baffle wall. Flow acceleration is also observed as the flow passes underneath or over the baffle. The secondary recirculation zone in the bottom/baffle corner is similar, while another secondary cell appears near the free surface. A counter-clockwise cell near the free end of the baffles is absent in the HS model suggesting that the shear that is induced by the main cell of the HS model is weaker than that of the NS model.

The profile of time- and spanwise-averaged and normalized flow-through velocity ($\bar{v}/U_{bulk}$) in *y* direction at three different vertical locations in the chamber of both NS and HS reactors are presented in Figure 4.6. The velocity profiles clearly deviate from that of the plug-flow (i.e. uniform velocity profile), with the presence of severe short-circuiting (i.e. flow with locally high velocity near the wall opposite of the chamber entrance at x/W > 0.4-0.5) and recirculation (*i.e.* reversed flow at x/W < 0.4-0.5). Near the chamber bottom (Figure 4.6(a), y/H = 0.27), the absolute values of the velocity peaks are smaller in the NS reactor compared to the HS reactor. However, the area over which recirculation occurs is considerably larger in the NS reactor. As the flow reaches the midpoint of the chamber height (i.e. y/H = 0.5), the positive maxima become about the same, while the

recirculation nearly disappears in the HS reactor. At $y/H = 0.72$, the magnitude of the velocity difference along the baffle spacing is much greater in the NS reactor than in the HS reactor, indicating that the short-circuiting is much more severe in the former. The reverse flow is completely absent in the HS reactor at $y/H = 0.72$ and the velocity profile is closer to that of the plug flow.

Figure 4.7 presents the distribution of the instantaneous normalized absolute velocity (U/U_{bulk}) in both reactors. Although the instantaneous velocity distribution overall resembles the time-averaged velocity distribution shown in Figure 4.5, prevalence of turbulence is apparent. In particular, smaller vortices are observed in both reactors, especially along the shear layers that form between the main flow path and recirculation region. In the HS reactor, these vortices lead to a partial disruption of the main flow path. The instantaneous velocity in the main flow path reaches about 2.2 to 2.7 times the average bulk velocity, again indicating severe short-circuiting in both reactors. The profile of instantaneous normalized flow-through (v/U_{bulk}) in the *y*-direction at three different vertical locations in the first chamber of the NS (upper figures) and HS (lower figures) reactors are compared with time-averaged profiles in Figure 4.8. The instantaneous velocity obviously deviates from the mean value and, for the moment depicted in this figure, the instantaneous velocity maxima are above the mean values. Whereas the maxima of instantaneous velocities are about 5 times higher than the plug flow velocity in the NS chamber, they are about 3 times in the HS reactor. At $y/H = 0.72$, this ratio is still approximately 5 in the NS model while it is decreased to a factor of 2.2 in the HS model, which is mainly due to the absence of recirculation at this height.

Streamlines along the *y-z* planes at five different streamwise locations within the first chamber shown in Figure 4.9 suggest that the flow field is highly three-dimensional. At $x/W = 0.0$ (i.e. the plane of the reactor entrance), two small counter-circulating vortices near the side walls are observed in both reactors. At $x/W = 0.25$, these vortices are still present in the NS model and a general downward movement (i.e. as a result of the main recirculation zone) is observed. There is a nodal point at $z/L = 0.5$ and $y/H = 0.42$ at which streamlines diverge. This nodal point corresponds to the center of the main streamwise recirculation zone. Along the upper side of the baffle opening (i.e. $y/H \approx 0.1$), the streamlines from the recirculation zone and those from incoming fluid converge. In contrast, the small vortices near the entrance region are dissipated at $x/W = 0.25$ and a new recirculation zone forms near the free surface in the HS reactor. Converging streamlines, similar to the NS reactor, are found along the baffle opening height and a pair of nodal points corresponding to the centre of the streamwise recirculation zone is also found relatively close to the chamber bottom ($y/H \approx 0.2$). Above approximately half the chamber depth (i.e. $y/H > 0.5$), the flow exhibits an upward motion. At half the baffle spacing (i.e. $x/W = 0.5$), a pair of large, symmetric, and counter-rotating vortices are observed in the NS reactor again suggesting three-dimensionality and fluid entrainment. Near the bottom of the chamber, the fluid exhibits an upward movement over the entire width. The secondary streamlines of the HS model suggest that the flow is almost two-dimensional at $x/W = 0.5$. At $x/W = 0.75$ and 1.0 for both reactors, upward motion is found over the entire baffle spacing. The small vortices near the free surface are almost dissipated at $x/W = 1.0$.

4.3.3 Tracer Transport

Figure 4.10 presents snapshots of the distribution of instantaneous normalized tracer concentration as predicted by the LES (left) and as observed in the laboratory (right). The experimental 3DLIF image was adopted from Kim et al. (2008). It has to be noted that, although the flow conditions are identical, the amount of tracer introduced into the reactor is less in the LES, which explains the discrepancy between experiment and simulation (especially in the first chamber). Nevertheless, there is a fairly good qualitative agreement between the observed and the predicted concentration distributions in the second to fourth chambers. Higher concentration (brighter contour) is found near the baffles or near free surface, whereas lower concentration (darker contour) in the centre. The concentration distributions support the occurrence of the aforementioned flow behaviors i.e. short-circuiting and occurrence of a large recirculation region in each chamber.

Figure 4.11 shows the instantaneous distribution of iso-concentration surface (i.e. the surface with tracer concentration higher than 1% of input concentration) as a function of time. These images again confirm the occurrence of non-ideal flow behavior. The short-circuiting is observed as a distinctive plume, for example, in the second chamber of the NS reactor (upper series) at t = 10.1 s. Internal recirculation and the accompanying dead zone are apparent in the images taken at 90.5 s (the first chamber) and 114.2 s (the second chamber). As a result of non-ideal flow, the tracer is widely distributed across the NS reactor: some parts of the injected tracer has already escaped the reactor while other parts are still remaining in the inlet region (e.g., images at t = 23.5 s and 43.7 s). Consistent with previous discussions, the short-circuiting is less obvious in the HS model.

Consequently, the tracer is much more widely distributed across the NS reactor compared to HS reactor. For example, at t = 10.1 s, the tip of the tracer plume in the NS reactor already reached the half of the volume of the reactor. In marked contrast, the tracer plume mostly remained in the second chamber in the HS model at the same elapsed time. At t = 23.5 s, the tracer in the NS model is about to exit the reactor, while the HS tracer is only halfway through. At t = 114.2 s, while tracer still occupied 3 out of 4 chambers in NS model, most tracers left the HS reactor.

4.3.4 Residence Time Distribution (RTD) Analysis

Figure 4.12(a) presents RTDs experimentally determined by Kim et al. (2008) and those simulated by the LES for both reactors. Note that the reactor used in the experiment consists of 12 chambers with baffle spacing equal to that of the NS reactor. Since the periodic boundary condition used in the present LES simulation does not accurately represent the inlet flow condition of the laboratory experiments, the RTDs for the first and the fourth chambers do not agree well. However, magnitude and shape of the LES computed RTD curves match the observations very well for the second and the third chambers, in which the effect of boundary condition is minimal. In particular, the presence of a sharp short-circuiting peak and a secondary peak that result from internal recirculation (i.e. the tracer exiting the chamber after single recirculation) are noticeable in both experimental RTDs and LES RTDs (for NS reactor). The RTD curves obtained for the HS reactor show a noticeable difference. The RTD from the first chamber is characterized by a single short-circuiting peak which occurs slightly later than that in the

NS reactor. No secondary peak is detectable as internal recirculation is less severe. The RTD curves obtained at later chambers gradually become a symmetrical Gaussian-shaped curve centered at around $\theta = 1.0$. Overall, the RTD curves become closer to that of a Plug Flow Reactor (PFR) as the number of chambers increases, diluting the effect of non-ideal mixing condition in each chamber (i.e. gradual disappearance of short-circuiting peak). The simulation also suggests that the reactor with narrower baffle spacing exhibits the RTD much closer to that of a PFR than the reactor with wider baffle spacing.

Cumulative RTD (F) curves are obtained by integrating the RTD curves in Figure 4.12, and the t_{10}/τ values are evaluated (Figure 4.13). Note that t_{10} represents the time required for 10% of the tracer injected as a pulse to exit the reactor. This is commonly used as a characteristic time to evaluate the disinfection credit according to the current regulations (USEPA, 1999). The t_{10}/τ of the NS reactor is 0.3, which is much smaller than t_{10}/τ = 0.7 of the HS reactor. According to the disinfection reactor baffle classification by the USEPA (1999), the NS reactor would be classified as a poor baffling condition reactor in which no baffle is typically installed. This result suggests that even though the reactor is designed as a multi-chamber, the occurrence of non-ideal mixing behavior could have a detrimental effect on the overall hydrodynamics of the reactor when the baffle configurations are not properly designed. A recent study by Kim et al. (2008) also suggests that a full-scale ozone contactor with 10 chambers is best represented with 7 Continuous Stirred Tank Reactors (CSTRs) in series. The HS reactor, according to the same classification, would be considered as the superior baffling reactor. With respect to regulatory compliance (USEPA, 1991), this reactor is preferred for a greater disinfection credit. This flow condition also helps minimize the process

overdesign and reduce the formation of disinfection byproducts such as bromate (Roustan et al., 1993; Do-Quang et al., 2000; Kim et al., 2007b).

4.4 Conclusions

The LES results suggest the occurrence of deficient flow conditions and non-ideal solute transport behaviors in the two multi-chamber ozone contactors examined herein. Specifically, the flow through these reactors is characterized by the presence of extensive short-circuiting from one chamber to the next through a relatively narrow baffle gap, large internal recirculation that contributes to backmixing and a dead zone in the center of each chamber. These observations are consistent with the experimental findings by Kim et al. (2008) made on a scale reactor with the same dimensions and flow rate as used in this study. The LES results also suggest that the flow is highly three dimensional with a pair of symmetric counter-rotating secondary vortices and nodal points in the centre of the recirculation zones.

Considering that multi-chamber design is intended to provide plug flow conditions, above findings conclude that careful design is necessary to avoid the occurrence of non-ideal hydrodynamics and significant deviation of the flow from the original design intent. The LES results show that these hydrodynamic deficiencies could be partially prevented by decreasing the baffle spacing. The present LES was performed for only two representative designs and other design options such as the dimension of the baffle inlet height and flow rate need to be studied further. Nevertheless, this study

showed that LES can be a useful tool for new plant design as well as retrofitting existing reactors for better process efficiency.

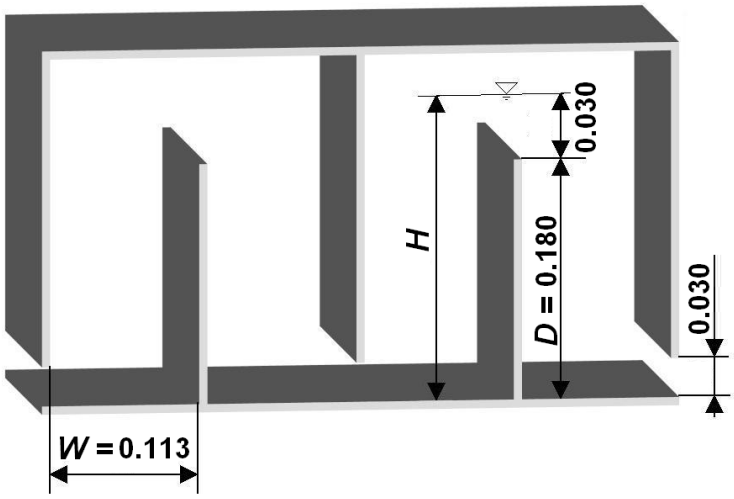

(a)

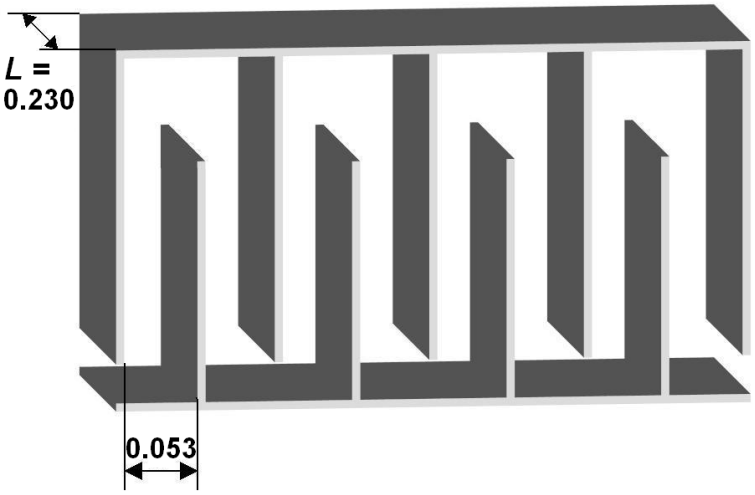

(b)

Figure 4.1. Schematics of the model ozone contactors with (a) Normal Spacing (NS) and (b) Half Spacing (HS)

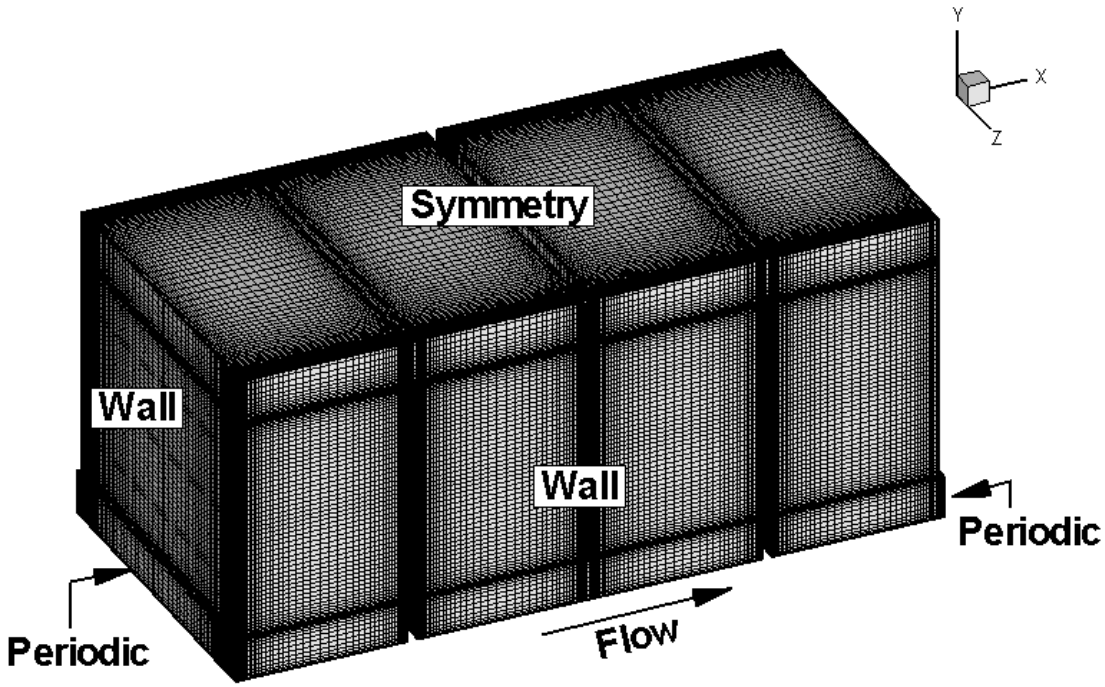

Figure 4.2. Grid resolution and boundary condition setups for the numerical model (NS reactor)

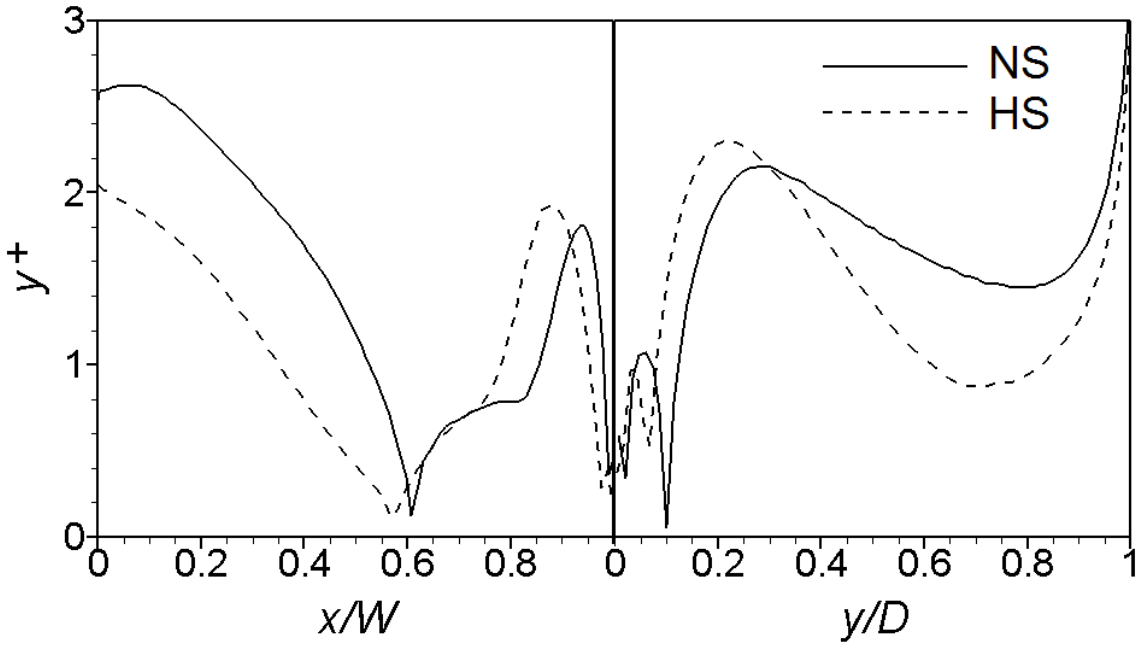

(a) (b)

Figure 4.3. y^+ comparison: (a) near the chamber bottom; (b) near the vertical baffle wall

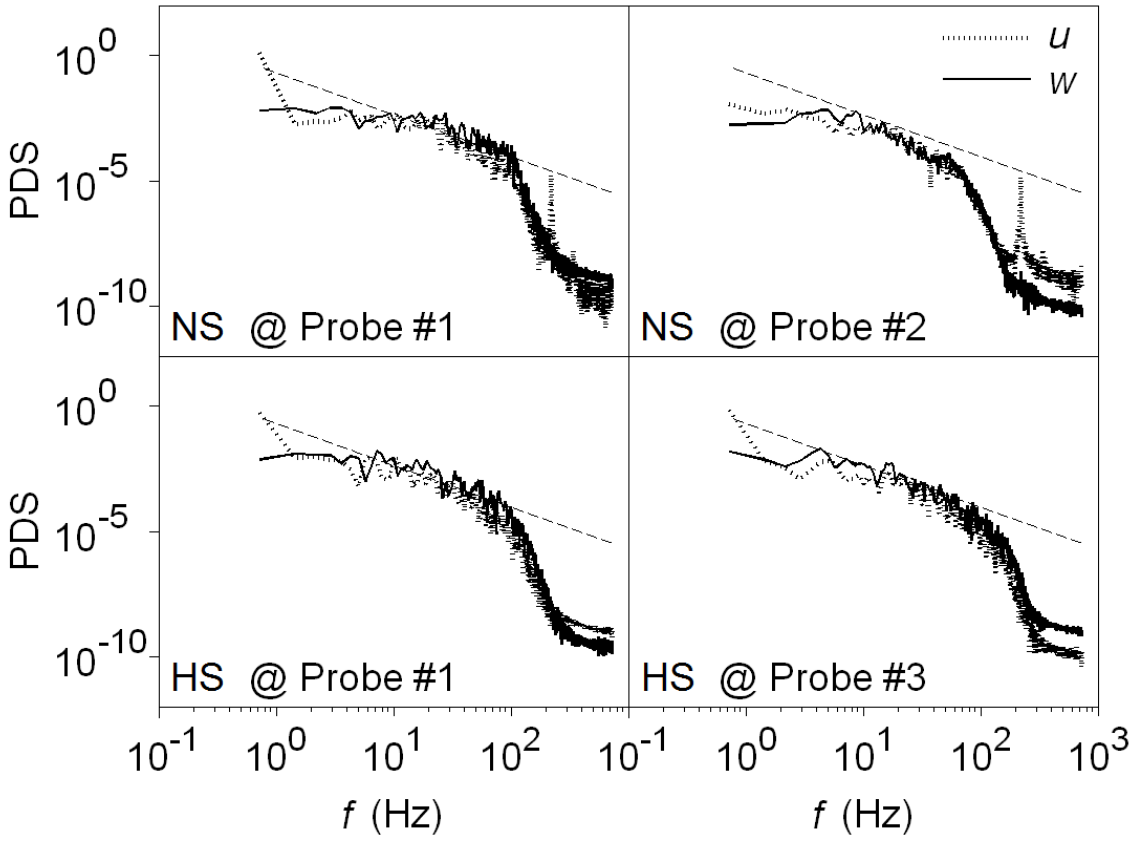

(a)

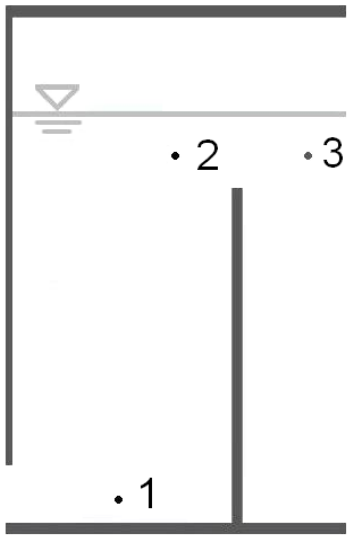

(b)

Figure 4.4. PDS of "*u*" and "*w*" velocity: (a) PDS at each point; (b) location of each extraction point

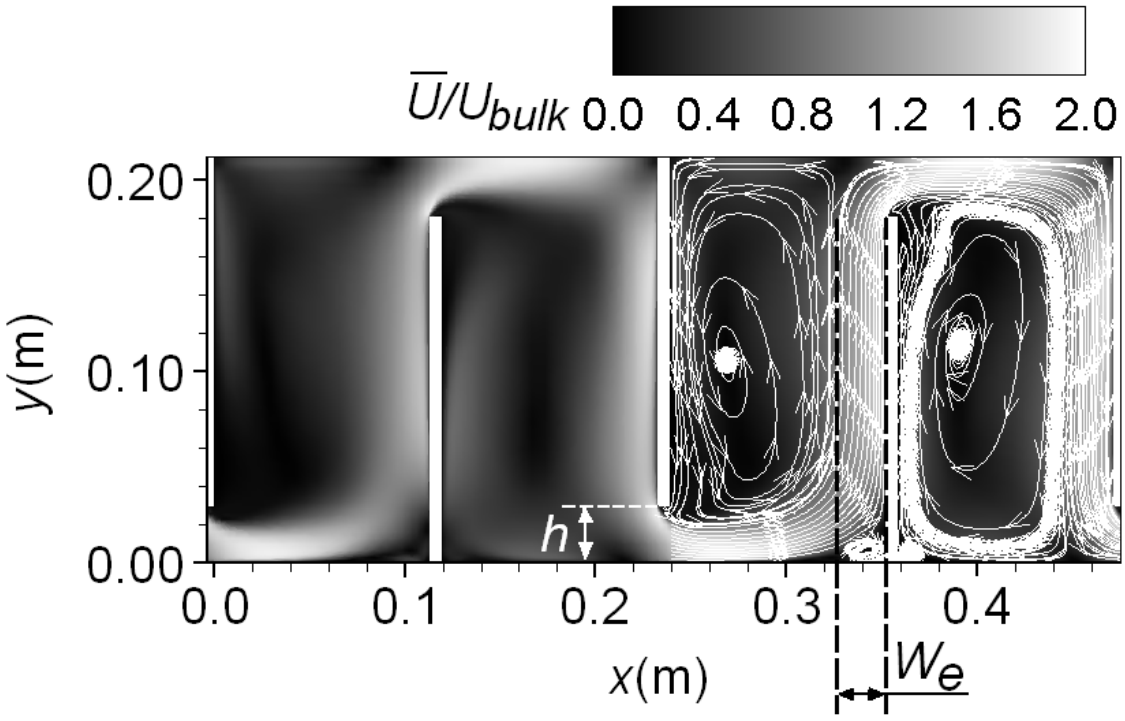

(a)

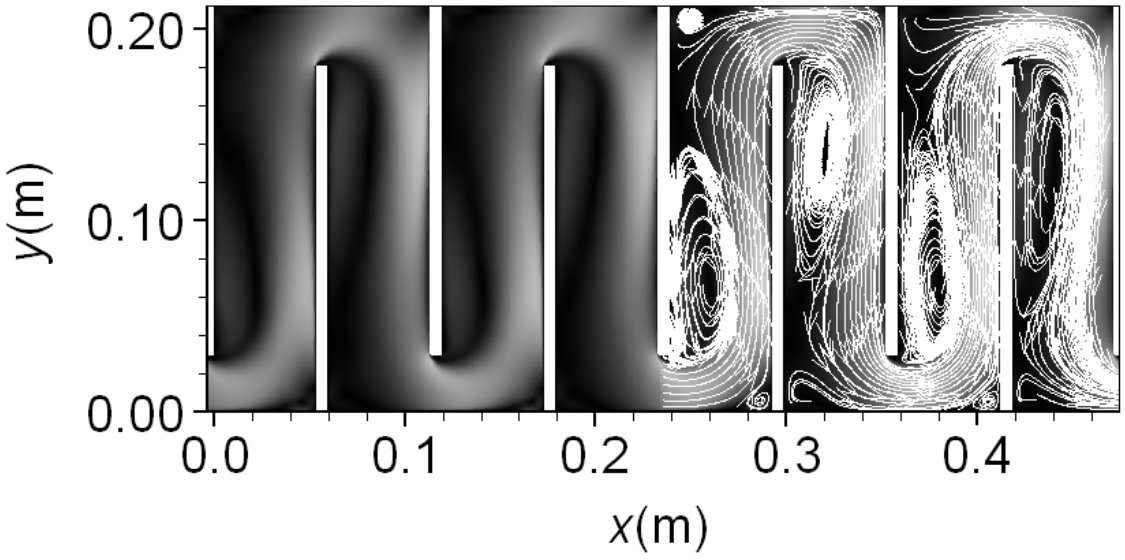

(b)

Figure 4.5. Time averaged absolute velocity distribution and streamline at center plane (z/L = 0.5): (a) NS; (b) HS

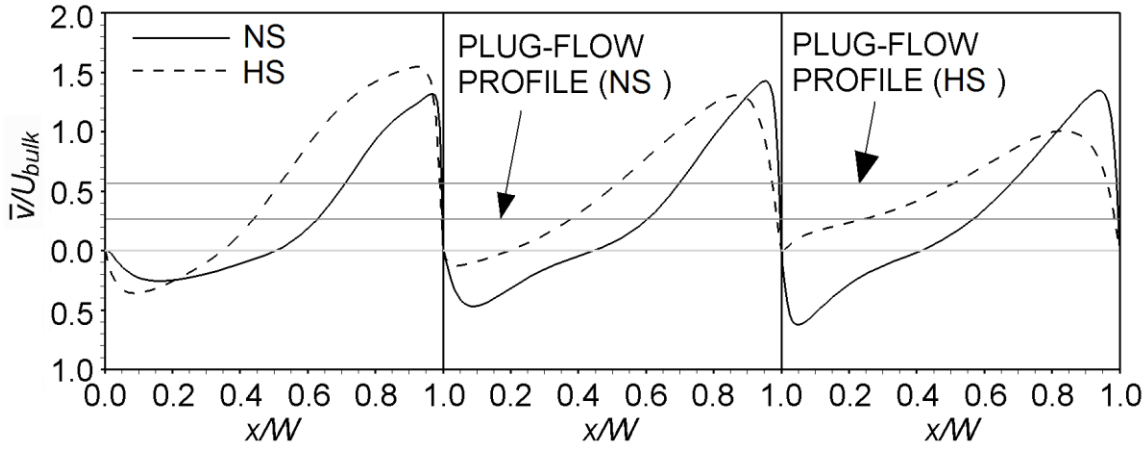

(a) (b) (c)

Figure 4.6. Time and span-wise averaged through-flow velocity distribution on a line along the baffle spacing (W): (a) $y/H = 0.27$; (b) $y/H = 0.5$; (c) $y/H = 0.72$

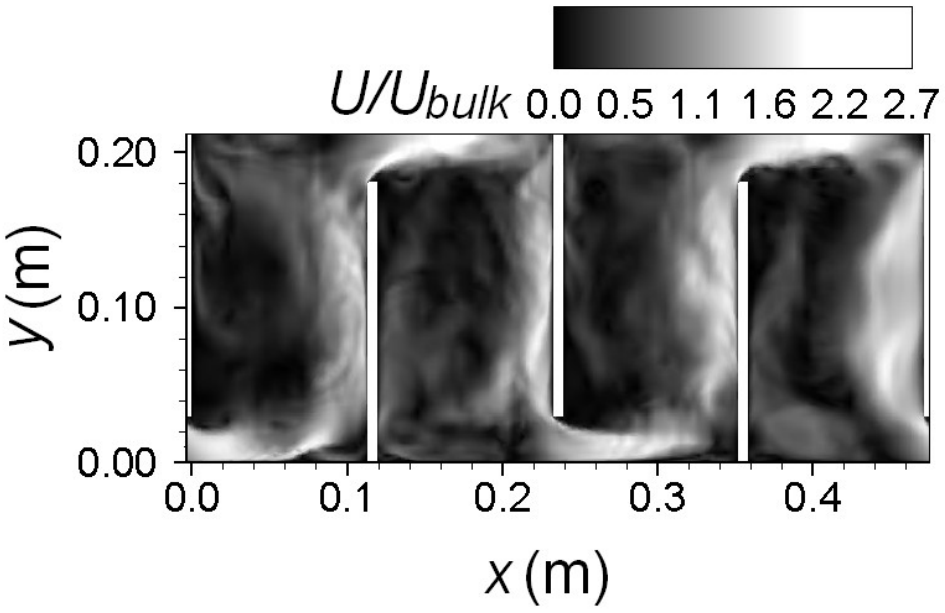

(a)

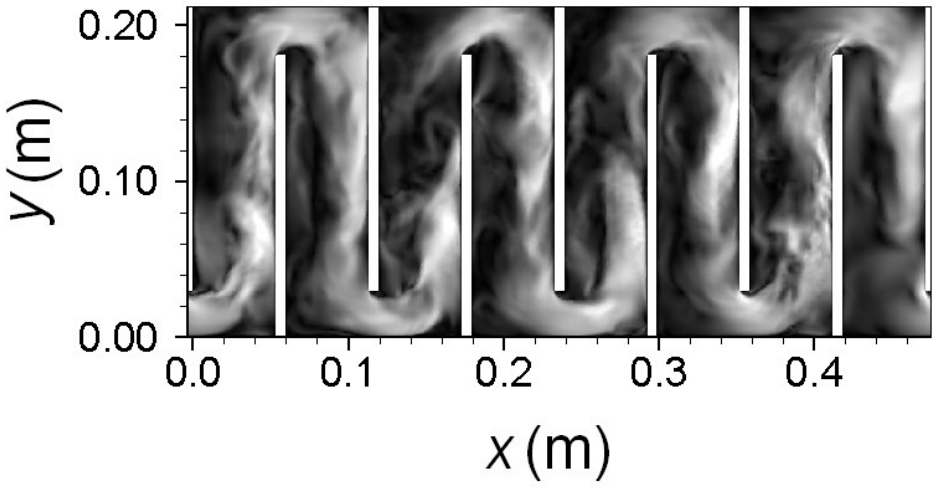

(b)

Figure 4.7. Instantaneous absolute velocity distribution at center plane (z/L = 0.5): (a) NS; (b) HS

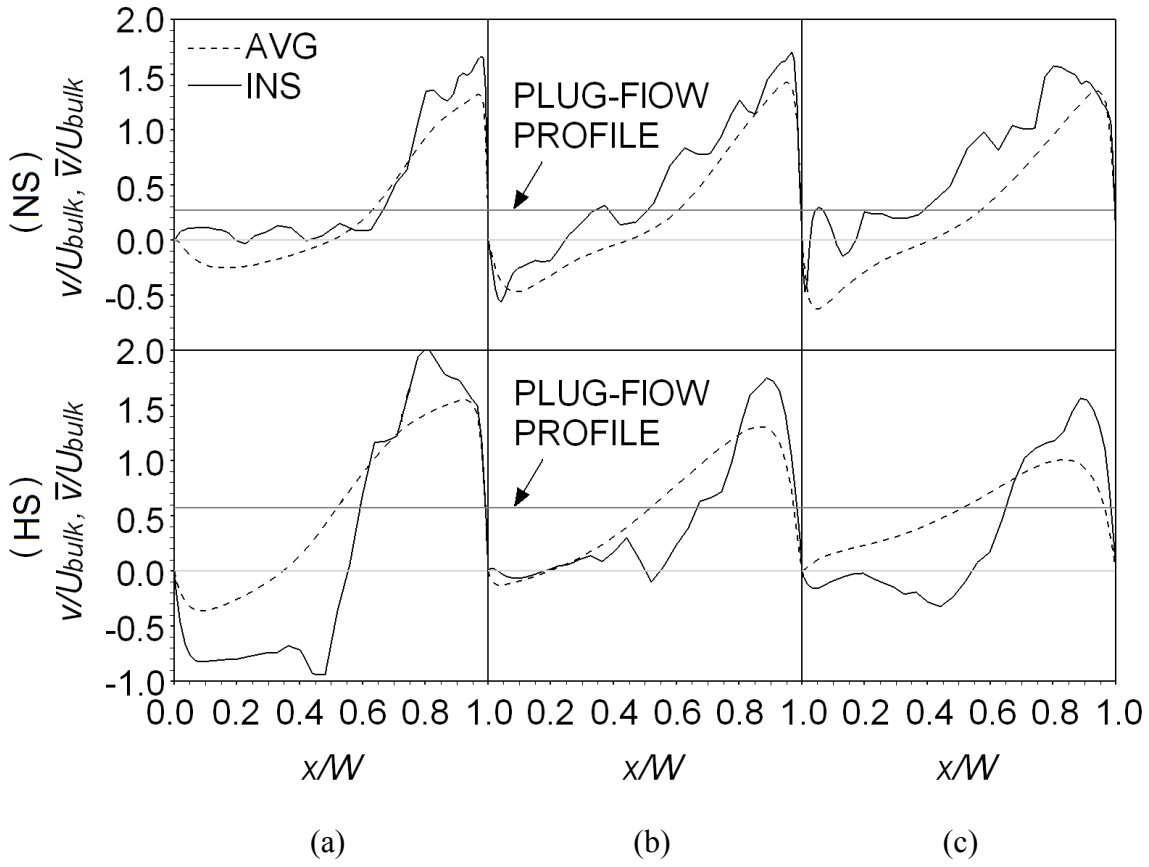

Figure 4.8. Instantaneous through-flow velocity distribution on a line along the baffle spacing (W): (a) $y/H = 0.27$; (b) $y/H = 0.5$; (c) $y/H = 0.72$

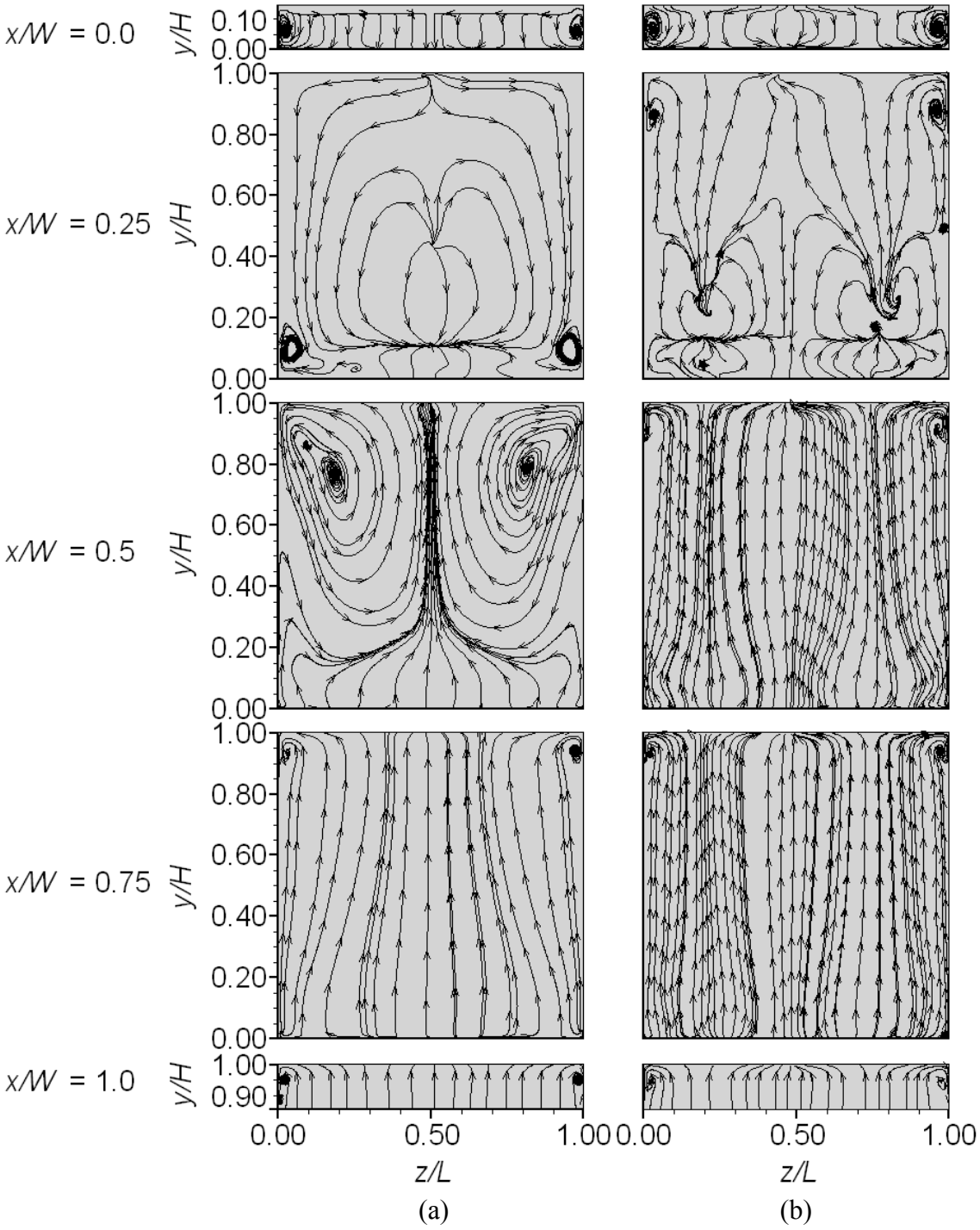

Figure 4.9. Time averaged streamlines on the span-wise planes: (a) NS; (b) HS

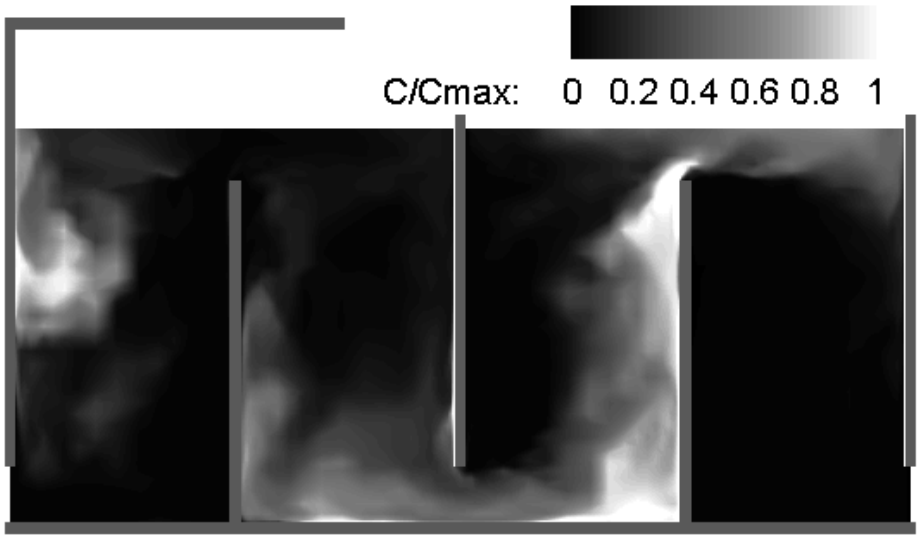

(a)

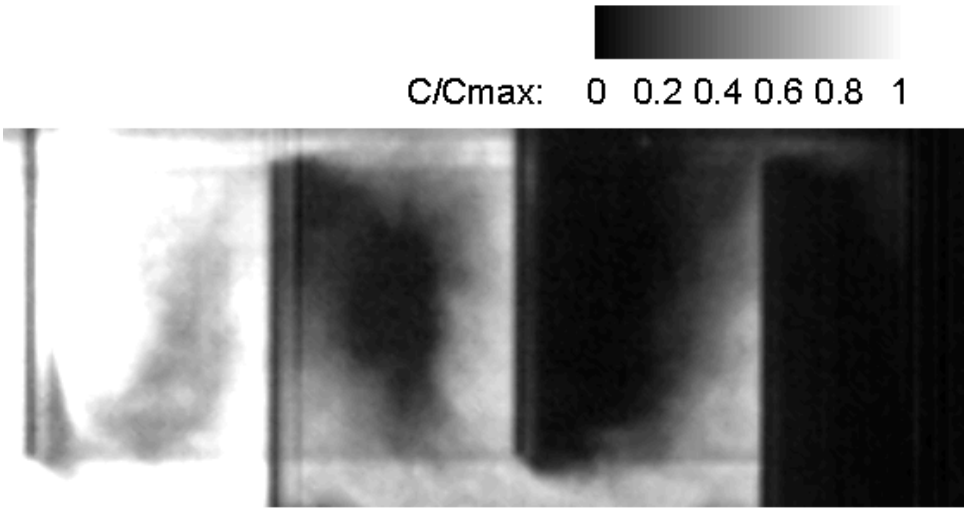

(b)

Figure 4.10. (a) Computed and (b) measured tracer distribution in the chamber at an instant in time

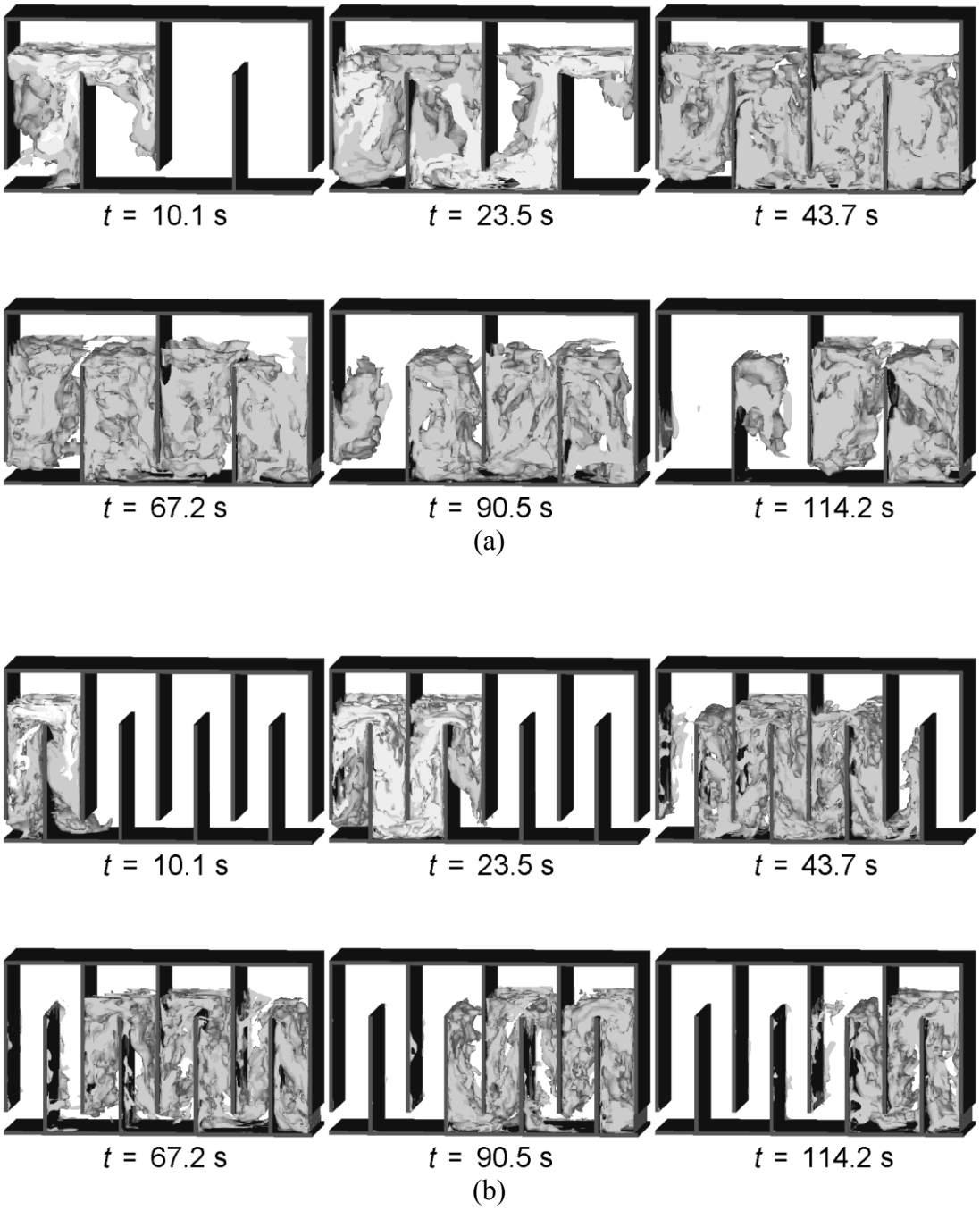

Figure 4.11. Above 1% concentration iso-surface of tracer transportation at selected instants in time: (a) NS; (b) HS

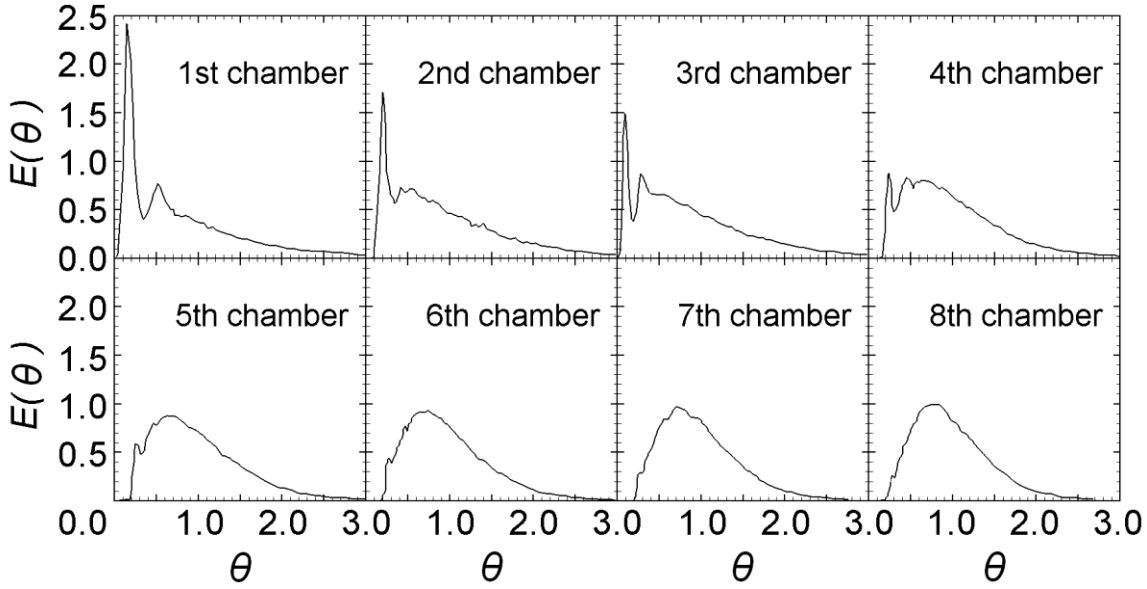

(a)

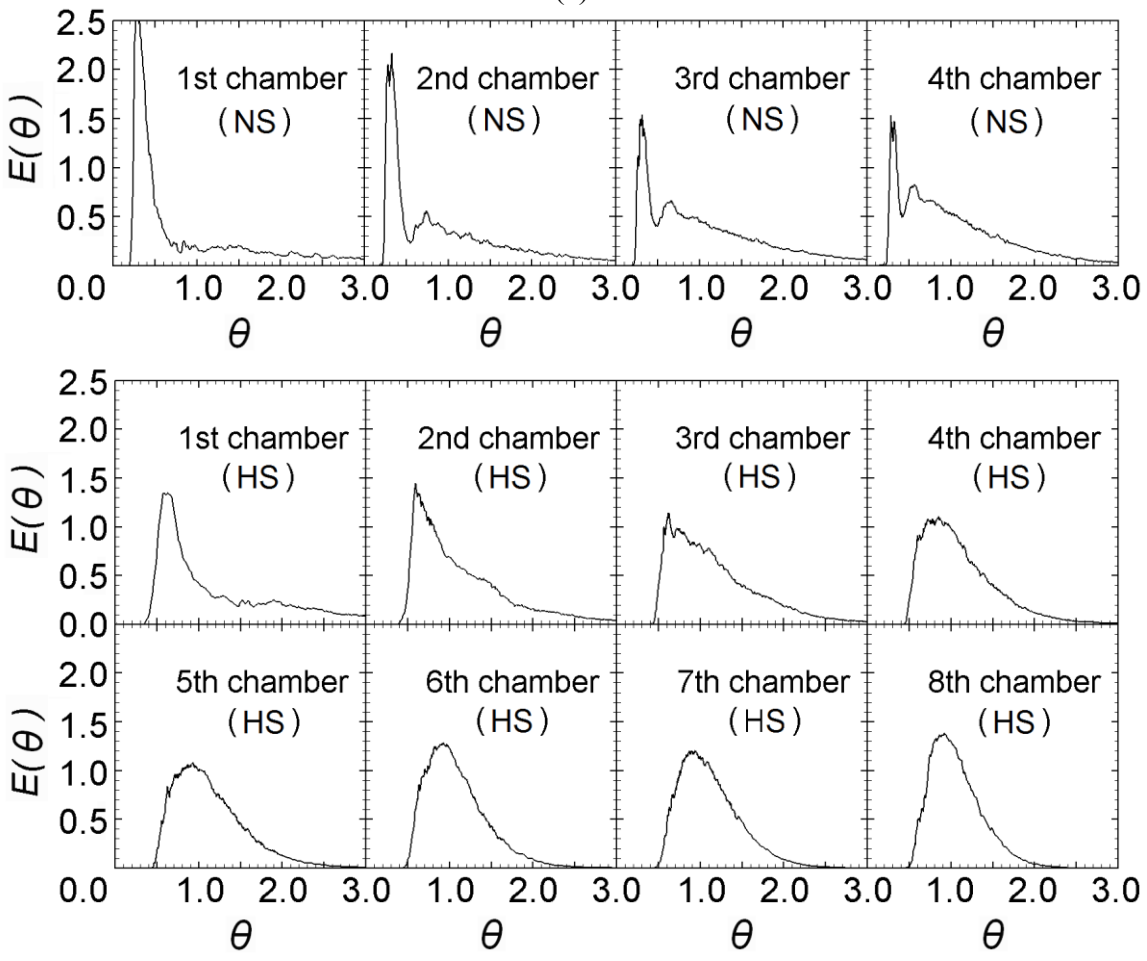

(b)

Figure 4.12. Tracer RTD graph extracted at the gate of each chamber: (a) Measured; (b) Computed

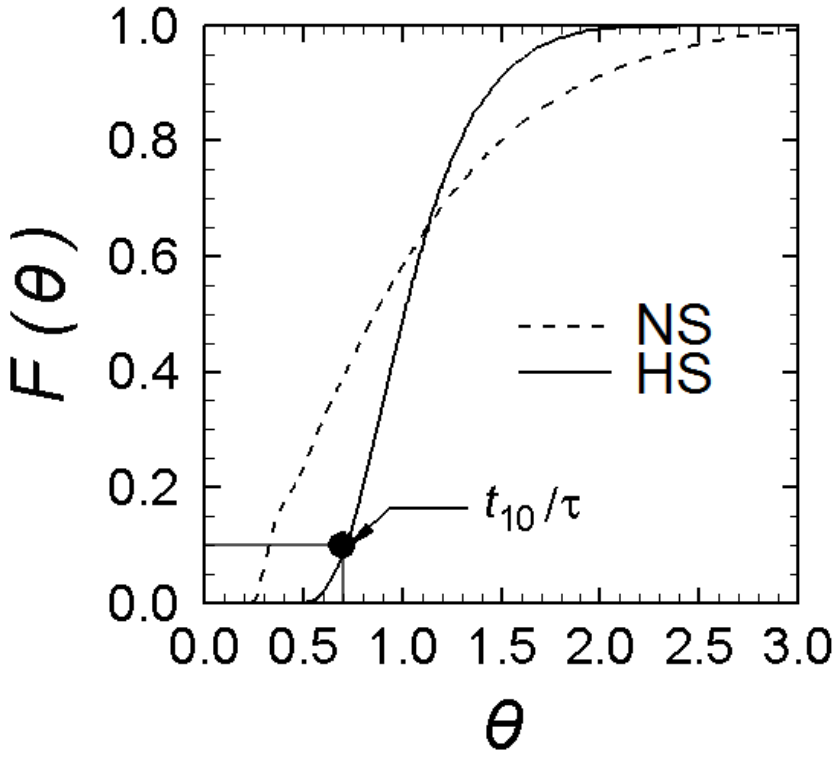

Figure 4.13. Cumulative tracer RTD graph at the exit gate of reactor for both models

CHAPTER 5

LES AND RANS MODELING OF FLOW IN AN OZONE CONTACTOR: MEAN AND INSTANTANEOUS TURBULENT FLOW CHARACTERISTICS

5.1 Introduction

The hydrodynamics of an ozone contactor affects its process efficiency significantly (Kim et al. 2004; Tang et al. 2005; Kim et al. 2007a). In order to maximize the inactivation of pathogens and to minimize the formation of undesired disinfection byproducts, a plug flow (i.e. no fluid shear and hence no turbulence) through multiple chambers in series divided by baffles is the ultimate condition. However, non-ideal flow conditions far from the hydrodynamics of plug flow may exist contrary to the design intention.

A recent three dimensional laser induced fluorescence (3DLIF) study (Kim et al. 2008) and an earlier Laser Doppler Anemometer study (Shiono et al. 2000) suggest that flow irregularities such as extensive short-circuiting (i.e. a preferential flow through a part of the reactor), internal recirculation within the chamber, and dead zone (i.e. the area in which insufficient mixing forms) might be prevailing in multi-chamber ozone contactors. In addition, a reactive transport model simulation by Kim et al. (2008)

suggests that this irregular flow condition would deteriorate the overall disinfection efficiency significantly.

The above evidences were analyzed out from the limited set of experiments restricting the extrapolation of the findings to a wider range of operating conditions. Computational fluid dynamic (CFD) models have been applied to verify the existence of these flow irregularities in multi-chamber reactors. Two dimensional CFD simulations with a number of different turbulence models (e.g., depth-averaged viscosity, k-ε, and Smagorinsky model) and different convection schemes (e.g., first- or third-order upwind and QUICK scheme) have been attempted for flow simulation of multi-chamber chlorine contactors (Wang et al. 1998a, 1998b; Gualtieri 2006a, 2006b, 2007).

Past CFD simulations have been exclusively based on Reynolds Averaged Numerical Simulation (RANS). However, the complex turbulent flows dominated by large-scale turbulence structures pose a significant challenge to this turbulence models. As an alternative method, Large Eddy Simulation (LES) aiming at simulating large-scale flow structures that are directly affected by the geometry and boundaries. The objective of the present study is to employ the LES method to simulate the unsteady and complex turbulent flow behavior in open channel, multi-chamber ozone contactors. The dimensions and the flow conditions are identical to those of the experimental study performed with scaled model contactors by Kim et al. (2008).

5.2 Numerical Approach

The LES code (Hydro3D-GT) used in this study is the in-house code which employs a finite volume method on a Cartesian grid with collocated variable arrangement. The Smagorinsky sub-grid scale (SGS) model (Smagorinsky, 1963) is employed to calculate sub-grid stresses. The model SSIIM (Olsen, 2005) was also employed to perform the time-averaged RANS simulations. This model solves the Reynolds-Averaged Navier-Stokes equations with the finite-volume approach on a structured non-orthogonal grid. The SIMPLE method couples the pressure to the velocity field and the standard k-ε turbulence closure approximates the Reynolds Stresses. Simulations were performed for the laboratory-scale multi-chamber ozone contactor the flow characteristics of which were extensively evaluated by Kim et al. (2008). The twelve chamber model reactor was simplified to a four chamber reactor with the same chamber dimension.

The numerical layout of the model contactor is shown in Figure 5.1 with applied boundary conditions. Successively fine grid consisting of 1,396,050 total grid points (195 X 88 X 82 in *x*-*y*-*z* direction) is presented herein. A no-slip boundary condition is used at wall boundaries. A symmetry boundary condition is applied at the water surface since shear forces are negligible at fluid-air interfaces. Periodic boundary conditions are used in the stream-wise direction to simulate a geometrically periodic and infinitely long domain. This boundary condition prevents unwanted effects of artificial inflow and outflow boundary conditions. The Reynolds number based on the hydraulic diameter of the inlet sluice gate is 2,740 corresponding to the experiments (Kim et al. 2008).

Transport of a conservative tracer was simulated by solving the three-dimensional advection-diffusion equation. The tracer at constant concentration was introduced at the inlet of the reactor initially for 500 time steps (i.e. for the duration of approximately 2.35 s) to represent a pulse injection. The residence time distribution (RTD) was normalized by the total introduced tracer concentration such that the area under the curve was equal to unity. The time scale was normalized based on the theoretical residence time (τ) per chamber which was 27.3 for the model contactor.

5.3 Flow Characteristics

Figure 5.2 shows the distribution of normalized instantaneous, *U/U(bulk)*, and time-averaged absolute velocity, *Um/U(bulk)*, and streamlines. Areas of higher velocity (white contours) are found along the outer regions of the meandering flow path, clearly suggesting the occurrence of short-circuiting through each chamber. Although the instantaneous velocity distribution overall resembles the time-averaged velocity distribution, prevalence of turbulence, in particular, smaller vortices along the shear layers between the main flow path and the recirculation region are observed. As the flow exits each chamber near the bottom or near the free-surface, it accelerates to twice the inlet bulk velocity, *U(bulk)*, due to the presence of the sharp crest of the baffles. The distributions of time-averaged velocity contours of LES are very similar to those predicted by RANS demonstrating that the turbulence closure model captures the effect of large-scale turbulence reasonably well. The streamlines indicate that a large recirculation zone occupies approximately two thirds of the baffle spacing in the

chambers. A small counter-rotating secondary recirculation zone occurs at the corners of bottom and the baffle wall on both sides of the baffle. A third cell is observed at the downstream side and near the free end of the baffle.

The profile of normalized instantaneous, *v/U(bulk),* and time- span-wise -averaged, *vm/U(bulk)*, velocity in *y* direction at three different vertical locations in the chamber are presented in Figure 5.3. The instantaneous velocity obviously deviates from the mean value and, for the moment depicted in this figure, the instantaneous velocity maxima are above the mean values (the maxima of instantaneous velocities are about 5 times higher than the plug flow velocity). The deviation is due to the presence of severe short-circuiting (i.e. at $x/W > 0.4$-0.5) and recirculation (i.e. at $x/W < 0.4$-0.5). The maxima of RANS are quite similar to those of the instantaneous LES, whereas 15 ~ 30% less in the time-averaged LES.

The distribution of the turbulent kinetic energy in the center plane for each simulation presented in Figure 5.4 indicates relatively high turbulence intensity in areas where the flow short-circuits. Although both simulations computed similar distribution of the time-averaged velocity field, LES predicted higher energy at the corners and at the free end of baffles while higher values are observed near the wall and the water surface at the gate in RANS.

Streamlines along the *y-z* planes at three different stream-wise locations within the first chamber shown in Figure 5.5 suggest that the flow field is highly three-dimensional. At $x/W = 0.25$, two small counter-circulating vortices near the side walls and a general downward movement (i.e. as a result of the main recirculation zone) are

observed. There is a nodal point at $z/L = 0.5$ and $y/H = 0.42$ at which streamlines diverge. This nodal point corresponds to the center of the main stream-wise recirculation zone. Along the upper side of the baffle opening (i.e. $y/H \approx 0.1$), the streamlines from the recirculation zone and those from incoming fluid converge. At half the baffle spacing (i.e. $x/W = 0.5$), a pair of large, symmetric, and counter-rotating vortices are observed again suggesting three-dimensionality and fluid entrainment. At $x/W = 0.75$, upward motion is found over the entire baffle spacing.

5.4 Tracer Transport

Figure 5.6 presents snapshots of the distribution of instantaneous normalized tracer concentration as predicted by the LES (a) and the RANS (b), and as observed in the laboratory (c) (Kim et al. 2008). It has to be noted that, although the amount of tracer introduced into the reactor is less in the simulations, which explains the discrepancy between experiment and computations (especially in the first chamber), there is a fairly good qualitative agreement between the observed and the predicted concentration distributions in the second to fourth chambers. Higher concentration (brighter contour) is found near the baffles and the free surface, whereas lower concentration (darker contour) in the centre. The concentration distributions support the occurrence of the short-circuiting and a large recirculation region in each chamber. While the concentration of LES quite nicely resembles the measured distribution, almost all tracer transport as short-circuit and relatively very small amount of tracer trapped in the recirculation area flows intermittently in RANS.

5.5 Residence Time Distribution (RTD)

Figure 5.7 presents RTDs determined by Kim et al. (2008) experimentally and those simulated by the LES and the RANS. The reactor used in the experiment consists of 12 chambers with baffle spacing equal to that of the present reactor. Since the periodic boundary condition used in the present simulation does not accurately represent the inlet flow condition of the laboratory experiments, the RTDs for the first chamber do not agree well. However, magnitude and shape of the LES computed RTD curves match the observations very well from the second chamber. In particular, the presence of a sharp short-circuiting peak and a secondary peak that result from internal recirculation are noticeable in both experimental RTDs and LES RTDs. The RTD curves based on the RANS show much more severe short circuiting and exhibit pronounced secondary peaks. The unsteadiness and intermittency of the flow is not expressed in the curves from the RANS, and hence the predicted results deviate largely from the ones measured or computed by LES.

5.6 Conclusions

LES and comparative RANS results suggest the occurrence of deficient flow conditions and non-ideal solute transport behaviors. Specifically, the flow through these reactors is characterized by the presence of extensive short-circuiting from one chamber to the next through a relatively narrow baffle gap, large internal recirculation that

contributes to back-mixing and a dead zone in the center of each chamber. These observations are consistent with the experimental findings by Kim et al. (2008) made on a scale reactor with the same dimensions and flow rate as used in this study. The LES results also suggest that the flow is highly three dimensional with a pair of symmetric counter-rotating secondary vortices and nodal points in the centre of the recirculation zones. Residence time distributions evaluated that the tracer transportation should be based on the flow field in which the unsteadiness and turbulent intensity are adequately reflected. Hence, this study provides that LES can be a useful tool for new design or retrofitting existing reactors.

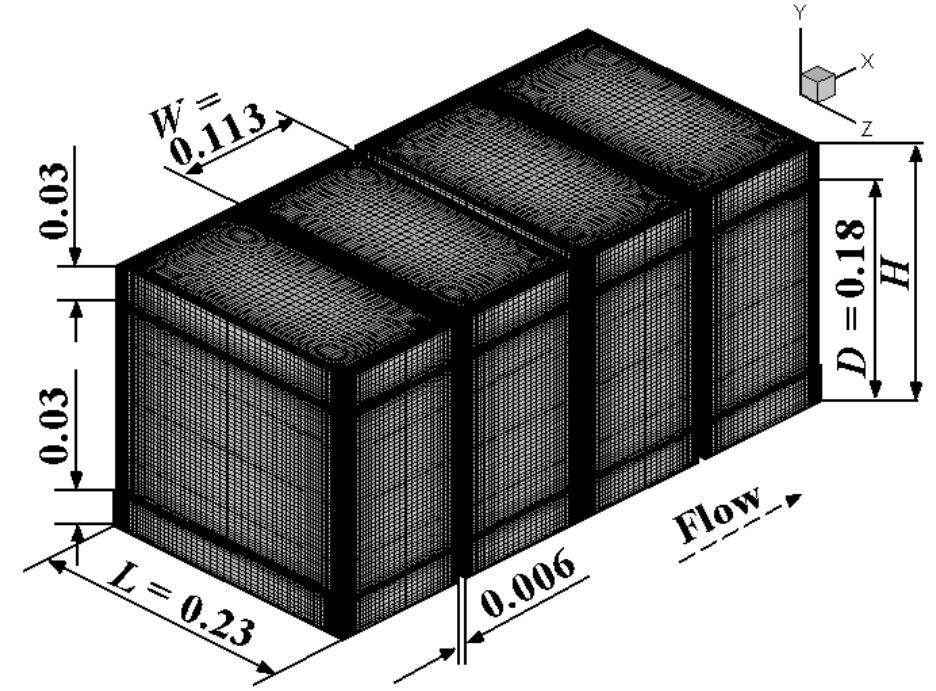

(a)

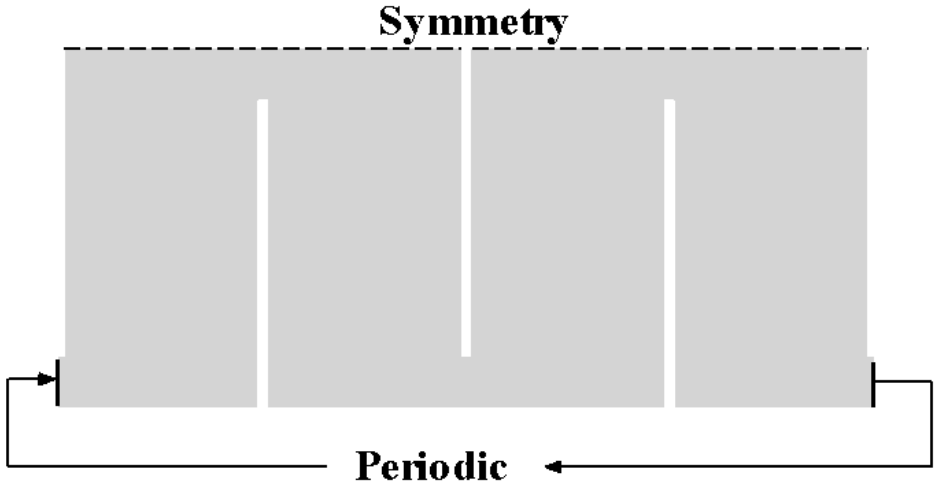

(b)

Figure 5.1. (a) Numerical model and (b) boundary conditions

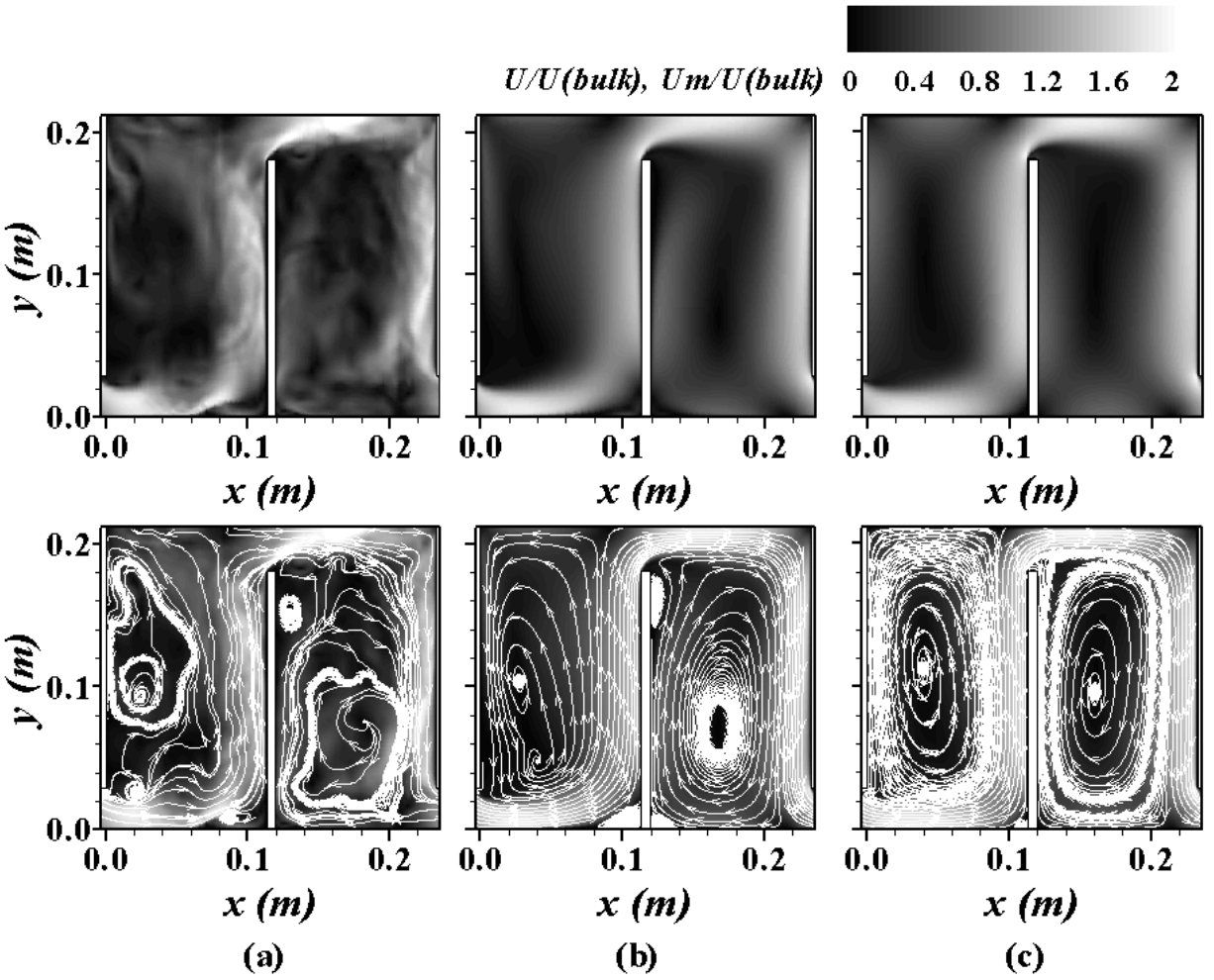

Figure 5.2. Distribution of normalized velocities and streamlines (a) LES (ins) (b) LES (mean) (c) RANS in the center plane (z/L = 0.5)

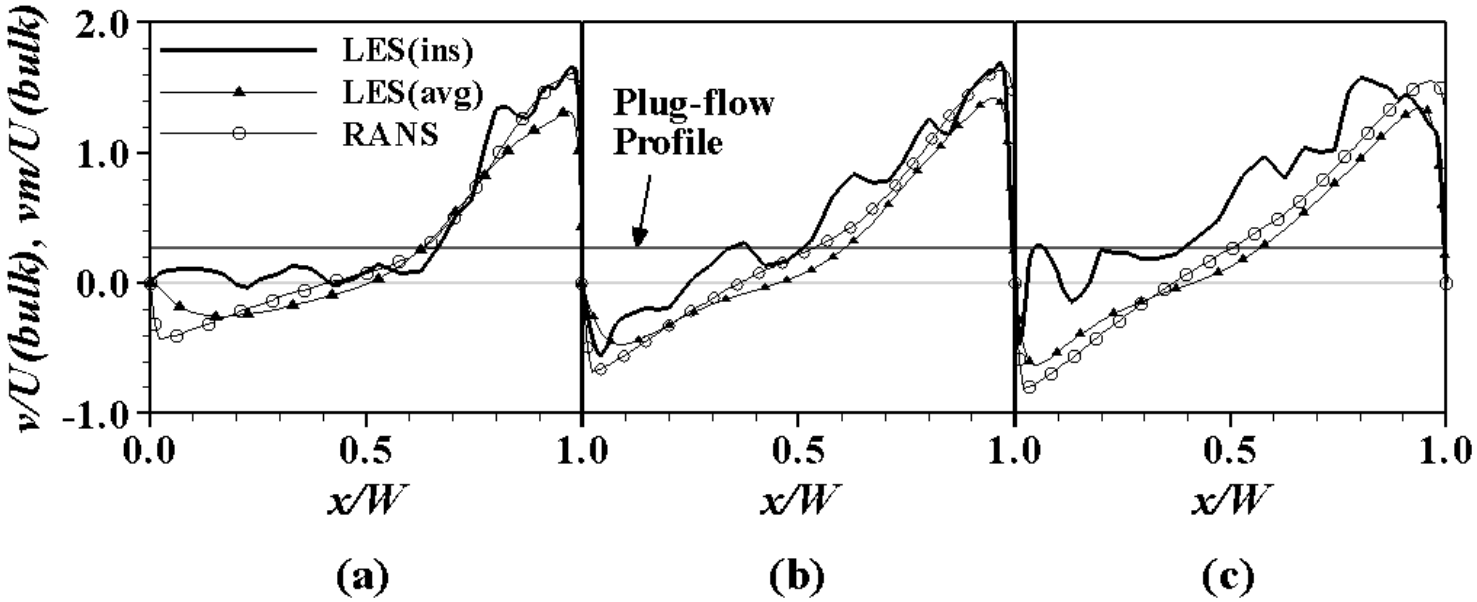

Figure 5.3. Spanwise averaged vertical velocity profiles (a) $y/H = 0.27$ (b) $y/H = 0.5$ (c) $y/H = 0.72$

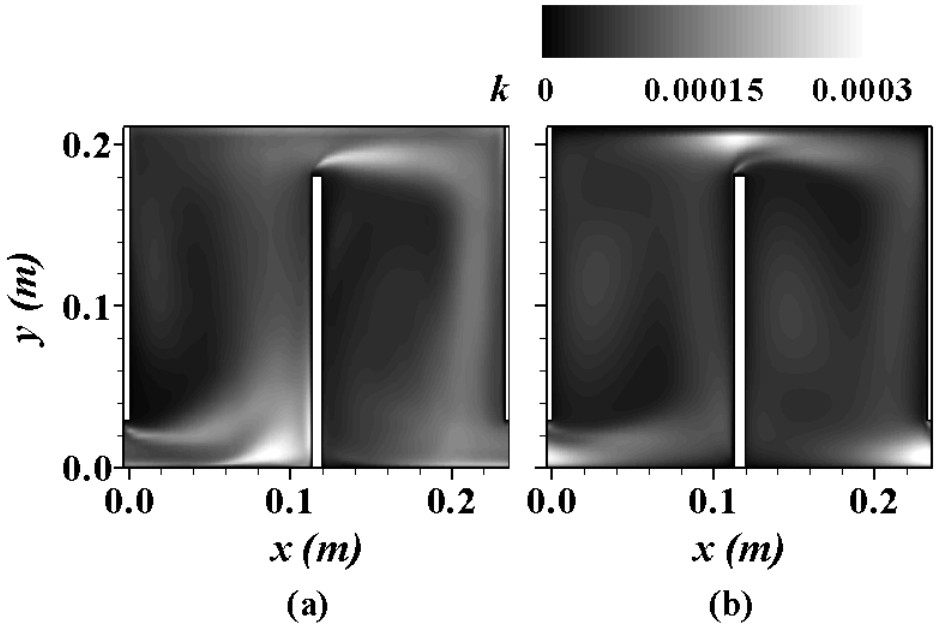

Figure 5.4. Turbulent kinetic energy (a) LES and (b) RANS

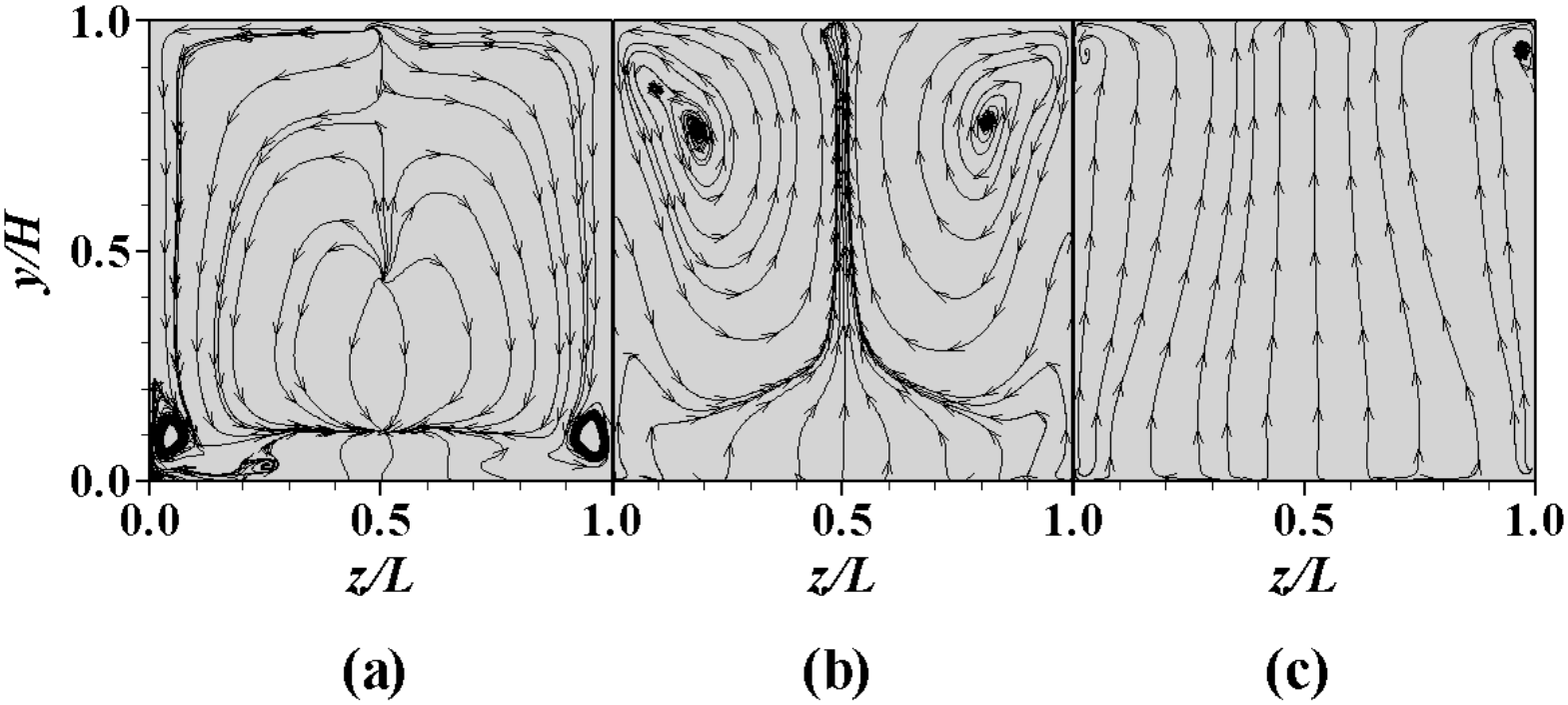

Figure 5.5. Time averaged streamlines in the spanwise planes (a) $x/W = 0.25$ (b) $x/W = 0.5$ (c) $x/W = 0.75$

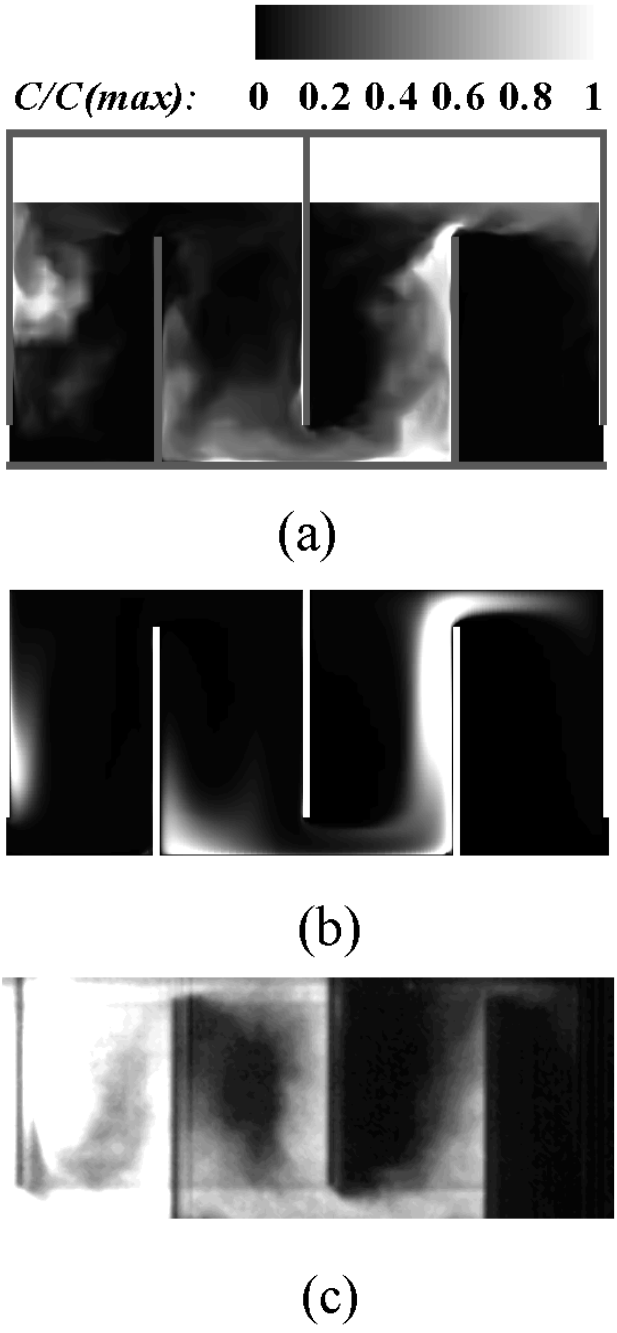

Figure 5.6. Computed (a) LES and (b) RANS, and (c) measured tracer distribution at an instant of time

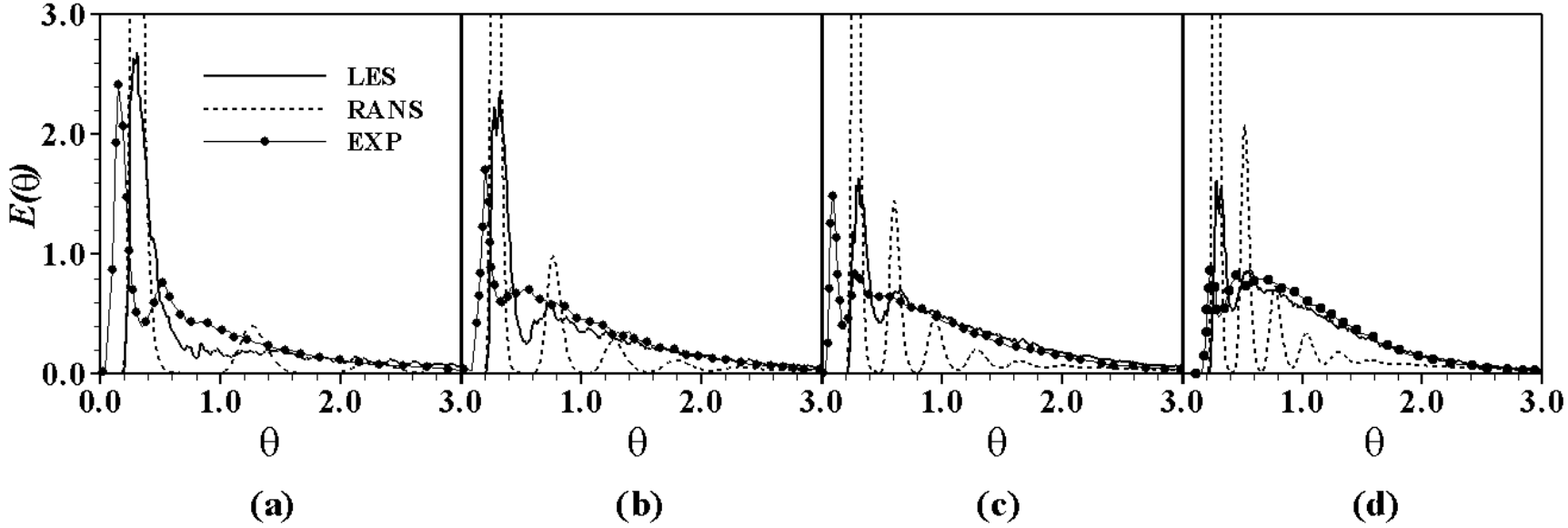

Figure 5.7. Tracer RTD curves at the exit gate of (a) chamber 1, (b) chamber 2, (c) chamber 3, and (d) chamber 4

CHAPTER 6

INVESTIGATION OF BAFFLE SPACING EFFECT ON HYDRODYNAMICS AND SOLUTE TRANSPORT IN AN OZONE CONTACTOR USING LARGE EDDY SIMULATIONS

6.1 Introduction

Ozone contactors used for water treatment are commonly designed to consist of multiple chambers in series divided by baffles resulting in a vertically meandering flow. For most disinfection reactors, a plug-flow is the target condition. However, non-ideal flow conditions of short-circuiting and recirculation exist in most multi-chamber contactors. Thus, limited disinfection and unwanted by-products, such as bromate, are incurred.

The significant importance of hydrodynamics on the process efficiency in an ozone contactor has been experimentally investigated and quantified (Kim et al., 2004; Tang et al., 2005; Kim et al., 2007). The disinfection capacity is evaluated by the residence time distribution (RTD), especially T_{10}, which is the residence time at 10% of cumulative RTD. Using this parameter, there have been efforts to improve disinfection efficacy by geometrical design modifications (Henry and Freeman, 1995; Wols et al., 2008). In particular, the baffle spacing (i.e., the distance between consecutive baffle walls) was identified as one of the critical design factors that determine the extent of short-circuiting and recirculation (Gualtieri, 2007; Zhang et al., 2007). In a recent three-

dimensional laser induced fluorescence (3DLIF) study by Kim et al. (2010a), the same level of inactivation was achieved through a narrower baffle spacing, which reduced the entire reactor volume by about 25%.

Besides experiments computational fluid dynamics (CFD) models have been applied to study and optimize the flow in multi chamber reactors (Henry and Freeman, 1995; Gualtieri, 2007; Zhang et al., 2007; Wols et al., 2008). The simulation models in above mentioned studies have been based exclusively on solving the Reynolds Averaged Navier-Stokes (RANS) equations, in which only the time-averaged velocity field is computed and all the unsteady effects of turbulence are accounted for by a turbulence model. However, the flow in meandering ozone contact chambers is characterized by unsteady flow structures, and thus the accurate prediction of the unsteady transport of solutes using RANS-based models can be a significant challenge without a-prior knowledge of the turbulent diffusivity. Kim et al. (2010b) calculated tracer transport in a multi-chamber ozone contactor using both a RANS-based CFD code and a large-eddy simulation (LES) and compared the resulting residence time distribution (RTD). They reported that the RTD obtained from the RANS model (without calibrating the turbulent diffusivity) severely overestimated short-circuiting and internal recirculation, while the LES reproduced qualitatively the experimentally obtained RTD curves.

The objectives of this study are to investigate the effect of baffle spacing of an ozone contactor on 1) the instantaneous and time-averaged flow, 2) turbulence statistics, and 3) tracer transport and its residence time distribution. Furthermore, this study aims at verifying the accuracy of the LES technique by choosing a numerical simulation setup in analogy to the physical experiments of Kim et al. (2010a).

6.2 Numerical Framework

6.2.1 Simulation Code

The LES code (Hydro3D-GT) employed in this study is based on the finite volume method and solves the filtered Navier-Stokes equations on a Cartesian grid with collocated variable arrangement (Stoesser and Nikora, 2008). The term that appears after the filtering of the governing equations, the anisotropic part of the subgrid-scale (SGS) stresses, is closed with the dynamic version (Germano et al., 1991) of the Smagorinsky model (Smagorinsky, 1963). The convection and diffusion terms in the filtered momentum equations are approximated by central differences ensuring second-order accuracy in space, and an explicit Runge-Kutta scheme is used and provides second-order accuracy in time. The code uses an adjustable time step that satisfies the C-F-L (Courant et al., 1928) stability criterion in every computational cell in order to maintain stability of the explicit time discretization scheme. The conservative tracer transport was simulated in this study by solving the following three-dimensional advection-diffusion equation for the filtered tracer concentration, $\overline{c}$:

$$\frac{\partial \overline{c}}{\partial t} + \overline{u}_j \frac{\partial \overline{c}}{\partial x_j} = (D + D_t) \frac{\partial^2 \overline{c}}{\partial x_j^2} \qquad \textbf{(6.1)}$$

where D is the molecular diffusivity and D_t is the turbulent eddy diffusivity. D is the ratio of molecular viscosity to the molecular Schmidt number (Sc) and Sc was set to be 1000 corresponding to the property of the tracer, Rhodamine-6G, used in the experiments by Kim et al. (2010a). D_t is calculated as the ratio of the turbulent subgrid-scale viscosity

$\nu_{t,sgs}$ to the turbulent Schmidt number (Sc_t). Sc_t was set to be 0.3, a standard value suggested by Jimenez et al. (2001).

6.2.2 Simulation and Boundary Conditions Setup

Figure 6.1 shows the schematic of the contactor including boundary conditions. The contactor consists of two upstream chambers for flow development, a main chamber the baffle spacing of which is changed by a movable baffle, a downstream chamber, and an extra chamber between main and downstream chambers. The baffle spacings of influent and effluent chambers are of equal width, W, which is chosen as length-scale to non-dimensionalize the geometry of the main chamber. The variable baffle spacing (Wi) varies between Wi=0.5W and Wi=5W, and the simulations are labeled as 0.5W, 1W, ... 5W. No slip boundary conditions are used at all walls, i.e. contactor bed, contactor sides (which are not shown in Figure 6.1 for the sake of clarity), and the baffles. The free surface is treated as a rigid, frictionless lid with zero shear stress. A uniform velocity profile corresponding to the experimental flow rate is prescribed at the influent surface as a Dirichlet boundary condition (designated constant value). At the effluent surface a von Neuman boundary condition (zero gradient) is used and overall mass conservation is enforced at the outlet.

The Reynolds number based on the hydraulic diameter (four times the cross-sectional area divided by the wetted perimeter) of the influent surface area is Re=784. Once the flow reaches a fully developed state a passive tracer is injected at constant concentration through seven ports at the bed underneath the upstream baffle of the main

chamber. The tracer was injected over approximately 1sec and with a ten times faster velocity than the influent bulk velocity. The tracer location, the seven inlet ports and the tracer inflow velocity are chosen to match as closely as possible the conditions of the experiment (Kim et al. 2010a).

The total number of computational grid points is approximately 6 million and consists of 330 × 51 × 242 cells in the *x, y,* and *z* direction, respectively. The numerical grid of the 3W case is depicted in Figure 6.2. The dimensionless time step, which is the computational time step normalized by the theoretical hydraulic residence time (t_{HRT}) of the LES is of the order of 2×10^{-5}. For the longest simulations, i.e. the 5W case, the simulation took 300,000 timesteps (or approximately $6t_{HRT}$) to obtain a fully developed flow field. After the flow is fully developed the simulations is continued for another 30,000 timesteps for the narrowest baffle spacing and 200,000 timesteps for the widest baffle spacing in order to obtain full RTD curves. The computations were carried out employing 78 processors on a Cray XT4 system.

6.3 Results and Discussion

6.3.1 Flow and turbulence characteristics

Figure 6.3 presents (a) streamlines of the flow, and (b) the distribution of the time-averaged absolute velocity (i.e. $V(abs) = \sqrt{u^2 + w^2}$) in the main chamber of each case. The absolute velocity, *V(abs)*, in the chamber is normalized with the inlet bulk velocity, *w(in)* . The streamline plots (Figure 6.3a) demonstrate the existence of recirculation zones in the main chamber, the size of which is very small in the 0.5W and

1W cases, however the recirculation grows continually as the baffle spacing increases. The recirculation is a result of flow separation at the baffle edge, and while the flow reattaches at the baffle wall in the 0.5W and 1W cases, it does not once the wider baffle spacing is increased further i.e. 2W –5W cases. In the wider chambers a large recirculation zone occupies the entire height of the chamber. Except for the narrow 0.5W case, a short-circuiting path (to be identified as an area with high absolute velocity, i.e., brighter contours) is observed near the right baffle (Figure 6.3b. The average width of the short-circuiting path, denoted as '*We*' in Figure 6.3a, appears to be constant and approximately equals the entrance height, *W*.

The effect of baffle spacing on the flow is further quantified by analyzing the lateral profiles of the vertical velocity at half depth of the main chamber (see sketch in upper left corner of Figure 6.4b). Figure 6.4 presents the time-averaged velocity profile normalized by (a) the inlet bulk velocity of the contactor, $\langle w \rangle / w(in)$, and (b) the bulk velocity according to the baffle spacing, $\langle w \rangle / w(bulk)$. For the sake of clarity only the cases 0.5W, 1W, 3W, and 5W are plotted. The distance between left and right wall is normalized by the corresponding baffle spacing (i.e., x/W_i). No reverse flow is observable in the 0.5W and 1W cases, while the profiles of all other cases exhibit a similar shape, i.e. high velocities near the right baffle and negative velocities near the left baffle. In the cases shown, the flow reverses at $x/W_i \approx 0.35$. The 0.5W case features a symmetric and parabolic profile, whereas all other profiles are skewed towards the right baffle wall; the larger the baffle spacing the more the profiles are skewed. Figure 6.4a, in which the velocity is normalized by a constant value, i.e. $w(in)$, shows that the peak in the velocity profile is at approximately $\langle w \rangle / w(in) = 1.45$ between the 1W and 3W cases, and it only

slightly reduces to $<w>/w(in)$ = 1.15 in the 5W case. The extent of short-circuiting and internal recirculation is more obvious once the velocity profile is normalized with the chamber bulk velocity, i.e. $w(bulk)=Q/A_{chamber}$. This is presented in Figure 6.4b. For the larger baffle spacings, the velocity peaks in the short-circuiting path attain values of five and six times the chamber bulk velocity for the 3W and 5W case, respectively. Negative velocities near the left chamber baffle of four times the bulk velocity are observed for the 5W case.

The instantaneous absolute velocity contours, presented in Figure 6.5a, embody the turbulence and the unsteadiness of the flow. The main recirculation zones can be discerned, however the flow is also characterized by smaller turbulent eddies, which are major contributors to turbulent mixing in the chamber. At the instant depicted here, instantaneous velocity magnitudes that are clearly above two times the inlet velocity are found at some locations (e.g. near the baffle in the 3W and 4W cases). As a result, areas of considerable shear exist, further enhancing turbulent mixing in the main chamber. In Figure 6.5b the distribution of instantaneous spanwise vorticity (ω_y) (at the same instant in time as the velocity contours of Figure 6.5a is plotted. Strong vortices are observable in all cases. These vortices are shed from the baffle edge and form a vortex street all featuring the same sense of rotation (hence differing somewhat from a classical von Karman vortex street behind a cylinder) along the short-circuiting path and in the larger baffle spacing cases some vortices are even traveling back along the left baffle. In the wider chambers (3W-5W) the vortices shed from the baffle grow in size until they reach the opposite baffle and weaken as they travel towards the exit. In the narrower chambers

(0.5W and 1W) vortices are found over the entire width due to the absence of a recirculation zone, the size of the vortices is limited to the baffle spacing.

The above discussed features of turbulence and unsteadiness is reflected in the turbulence statistics. Figure 6.6 presents the distribution of turbulent kinetic energy (k) in the center plane of the main chamber for the six cases investigated. The values are normalized by the square of the inlet bulk velocity, $w(in)^2$ in order to quantify and directly compare the turbulence for each case. Areas of high turbulent energy principally coincide with areas of high velocity and vorticity, being prevalent in the short-circuiting path. The highest values of kinetic energy are found near the entrance of the main chamber, where the vortices are shed from the baffles. As the flow progresses through the main chamber the peaks of kinetic energy diminish. This is owed to the fact that the growing vortices weaken and turbulence is being spread over a wider area. Obviously such a scenario depends on the baffle spacing, i.e. the wider the chamber the more the vortices can grow. For the larger chambers (3W, 4W and 5W cases) the lowest values of turbulent kinetic energy are observed in the recirculation zone, because the vortices travel around the core of the recirculation zone.

Lateral profiles of the three turbulent normal stresses and the kinetic energy in the center plane at half water depth (i.e., 0.5B and 0.5H) are presented in Figure 6.7. The upward, or streamwise, normal stress ($w'w'/w(\text{in})^2$) is the greatest contributor to the kinetic energy. In the narrowest chamber (0.5W case), higher streamwise stresses are found near the baffles, where the vortices interact with the wall and produce the highest shear. In the 1W case, however, the streamwise stresses near the left side baffle wall reduce significantly, while there are still high values near the right side baffle. The high

streamwise stresses near the right side baffle wall become smaller in the wider chambers and reduce to similar levels with those near the left side baffle wall. The streamwise stresses are much higher in the narrower chamber cases than in the wider cases due to the presence of previously shed eddies being confined in a relatively narrow space and at the same time being transported at high velocity. The normal stresses in the baffle-normal direction, i.e., $u'u'/w(\text{in})^2$, express that previously shed vortices are transported with higher velocities in the centre of the channel in the narrower chambers. In the wider chambers the maxima of the baffle-normal stresses are found near the right baffles, i.e. in the short-circuiting path, and their minima are found in the recirculation regions. The stresses in the spanwise direction, i.e., $v'v'/w(\text{in})^2$, confirm the three-dimensionality of turbulence in the flow. Interestingly their values are as high as the baffle-normal stresses ($u'u'/w(\text{in})^2$) even though the flow is quasi-two-dimensional, i.e., the time-averaged velocity <v> is zero. The spanwise stresses are considerably higher in the narrower chambers than in the wider chambers. This can be attributed to the confinement of eddies between the baffle walls, they can only expand in the spanwise direction. In the wider chambers spanwise stresses are elevated near the right baffle wall, i.e., where some vortices impinge before they are being convected towards the free surface. Overall, the magnitude of spanwise stresses is much lower in wider chambers suggesting less mixing in that direction. All the aforementioned features are clearly reflected in the turbulent kinetic energy profile, with the narrower chambers displaying a three times higher peak value than the wider chambers.

6.3.2 Solute transport

After the flow has reached a fully developed state, a constant value of conservative tracer is injected through the chamber bottom at the entrance to the main

chamber in analogy to the experiments. Figure 6.8 presents contours of the absolute velocity (upper part of the figure) and contours of tracer concentration (lower part of the figure) in the 1W chamber at a few selected instants in time during the tracer injection period. The high vertical velocity at which the tracer is injected enters the chamber as a jet and considerably alters the local instantaneous flow. Immediately after injection the jet starts to oscillate due to turbulent instabilities, sending some of the tracer into the upstream chamber. The incoming jet of water adds turbulence to the already turbulent flow and new vortices are generated during the injection period. The injection turbulence enhances the turbulent diffusion of the tracer in the early stages of its transport through the main chamber.

After the injection, the tracer cloud is advected along the main flow path and diffuses across the main chamber. Figure 6.9 illustrates how the baffle spacing affects the instantaneous tracer transport by depicting its distribution at different instants in time. As mentioned above, part of the tracer gets injected into the upstream chamber, and while some tracer is still in the upstream chamber, the rest of the tracer has already reached the middle height of the chamber (see the earliest time step). The highest concentrations of tracer is observed in the 0.5W and 1W cases (due to their size), and the tracer occupies the entire baffle spacing while being dispersed towards the exit. The transport of the tracer in the narrow chambers resembles qualitatively plug flow. However, some part of the tracer already exits the chamber, while another part is still in the upstream chamber. In both wider chambers depicted here, i.e. 3W and 5W cases, some tracer is already exiting the chamber at very early instants in time (see $t/t_{HRT} = 0.198$ in 3W case and $t/t_{HRT} = 0.166$ in 5W case) providing the proof of the previously discussed short-circuiting.

Also the virtue of both large and small scale turbulent eddies is apparent. In the wider chambers (3W and 5W cases), some of the tracer gets dispersed into the recirculation zone, particularly visible in the 3W case (i.e., at t/t_{HRT} = 0.266 in 3W case) and then being transported along the left baffle. In the 5W case some tracer exits t/t_{HRT} = 0.166, while some gets dispersed into the large recirculation zone and travels back towards the inlet. At t/t_{HRT} = 0.592 in the 3W case and t/t_{HRT} = 0.334 in 5W case, there is a patch of high tracer concentration above the entrance at the baffle in the main chamber (also seen at earlier instants), apparently being trapped in a small recirculation bubble that forms (see also time-averaged streamlines). The observations made of the instantaneous tracer transport are consistent with the previous hydrodynamic observations, i.e., turbulent eddies are responsible for the tracer transport; and short-circuiting and recirculation are less severe in the narrower chambers, whereas the tracer transport in the wider chambers suffers from the deficient hydrodynamics leading to short-circuiting and internal recirculation.

The transport characteristics of solutes in ozone contactors can be quantified with a residence time distribution (RTD) plot. The tracer is sampled and integrated over the chamber exit plane. Figure 6.10 presents the normalized CT value, $E = C * t_{HRT} / \sum Cdt$, and its cumulative value, F, as a function of normalized time scale, t/t_{HRT}, for selected cases (i.e., 0.5W, 1W, 3W, and 5W). The computed results are also compared with available experimental data (for 1W, 3W, and 5W), which should be considered a validation of the LES. The computed magnitudes and locations of the peak concentrations do not exhibit a perfect match to the measurements; however the overall agreement is very satisfying. In particular, the disinfection performance of each contactor using T_{10} is predicted very well. In terms of contactor performance, the reactor with

baffle spacing 0.5W shows a similar residence time than the 1W case, it features a smaller peak value but also a longer tail. The cumulative curves of these two cases indicate that the 0.5W case has slightly higher T_{10} value than the 1W case ($T_{10,0.5W} \approx 0.74$ and $T_{10,1W} \approx 0.71$). Higher T_{10} value (superior class if $T_{10} > 0.7$) is recommended by regulations, such as USEPA (1999), however, due to the longer residence time after the peak concentration, the 0.5W case should be considered inferior to the 1W case. This can be quantified by comparing the residence time at 90% of the cumulative concentration (i.e., T_{90}); here, $T_{90,0.5W} \approx 2.93$ and $T_{90,1W} \approx 1.8$. The comparison of computed and measured RTD curves of the 3W and 5W cases clearly demonstrate the predictive capability of LES. The simulations reproduce accurately the secondary peaks (indicated by arrows) in the tail of the curve. These secondary peaks represent the effect of internal recirculation on the RTD curve, which is the transport of tracer into the recirculation region. This is especially obvious in the 5W case in which a distinct secondary peak represents the part of the tracer that circulates the chamber once before exiting, and the tertiary peak represents the part of the tracer that circulates twice through the chamber. The cumulative curves of the 3W and 5W cases quantify the deteriorating contactor performance with an increase in baffle spacing, which is due to enhanced short-circuiting ($T_{10,3W} \approx 0.31$ and $T_{10,5W} \approx 0.23$) and long residence times. Noteworthy is that the residence time in the contactors with wide chambers is little affected ($T_{90,3W} \approx 2.65$ and $T_{90,5W} \approx 2.45$). Overall, the method of LES is able to reproduce the tracer transport characteristics in ozone contactors quite accurately, which is due to the fact that the relevant instantaneous flow dynamics, i.e., the large eddies are simulated explicitly. Hence, LES simulates directly the transport of passive tracers, being a result of advection and large-scale turbulent diffusion.

6.4 Conclusion

Several large-eddy simulations were carried out and the results confirm that the baffle spacing is a critical parameter in the design of an ozone contactor. The simulations provide first and second order statistics of the hydrodynamics in several ozone contact chambers, the baffle spacing of which varied between 0.5 times to 5 times the size of the base chamber. The width of a large recirculation grows at about the same rate as the baffle spacing increases. As a result, the width of the short-circuiting path in each chamber is increasing only little, leading to severe short-circuiting in the chamber. Instantaneous turbulent eddies that are shed from sharp baffle edges are prevalent in the chamber and increase turbulence and turbulent mixing. The turbulence statistics are characterized by the flow unsteadiness and elevated levels of turbulence are found in the short-circuiting flow path. In addition to the hydrodynamics the transport of a passive tracer was investigated. The tracer is dispersed along the short-circuiting path and into the recirculation zone due to turbulent diffusion. The simulated RTD and cumulative RTD curves compare quite well with experimentally obtained results. The base chamber, the baffle spacing of which corresponds to the chamber entrance gate height, clearly exhibits the most favorable behavior in terms of disinfection performance having a minimum amount of short circuiting and almost no internal recirculation. An increase in baffle spacing, but also a further decrease in baffle spacing, worsens the performance in terms of the residence time distribution. Overall, the method of three dimensional LES has proven to be a reliable tool for predicting ozone contactor performance without the need for calibration of model constants.

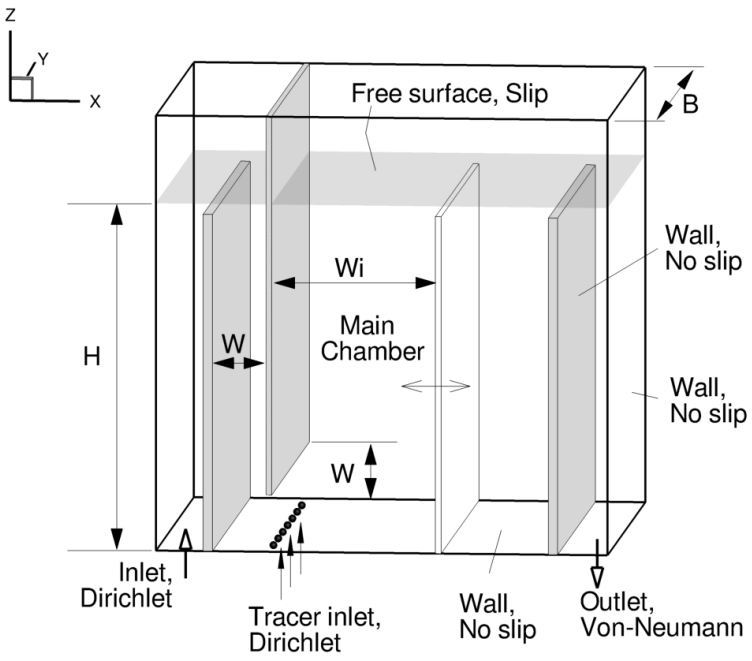

Figure 6.1. Layout and boundary conditions of the variable baffle spacing ozone contactor investigated in this study

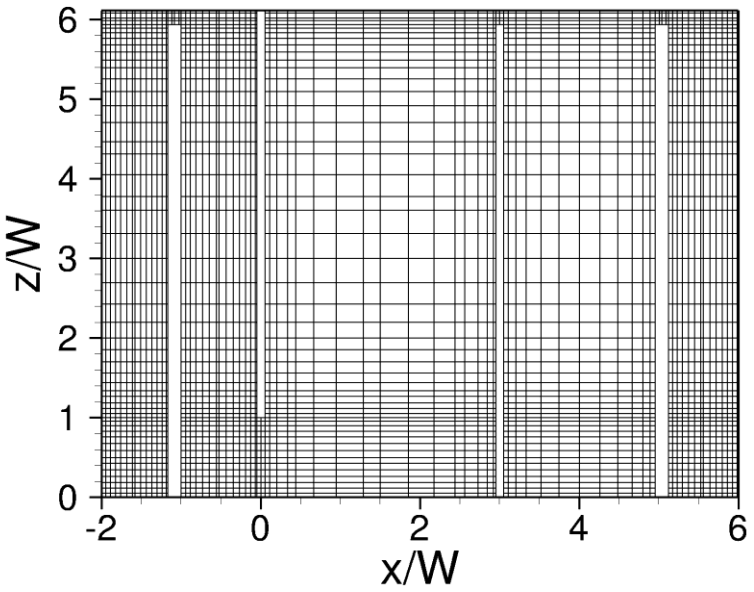

Figure 6.2. Front view of the computational grid of the 3W case (only every fifth grid line is plotted)

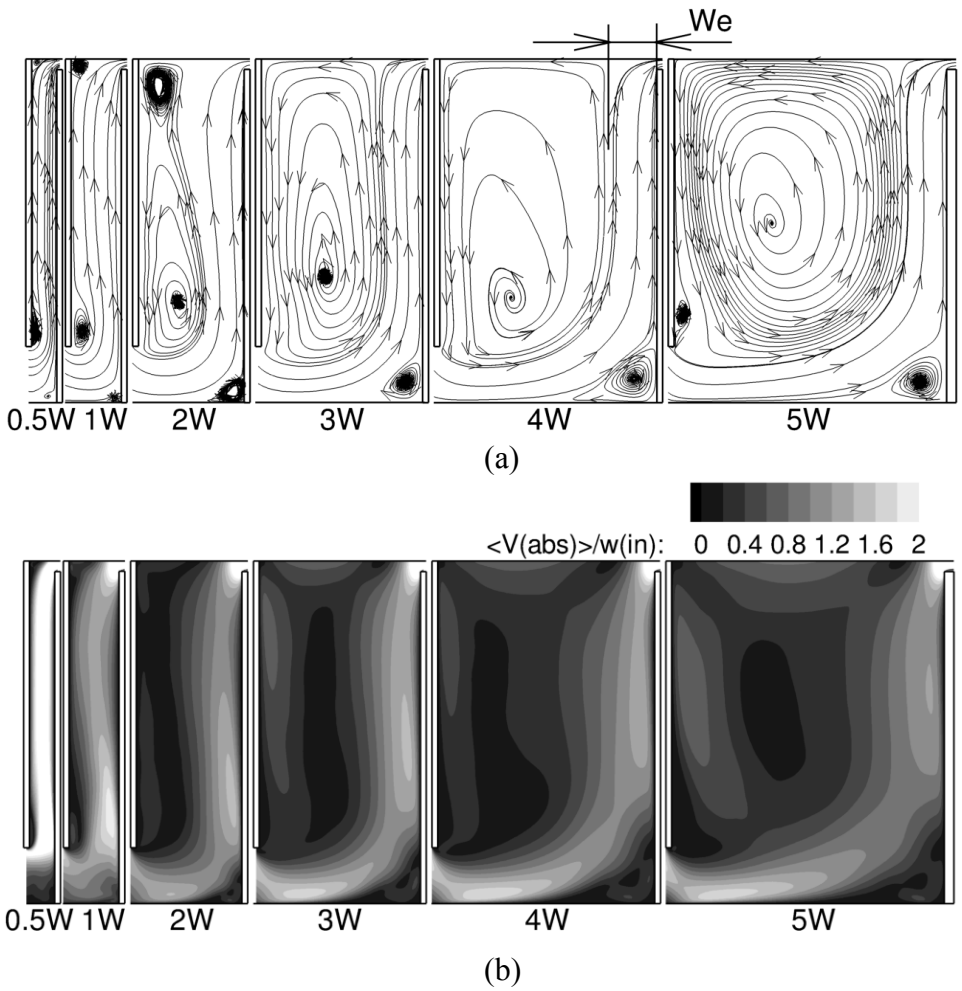

Figure 6.3. (a) Streamlines and (b) time-averaged velocity contours in the main chamber center-plane for the six cases investigated

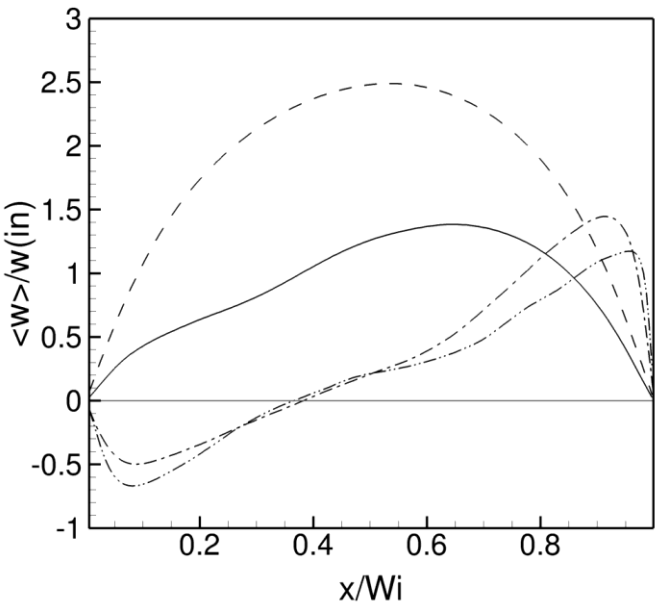

(a)

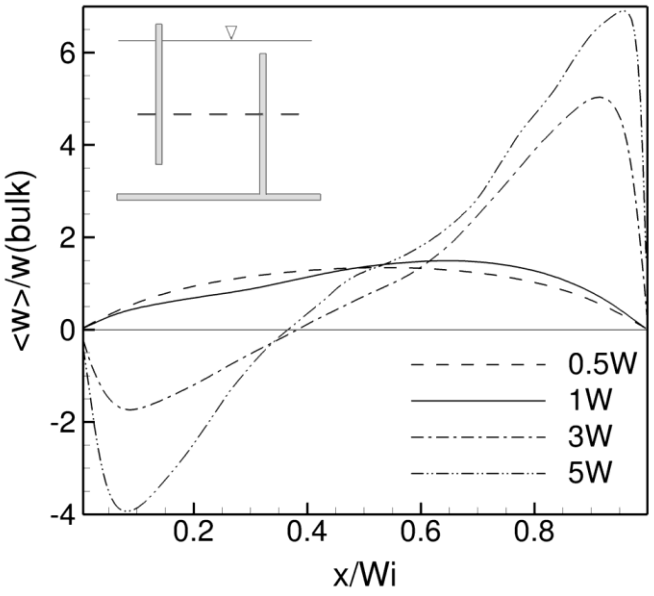

(b)

Figure 6.4. Profile of the time-averaged vertical velocity normalized by (a) the contactor inlet bulk velocity and (b) the chamber bulk velocity ($Q/A_{chamber}$) at half depth (i.e., at y=0.5B and z=0.5H)

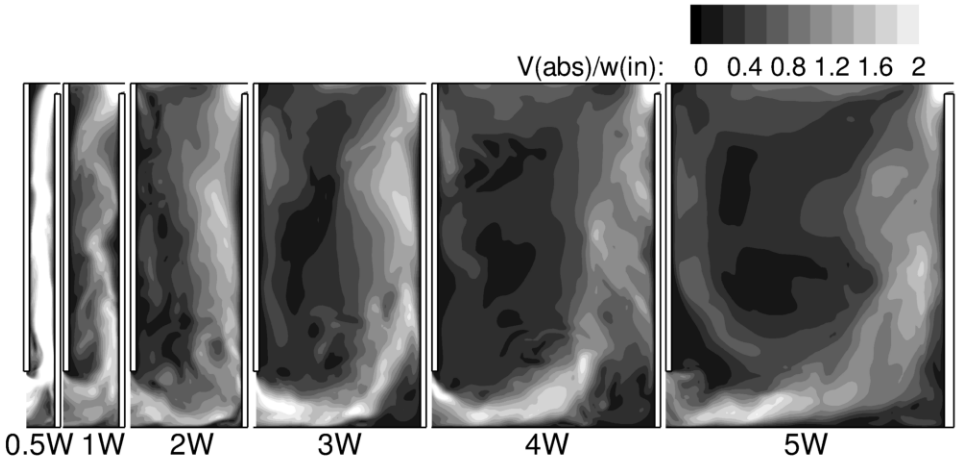

(a)

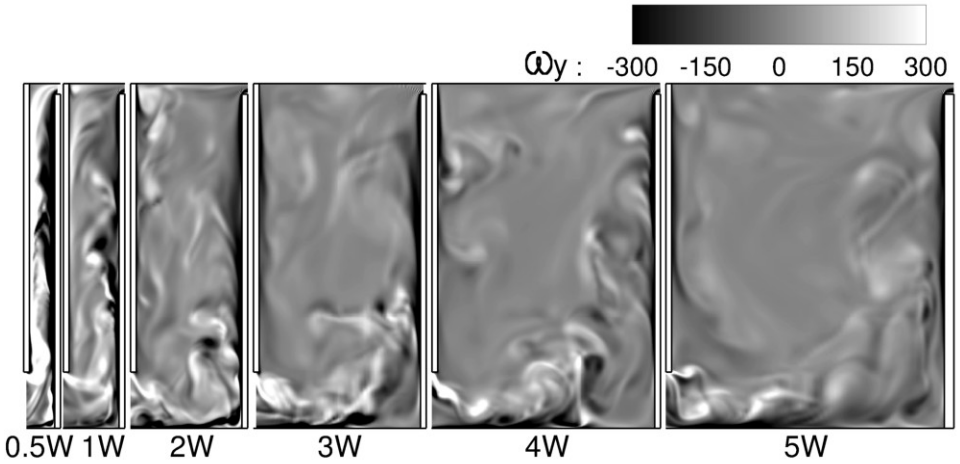

(b)

Figure 6.5. Distribution of (a) instantaneous absolute velocity and (b) spanwise vorticity in the center plane of the main chamber for six cases studied

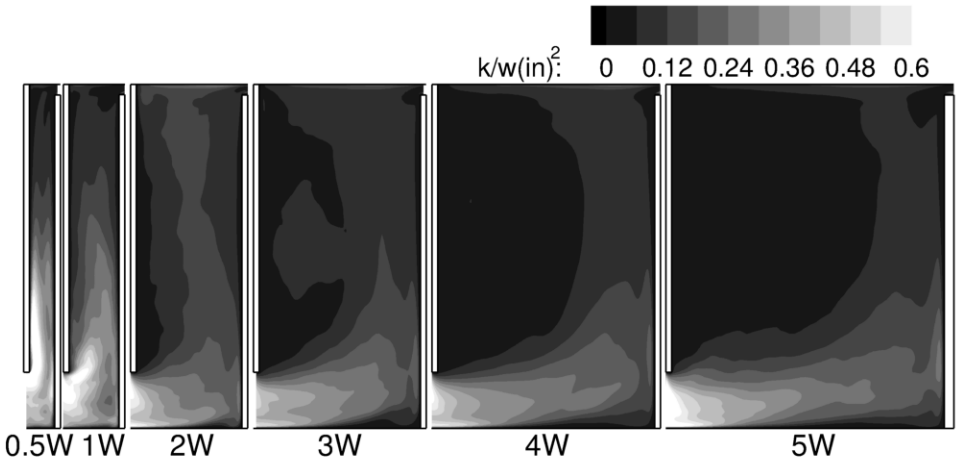

Figure 6.6. Distribution of turbulent kinetic energy in the center plane of the main chamber for all six cases studied

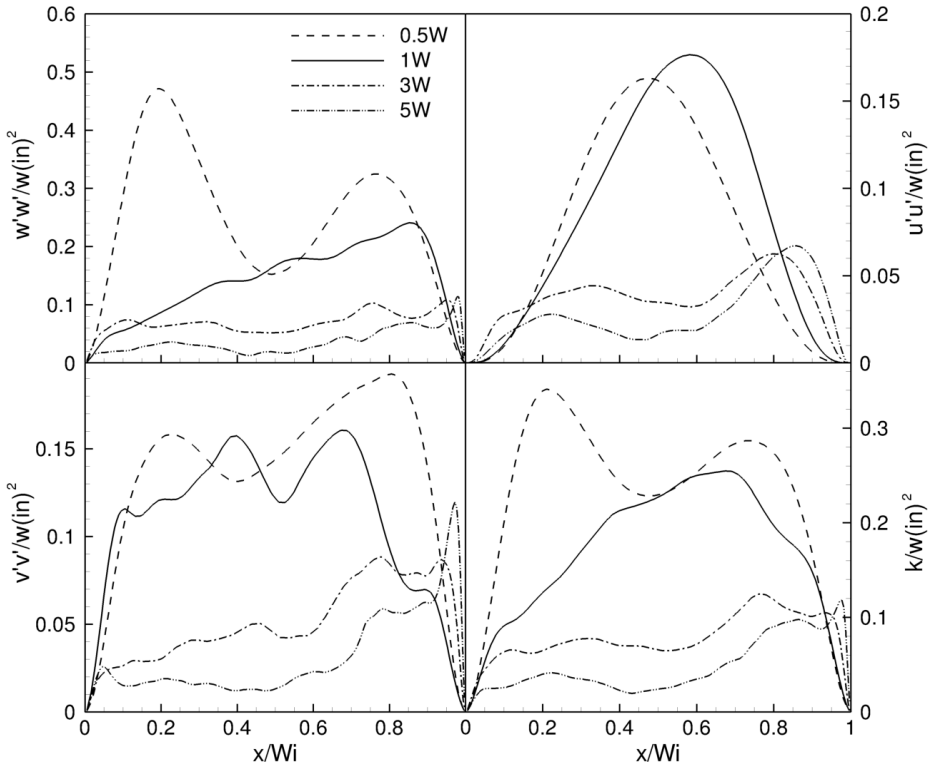

Figure 6.7. Lateral profiles of the three stress components and the kinetic energy at the half depth

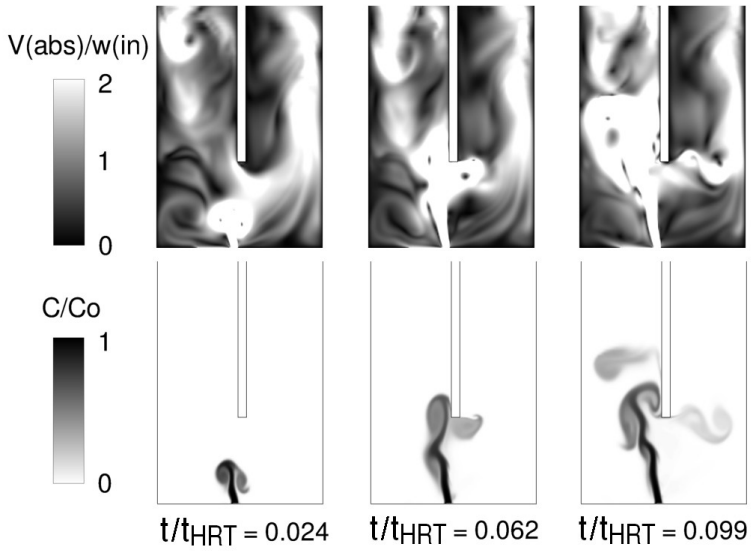

Figure 6.8. Distribution of the instantaneous absolute velocity (top) and contours of normalized tracer concentration (bottom) at selected instants during injection period in the 1W chamber

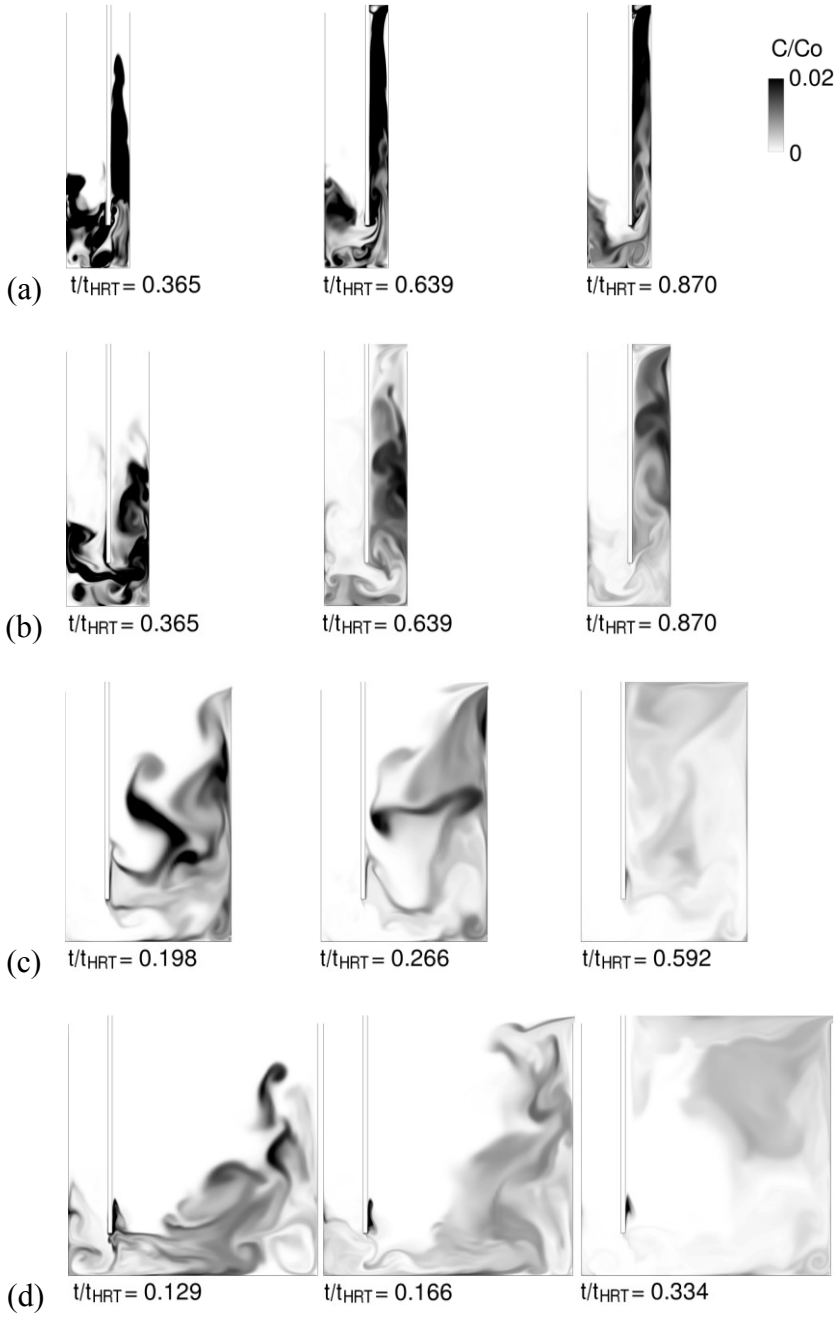

Figure 6.9. Distribution of instantaneous normalized tracer concentration at characteristic instants after tracer injection in the (a) 0.5W chamber, (b) 1W chamber, (c) 3W chamber, and (d) 5W chamber

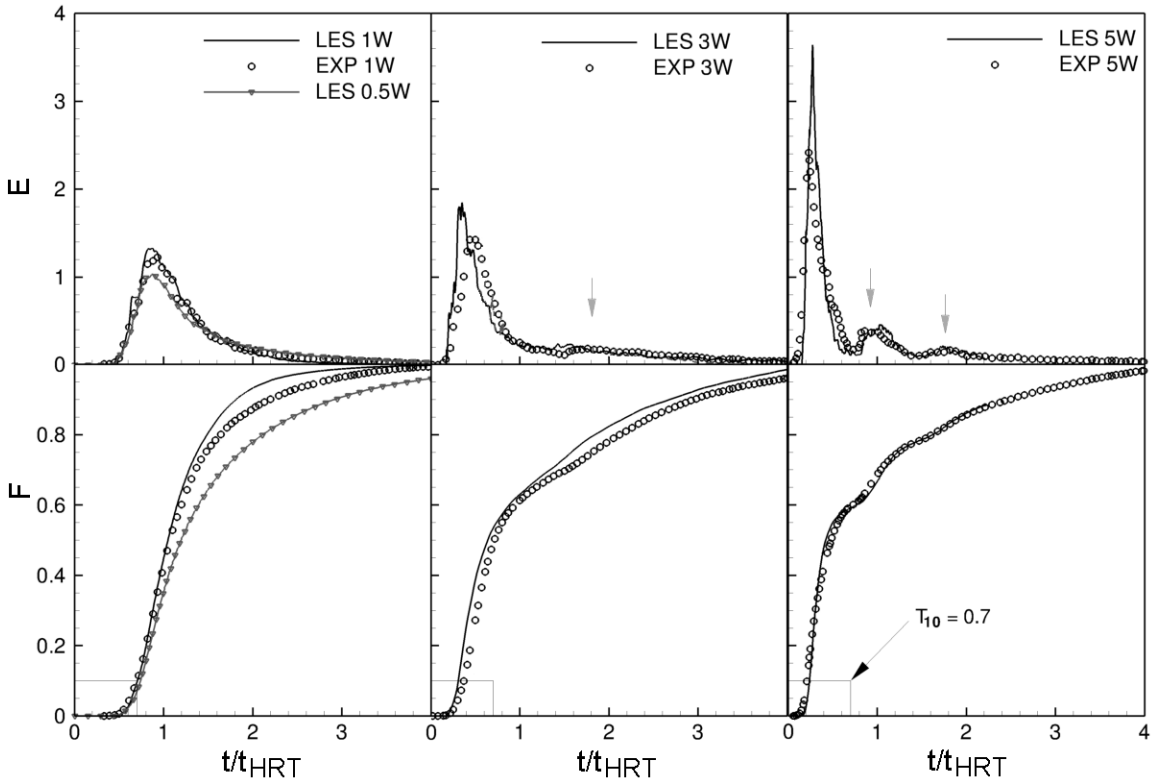

Figure 6.10. Tracer RTD curves at the exit of each chamber for the 0.5W, 1W, 3W and 5W cases

CHAPTER 7

NUMERICAL AND MODELING ASPECTS OF RANS SIMULATIONS OF FLOW AND SOLUTE TRANSPORT IN OZONE CONTACTORS

7.1 Introduction

Computational fluid dynamics (CFD) have been applied to verify the existence of internal recirculation in serpentine flow reactors replacing or reducing the both the effort and the cost of physical model experiments (e.g. Wang et al. 1998a, 1998b, Wols et al., 2008). CFD has also been employed to guide retrofitting of existing reactors by providing predictions of the expected hydrodynamics (e.g. Henry and Freeman, 1995, Murrer et al., 1995, Zhang et al., 2007).

Most of the CFD simulations of flow and solute transport in ozone contactors carried out in the past have been based on solving the Reynolds Averaged Navier-Stokes (RANS) equations, in which only the time-averaged velocity field is computed and all the unsteady effects of turbulence are accounted for by turbulence models. However, the flow in an ozone contact chamber is characterized by unsteady large-scale flow structures due to flow separation and vortex formation (Kim et al., 2009, 2010b). Hence, the accurate simulation of the effect of unsteadiness on the time-averaged flow is a significant challenge for RANS based models. Moreover, the calculation of the unsteady transport of a tracer using a RANS-based model can only be accurate if the instantaneous flow is similar to the time-averaged flow or if the effect of turbulence is accounted for through an adequate (calibrated) turbulent diffusivity.

For instance Wols et al. (2008) used a RANS based finite-element flow simulation code (Finlab) with standard *k*-ε model. In their study, the turbulent diffusivity used for tracer transport is $D_t = C_\mu(k^2/\varepsilon)$ with the constant C_μ = 0.09. This means the turbulent Schmidt number, Sc_t, they employed is 1.0. They reported underestimation of the diffusion of tracer between the recirculation zone and the main flow. Wang et al. (1998a, 1998b) used Sc_t =0.5 the value suggested by Rodi (1980) for the standard *k*-ε model, compared with a number of different turbulence models (*e.g.*, depth-averaged viscosity model, *k*-ε model, and Smagorinsky model) for flow simulation of multi-chamber chlorine contactors to find that the standard *k*-ε model predicted higher peak and longer detention time of the flow through curve than the other models. In the chapter 4 and 5, tracer transport was calculated in a multi-chamber ozone contactor using both a RANS and a LES based CFD codes and compared the resulting tracer transport characteristics. They reported that the RTD curves obtained through the RANS model (without calibrating the turbulent diffusivity) severely overestimated the peak of the RTD curve and underestimated the $t_{10} - value$, i.e. the time at which 10% of the injected tracer has exited the reactor. Tominaga and Stathopoulos (2007) studied various types of flow field (such as jet perpendicular to the main stream and flow around rectangular building) with RANS model and confirmed that the optimum values of turbulent Schmidt number are widely distributed in the range of 0.2 – 1.3 and largely depend on the local flow characteristics. He et al. (1999) also had a look at the effect of Schmidt number on turbulent scalar mixing in a jet in cross flow recommending that the turbulent Schmidt number to be 0.2 for best agreement with measurements. In contrast, large eddy simulation (LES) of turbulent channel flow by Dong et al. (2003) suggested that, from the study of very wide range of turbulent Schmidt number from 0.1 up to 200, 1.0 was the optimum value.

The objectives of this study are to investigate and quantify numerical and modeling aspects of RANS based simulations of flow and transport in different ozone contact reactors. The quantities to be investigated are the turbulent Schmidt number, spatial resolution and the time step size. The RANS simulations are compared with validated, high-resolution Large-Eddy Simulations, with which numerical modeling errors of RANS can be quantified.

7.2 Numerical Framework

7.2.1 Simulation Code

The model SSIIM (Olsen, 2005) was employed to perform the RANS simulations of the hydrodynamics of the ozone contact reactors. SSIIM solves the Reynolds-Averaged Navier-Stokes equations with the finite-volume approach on a structured non-orthogonal grid. The SIMPLE method couples the pressure to the velocity field and the standard k-ε turbulence closure approximates the Reynolds Stresses. The model has been used for a wide range of flows and applications and has been thoroughly validated (e.g. Fischer-Antze et al., 2001, Wilson et al., 2003, Ruether and Olsen, 2005, Stoesser et al., 2009).

While SSIIM provides the hydrodynamics the conservative tracer transport was simulated in this study by solving the advection-diffusion equation for the tracer concentration, C:

$$\frac{\partial C}{\partial t} + \overline{u}_j \frac{\partial C}{\partial x_j} = D_t \frac{\partial^2 C}{\partial x_j^2} \qquad \textbf{(7.1)}$$

where $\overline{u}_j$ is the Reynolds averaged velocity vector and ν_T the eddy viscosity, both taken from the SSIIM results. D_t is the turbulent eddy diffusivity, which is the ratio of the eddy

viscosity, to the turbulent Schmidt number (Sc_t). Initially, Sc_t was set to be 0.7, which is a commonly accepted value for RANS based simulations, however as part of this study Sc_t was calibrated to match the LES results. The Hybrid Liner/Parabolic Approximation (HLPA), which is low diffusive and oscillation-free scheme suggested by Zhu (1991), is used for the convective terms in the tracer transport equation and second order three-time-level implicit scheme is employed to integrate the equation in time.

The comparative LES simulations are reported in Kim et al. (2011) and are based on the in-house code HYDRO3D-GT (Stoesser and Nikora, 2008, Kim et al. 2010), which, for the sake of brevity, is not explicitly introduced here.

7.2.2 Simulation and Boundary Conditions Setup

Figure 7.1 shows the schematic of the contactor including boundary conditions. The contactor consists of two upstream chambers for flow development, a main chamber the baffle spacing of which is changed by a movable baffle, a downstream chamber, and an extra chamber between main and downstream chambers. The baffle spacing of influent and effluent chambers are of equal width, W, which is chosen as length-scale to non-dimensionalize the geometry of the main chamber. The baffle spacing (Wi) varies between $Wi=W$ and $Wi=W\times5$, and the simulations are labeled as 1W, ... 5W.

No slip boundary conditions are used at all walls, i.e. contactor bed, contactor sides (which are not shown in Figure 7.1 for the sake of clarity), and the baffles. For RANS, wall law suggested by Schlichting (1979) was used. The free surface is treated as a rigid, frictionless lid with zero shear stress. A uniform velocity profile corresponding to the experimental flow rate is prescribed at the influent surface is used and overall mass conservation is enforced at the outlet.

The boundary conditions for the tracer transport equation are as follows: Dirichlet boundary condition at the inlet and the walls and von Neuman boundary conditions at the outlet and the spanwise boundaries.

The Reynolds number based on the hydraulic diameter (four times the cross-sectional area divided by the wetted perimeter) of the influent surface area is Re=784. Once the flow reaches a fully developed state a passive tracer is introduced at constant concentration in a plane underneath the upstream baffle of the main chamber (the oblique lined plane) over approximately 1sec.

Since the geometry is quasi two-dimensional the RANS simulations are carried out as quasi-2D simulation, with slip-condition in the spanwise directions. The total number of computational grid points of the finest RANS grid is approximately 320,000 and consists of 330 × 4 × 242 cells in the x, y, and z direction, respectively. The numerical grid of the W3 case is depicted in Figure 7.2. Three different grid resolutions for RANS cases are used: fine grid case with the same resolution with that of LES; coarse grid case which has half grid fineness of fine grid case; and even coarser case with half grid resolution of coarse grid case. The cell sizes normalized by the entrance gate height of the main chamber, h, are 7.6×10^{-4}, 1.6×10^{-3}, and 3.6×10^{-3}, and the results are labeled as F, C, and CC, respectively. The time step is also varied to investigate its effect on the accuracy of the simulation and varies between 8×10^{-4}, 8×10^{-3}, and 4×10^{-2}.

7.3 Results and Discussion

7.3.1 Flow and turbulence characteristics

The streamlines in each main chamber predicted by LES and RANS are plotted in Figure 7.3. The flow patterns are clearly characterized by large and small scale

recirculations and a main short-circuiting path along the bed and the downstream baffle wall. The results from both LES (Figure 7.3a) and RANS (Figure 7.3b) exhibit a very similar overall behavior although small size secondary vortices in the corners are absent in the RANS simulations. The recirculation zone grows continually as the baffle spacing increases. In the wider chambers (3W and 5W) a large recirculation zone occupies the entire height of the chamber, and the width of the short-circuiting path appears to be constant and approximately equals the entrance height, *h*.

Figure 7.4 presents the absolute velocity, $V(abs) = \sqrt{u^2 + w^2}$, distributions in each main chamber of the instantaneous flow field from LES and the time-averaged field provided from RANS. This is an important and interesting comparison due to the fact that the tracer transport in RANS uses the time-averaged flow field, while in reality (and in the LES) the tracer is transported by the instantaneous flow. The absolute velocity, *V(abs)*, in the chamber is normalized with the bulk velocity of the reactor inlet, *w(in)*. The instantaneous absolute velocity contours of LES, presented in Figure 7.4a, embody the turbulence and the unsteadiness of the flow. Higher velocities are observed along the bed and the downstream baffle walls, and in the wider baffle spacing chambers, large recirculation and dead zones (almost zero velocity area inside the recirculation) are present. Besides the obvious large scale motions, the flow is also characterized by smaller local turbulent eddies, which are major contributors to turbulent mixing in the chamber. At the instants depicted here, instantaneous velocity magnitudes can reach up to twice the inlet bulk velocity at the entrance gate of the main chamber. The time-averaged absolute velocity contours of RANS in Figure 7.4b also feature a similar distribution of velocity magnitudes than the instantaneous LES results; however turbulent fluctuation and small scale motions are all absent due to time-averaging.

A quantitative comparison of time-averaged velocities to assess the accuracy of RANS is provided in Figure 7.5. Figure 7.5 presents the profiles of normal velocity component along selected lines. In the upper row (Figure 7.5a) the profiles of the time-averaged vertical velocity normalized by the bulk velocity of each chamber along the lateral lines at z/Z = 0.5 (see sketch for illustration) in each chamber are plotted. The horizontal distance is normalized by the respective baffle spacing. Three profiles from different grid resolutions (labeled as F, C, and CC) of RANS studies are compared with the one from the LES. All profiles have peaks near the downstream baffle (right side wall), and the wider chambers have negative peaks near the upstream baffle (left side wall). These peaks increase with the baffle spacing indicating the proportionality of short-circuiting strength with the baffle spacing. The velocity gradients near the walls of RANS are greater than that of LES, and the peaks of RANS are also higher than the ones in LES cases. However all RANS simulations predict the time-averaged flow reasonably well except close to the wall. The time-averaged horizontal velocity profiles at the entrance gate of the main chamber are also examined and are presented in Figure 7.5b. The magnitude of the profile is normalized with the bulk velocity at the entrance gate, and the vertical distance is normalized with the gate opening, *h*. The results are inconsistent with the observations made above. The fine (F) and coarse (CC) grid results of the RANS agree less favorably with the LES, while the medium grid (C) matches the LES profile quite well. The finest grid overpredicts the reverse flow beneath the baffle (z/h ~ 0.9), while only small negative velocities are observed in the two coarser grids of RANS and the LES. Overall, it seems there is no significant effect of the grid resolution in RANS on the hydrodynamics, and the time-averaged flow predicted by the RANS model can be considered acceptable accuracy.

Figure 7.6 presents the time averaged velocity profile from the RANS and the instantaneous velocity profiles at three arbitrary instants in time from the LES at the same

locations as in Figure 7.5. The assumption of RANS based unsteady tracer simulations is that the time-averaged flow behaves similarly to the instantaneous flow. In the W1 case at half depth the instantaneous flow is quite similar to the time-averaged profile from RANS (Figure 7.6a), however the other two cases (i.e., 3W and 5W) exhibit markedly different profiles of the instantaneous velocity than the time-averaged velocity. Similar observations can be made for the profile directly underneath the baffle. Here the instantaneous flow is different than the time-averaged flow in all three cases. At some locations the instantaneous velocity is as high as twice the time-averaged one.

7.3.2 Solute transport

Once the flow field has developed, a passive, conservative tracer was released at the entrance gate of the main chamber. Figure 7.7 shows the cloud of tracer transported by the time-averaged flow simulated through RANS (a) and by the unsteady flow simulated through LES (b). The Sc_t for both simulations is set to be 0.7, which was suggested by Launder (1978) and is commonly used in commercial codes as a default value (FLUENT user's guide, 2003). Most of the tracer is distributed within the width of short-circuiting path when it is transported by the time-averaged flow field. Some portion of tracer is trapped in the right side corner, and sluggish movement due to the wall shear is found near the baffle. The concentration of the tracer diffuses into the recirculation zone in the early time step is already unobservable, and only weak diffusion is shown in the narrow baffle spacing along the streamlines right next to the short circuiting path. On the other hand, the tracer along the unsteady flow field shows stronger dispersion than the RANS case. The tracer concentration which is similar to that in the short-circuiting path is observed even in the center of the recirculation, being convected to that position within short time period. In addition, high concentration in the recirculation zone is found along

the streamlines indicating that the tracer transport between recirculation zone and the short-circuiting path occurs not only by diffusion but also by advection. Due to these significantly distinct tracer transport patterns, it is expected that both simulations will predict the reactor performance quite differently.

The transport characteristics of solutes in ozone contactors can be quantified with a residence time distribution (RTD) plot. The tracer is sampled and integrated over the chamber exit plane. Figure 7.8 presents the normalized concentration, $E = (C \times t_{HRT}) / \sum (C \times \Delta t)$, and its cumulative value, *F*, as a function of normalized time scale, t / t_{HRT}, for selected cases (i.e., 1W, 3W, and 5W), where t_{HRT} is calculated as the chamber volume divided by the discharge. The computed results from RANS with Sc_t = 0.7 and smallest time step on the finest grid (solid black lines) are compared with the results from LES. As expected from the afore discussed contour plots, the RANS predicted peak concentrations are severely overpredicted and are approximately four times higher than the LES predictions (solid lines with open circles). The cumulative distributions reflects this behavior as such that the residence time as predicted by RANS is much shorter than what LES predicts. This is particularly severe in the W3 and W5 cases.

7.3.3 Turbulent Schmidt Number Calibration

By definition, turbulent mixing is controlled by the eddy viscosity and the turbulent Schmidt number. The eddy viscosity is calculated together with the time-averaged velocity distribution prior to the tracer transport equation simulation. Hence, the Sc_t is considered the only physical parameter that can be calibrated in RANS models of

tracer transport. This was done by tuning Sc_t to make the RANS simulation provide similar RTD curves to those obtained from LES.

In Figure 7.8 the resulting RTD curves from the calibrated RANS simulations are plotted as dashed lines and the last number in the legend provides the turbulent Schmidt number necessary to achieve a good match to the LES. While for the W1 case the Schmidt number was found to be 0.001, i.e. approx. 2 orders of magnitude smaller than the default value, it had to be reduced by another order of magnitude for the W3 and W5 cases. Hence, not only is there a significant and unphysical reduction in turbulent Schmidt number necessary but also is Sc_t not universal and varying from case to case. Such a small Schmidt number can be attributed to the fact that the numerics employed in this study feature very little numerical diffusion, i.e. a very fine grid, a small time-step together with higher order convection, diffusion and time discretization schemes.

The effect of numerical diffusion on the tracer transport is investigated by varying grid resolution and time step size. Figure 7.9 represents the T_{10} values of the RTD curve for different grid and time step sizes. T_{10} is defined as the detention time when 10% of tracer has exited from a chamber volume. This value has been treated as the main indicator of the reactor performance. If this value is greater than 0.7, the reactor is considered to perform superior (USEPA 1999). The dashed lines in the figure indicate the results from the LES for each baffle spacing, and the other lines with symbols are from RANS. The effect of the time step size are also compared in separate plots aligned to the right. The upper figures are the results of the $Sc_t = 0.7$ simulations. With the increase in baffle spacing, T_{10} has decreased from the value of superior to poor performance within the baffle spacing five times wider. The values of the results from RANS are also similar in all case studies. The figures shown below of them are the results of lower Sc_t. Sc_t was calibrated to the value until the RTD curves match to that of LES within 5% error, and

the obtained values are between 0.001 and 0.0003, which are significantly lower than 0.7. Interestingly, even though the values somewhat decrease or increase with the increase in grid and time step sizes, their effect, as well as Sc_t's effect, was little on the T_{10} values.

Figure 7.10 shows the peak concentration, E_{max}, in the same manner with the plots of the T_{10} values. As observed in Figure 7.8, E_{max} is affected dramatically by time step size and Sc_t, and the grid size effect is also observed when Sc_t=0.7. With the increase in grid size, E_{max} decreases about 30% with the smallest Δt, and 5% in the largest Δt cases. In smaller Sc_t condition, the grid size shows little effect on E_{max}. Meanwhile, when time step size is increased, E_{max} is decreased 60-70% with both higher and lower Sc_t.

Another parameter indicating the dispersion in the chamber through the RTD curve, known as "Morill index" (MI) calculated as T_{90}/T_{10}, is examined in Figure 7.11 with the same approach of previous figures. Here T_{90} is defined in similar fashion with T_{10} as the detention time at 90% of tracer has exited the reactor. Plots with the higher Sc_t, MIs for all baffle spacings are significantly lower than those of LES, and they were hardly affected by grid nor time step sizes. Instead, the MIs for all baffle spacings are almost the same within the range between 1.2 and 2.0. In contrast, if lower Sc_t is used, MIs are widely spread with the increase in baffle spacing at similar levels than the LES cases. In widest chamber, MI increases up to 13 with the maximum time step size. Again, the influence of grid and time step sizes is negligible. Both LES and RANS results show the greater increment between 1W and 2W than 3W and 5W. It implies that the effect of the large recirculation on the dispersion of RTD curve decays after the recirculation occupies the chamber height (between W2 and W3).

According to USEPA (1986), if MI is less than 2.0, the reactor is considered as effective, and in completely mixed reactor the value can increase to 21.0. In most

regulations, such as USEPA guides (1986, 1999), only the time parameters T_{10} and/or MI are used to assess the reactor performance. It is because these indicators are based on the RTD curves from experiments, and thus there is no risk to rate the reactor performance with only these values. However, with the higher Sc_t, which has been widely employed in many turbulent flow cases, RANS approach with time-averaged flow field can mislead the reactor efficiency, especially on MI value.

Based on the above analyses, the Sc_t for RANS should be calibrated for each geometry with the two indicators, E_{max} and MI, along with the grid and time step dependency. The available Sc_t should be found within the range where the three values are all independent of grid and time step sizes. Figure 7.12 shows these two indicators for the present study with respect to the baffle spacing. The calibrated diffusivity, which is the inverse of Sc_t, is found to be proportional to both MI and E_{max}.

7.4 Conclusion

Turbulent Schmidt number for RANS simulations for different baffle spacing ozone contactor models were investigated with the comparative LES simulations. Regardless of grid resolution, RANS simulations could reproduce reasonable hydraulic characteristics in various baffle spacings. In contract, the tracer RTD curves with commonly used turbulent Schmidt number of RANS significantly deviated from those obtained by LES. This discrepancy was reduced by turbulent Schmidt number calibration. The effect of the turbulent Schmidt number on the RTD accompanied by the dependency of numerical grid and time step size was examined. This investigation was conducted using three RTD curve indicators, T_{10}, E_{max} and Morrill index. The first indicator T_{10}, which is the most commonly used indicator for reactor design, was did not

reflect the poor performance of the uncalibrated RANS simulations since the value was independent of all parameters, even turbulent Schmidt number. The maximum concentration, E_{max}, provided better index, however this value was found to be very sensitive to time step size for all turbulent Schmidt number range, but becomes independent of grid size with lower turbulent Schmidt number. The RTD dispersion indicator, MI, depended mainly on the turbulent Schmidt number and not so much on grid resolution or time step suze. The tracer diffusivity was found to be proportional to the MI and E_{max} value with an increase in baffle spacing. Therefore, reactor designers can calibrate turbulent Schmidt numbers for RANS simulation if they have reference data for at least two extreme cases (narrowest and widest chambers) using these two parameters.

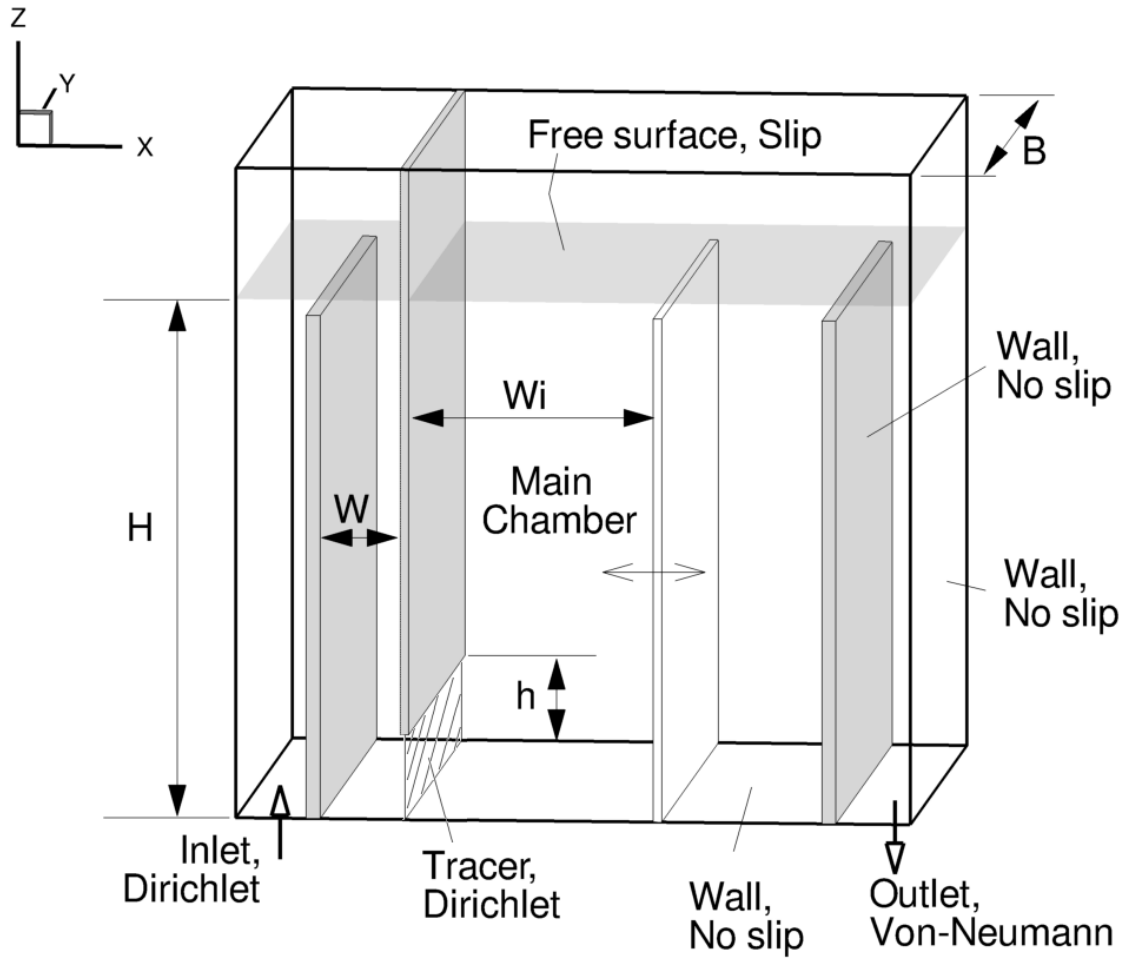

Figure 7.1 Layout and boundary conditions of the variable baffle spacing ozone contactor investigated in this study.

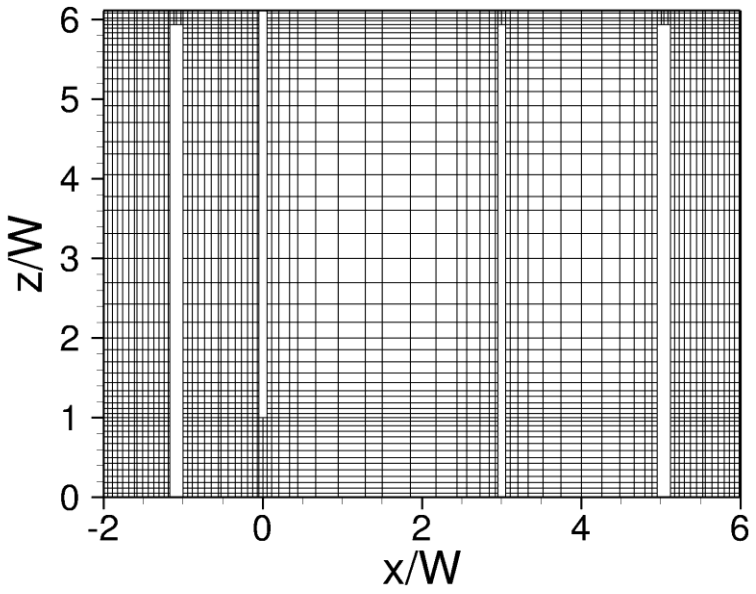

Figure 7.2 Front view of the computational grid of the 3W case (only every fifth grid line is plotted).

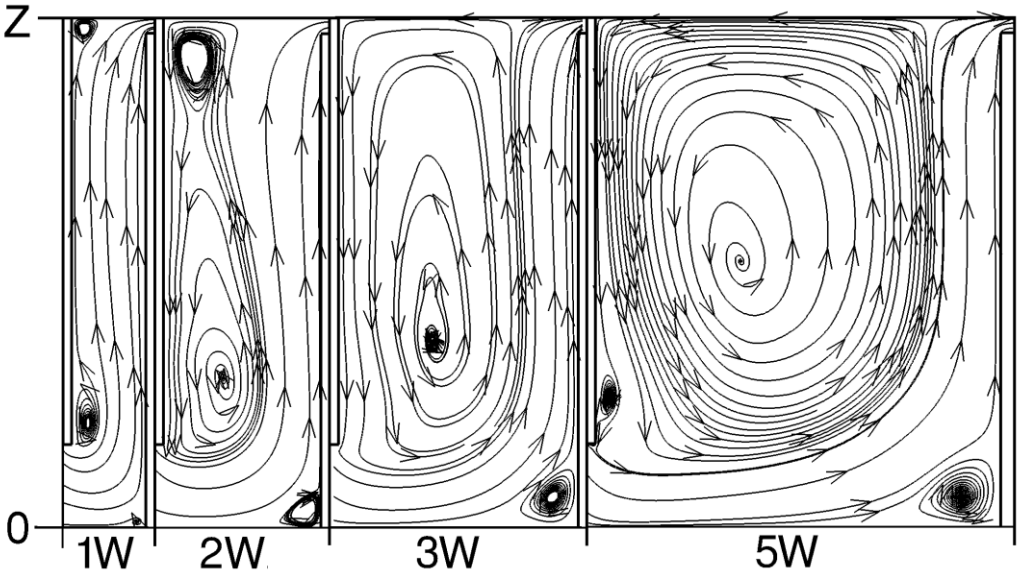

(a)

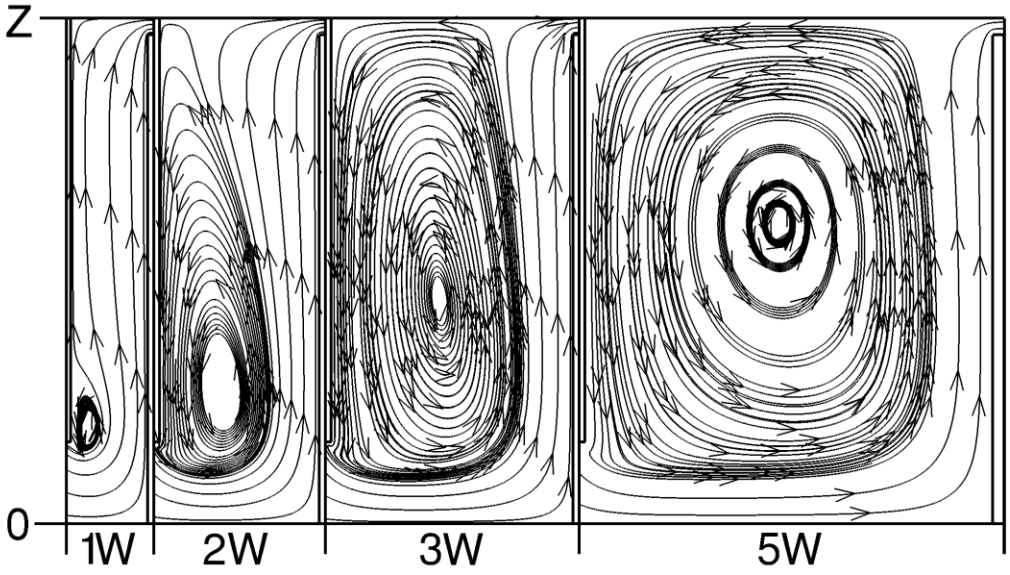

(b)

Figure 7.3 Streamlines in each main chamber predicted by (a) LES and (b) RANS

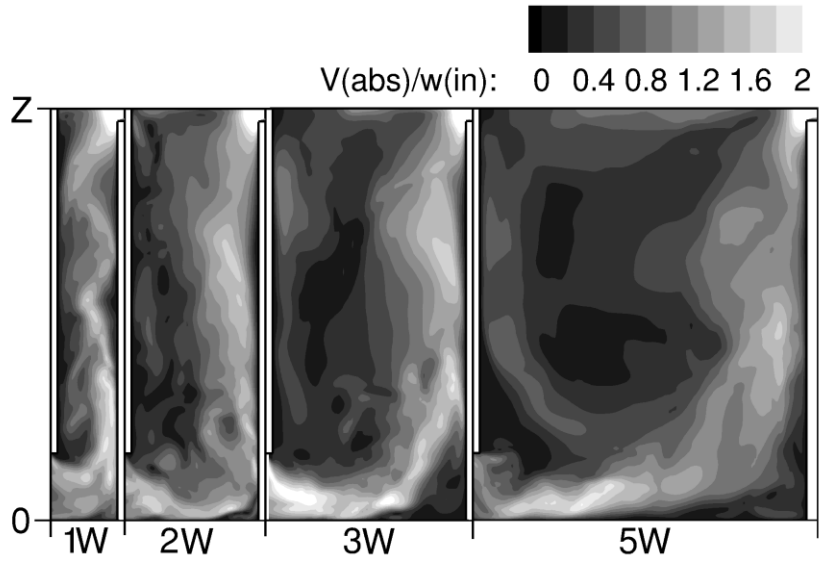

(a)

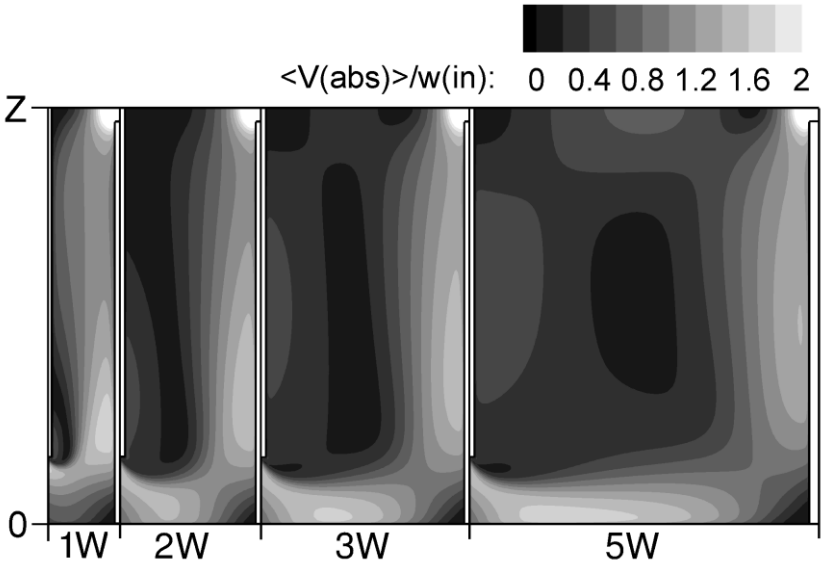

(b)

Figure 7.4 Absolute velocity distributions in each main chamber: (a) instantaneous velocity field from LES and (b) time-averaged velocity field from RANS

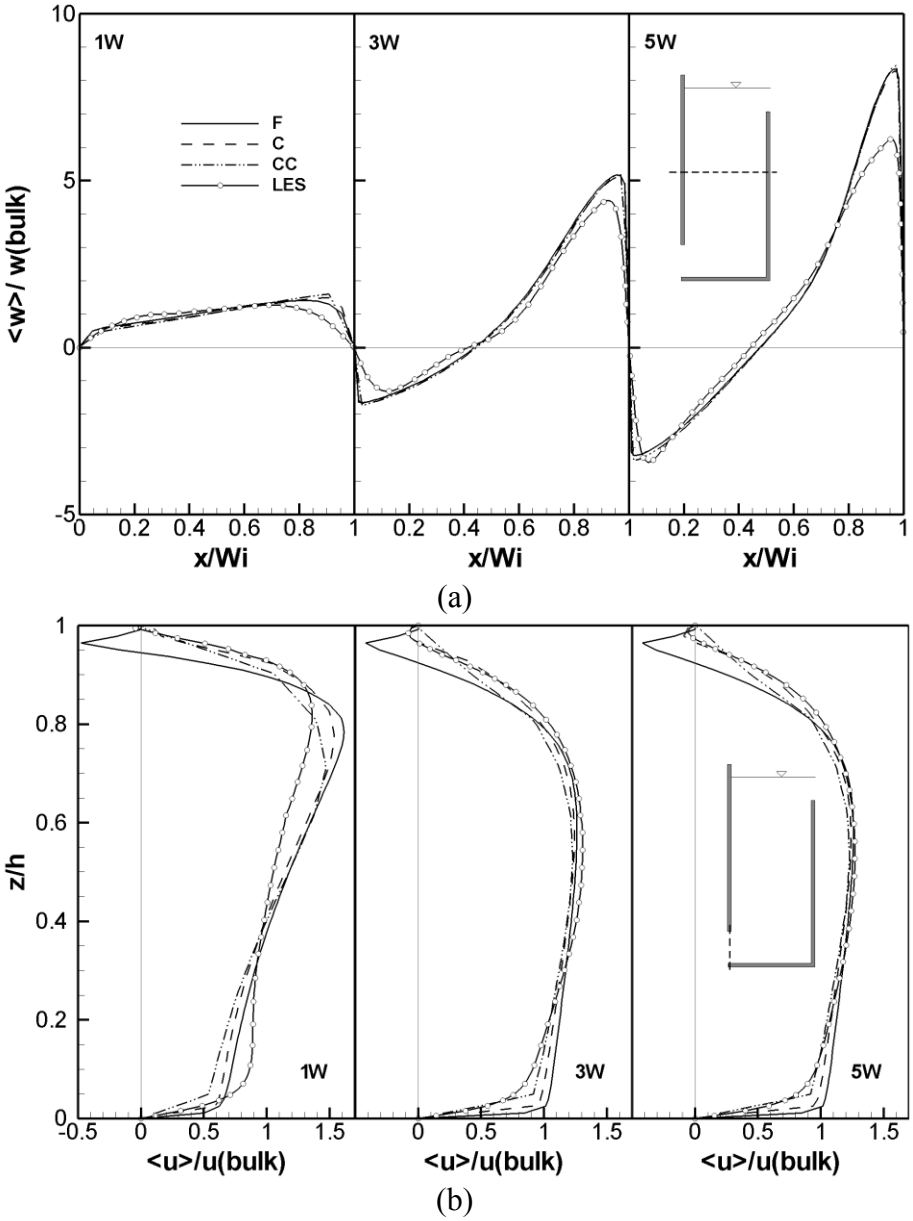

Figure 7.5 Velocity profiles at selected locations: (a) vertical component distribution along horizontal line across the baffle spacing and (b) horizontal component distribution along vertical line at the entrance gate of the main chamber

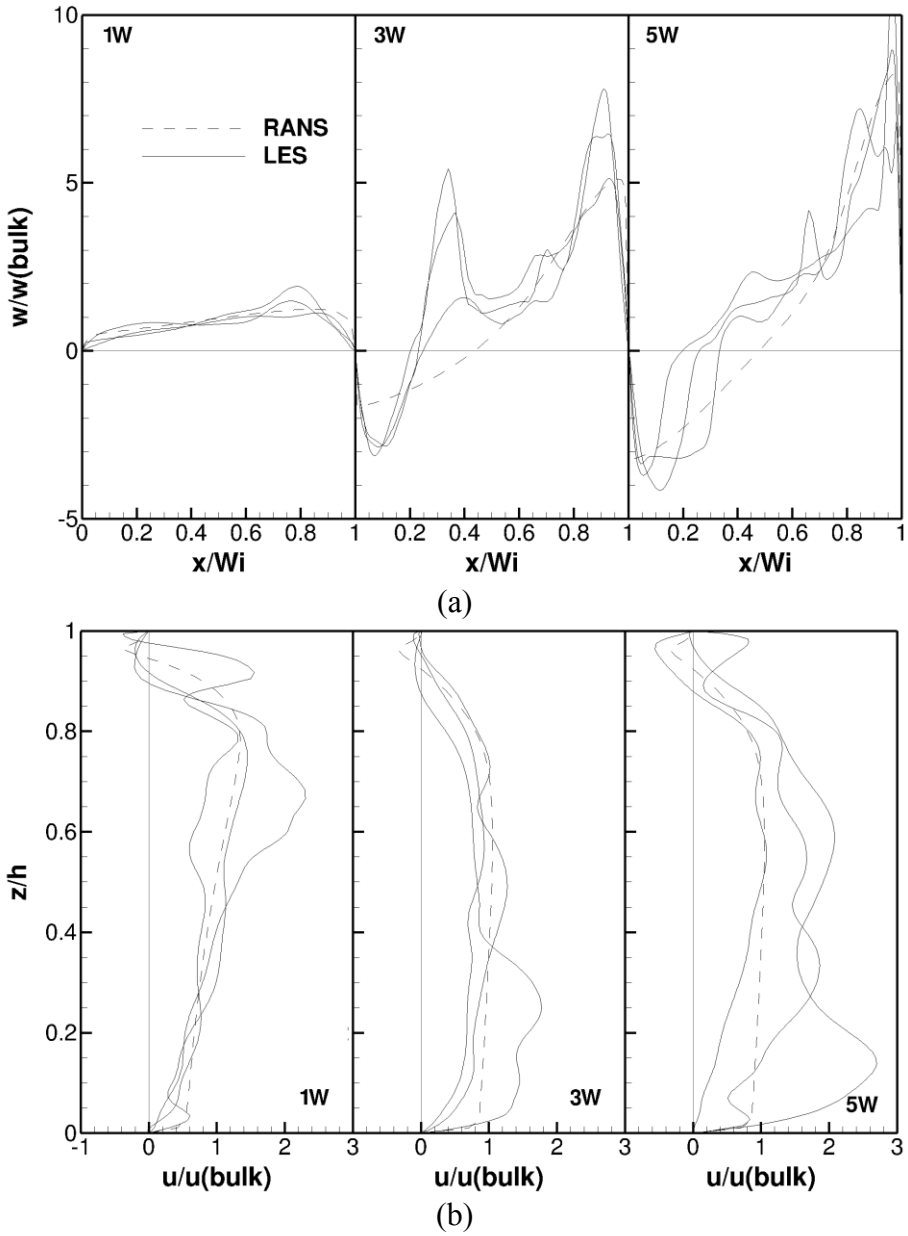

Figure 7.6 Velocity profiles at three arbitrary instants in time from the LES and time-averaged velocity profiles from RANS at the same locations as in Figure 7.5: (a) vertical component distribution along horizontal line across the baffle spacing and (b) horizontal component distribution along vertical line at the entrance gate of the main chamber

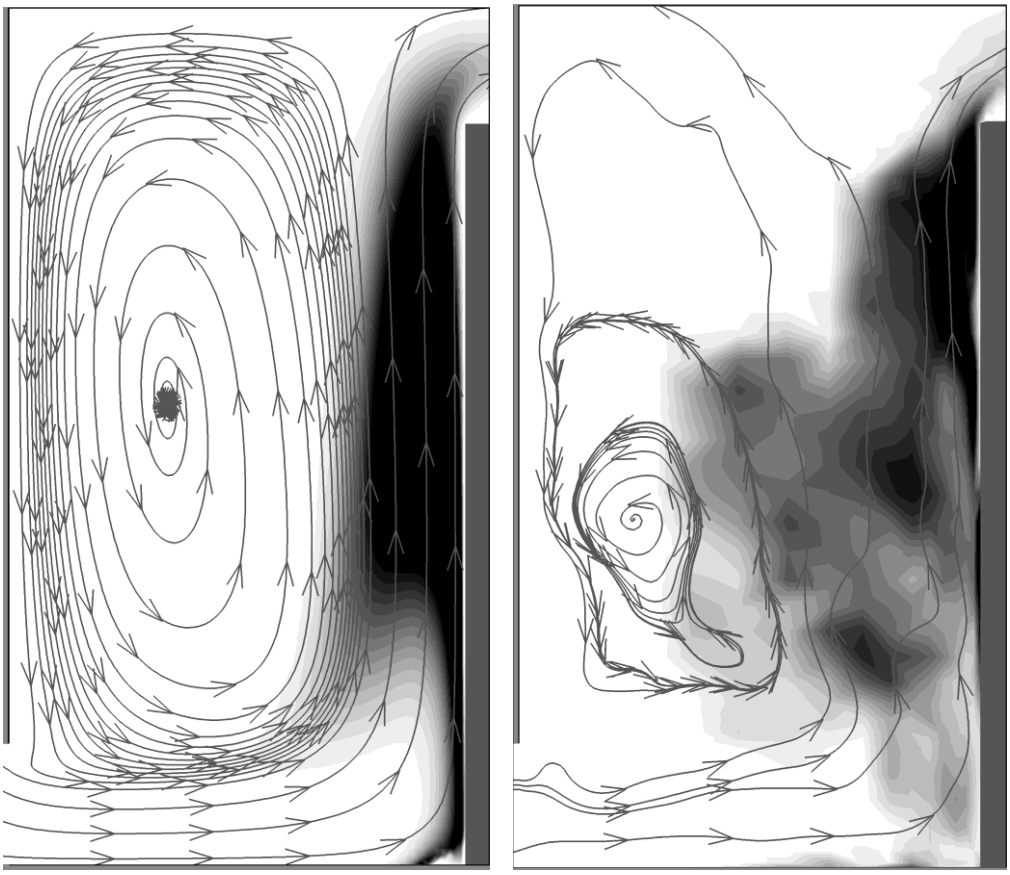

(a) (b)

Figure 7.7 Tracer transport at an instant in time along (a) time averaged flow field and (b) fluctuating unsteady flow field (both with $Sc_t = 0.7$ in 3W chamber)

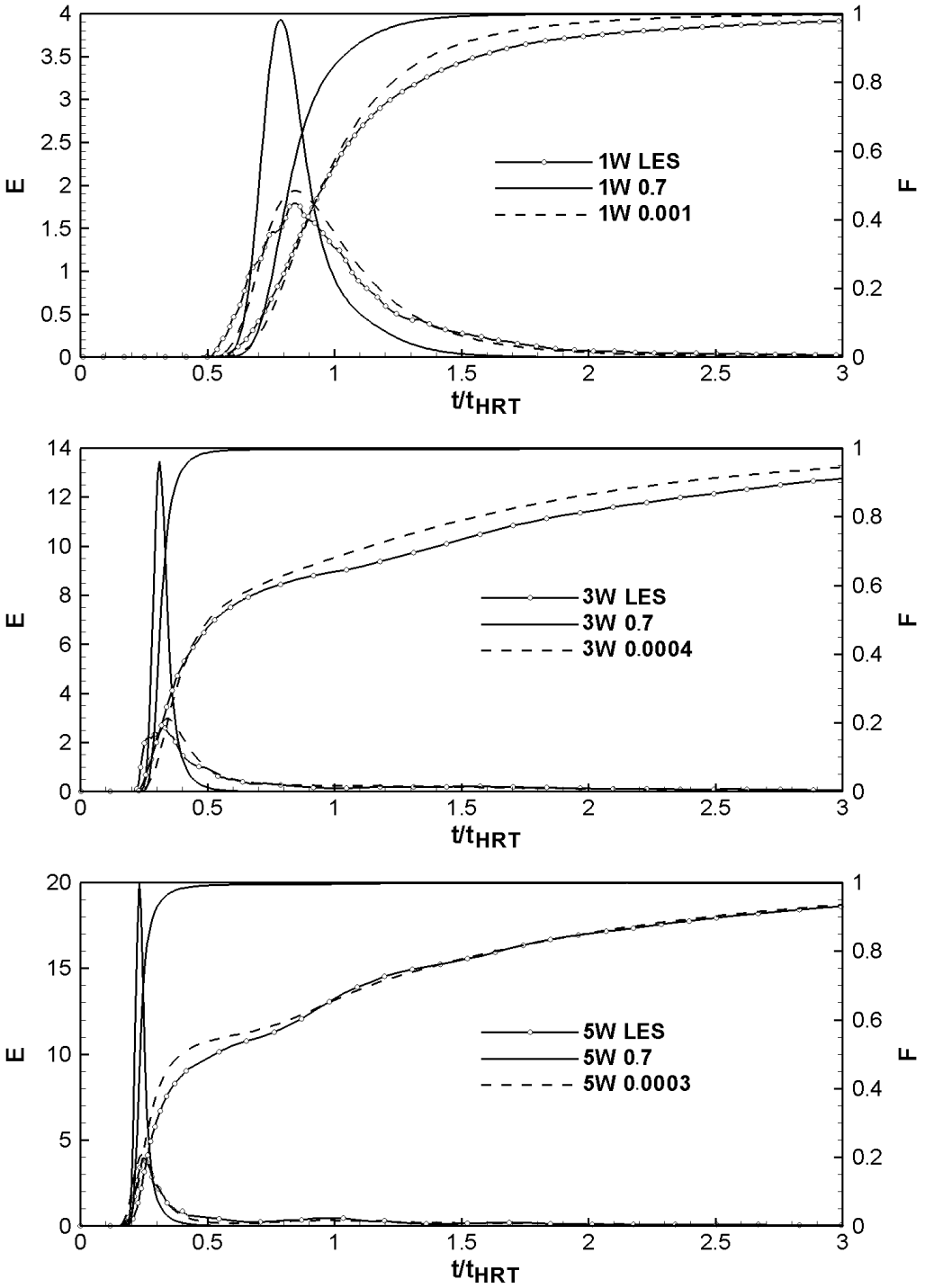

Figure 7.8 LES and RANS predicted (condition: fine grid, $\Delta t/t_{HRT,1W}$ = 8E-04, and Sc_t = 0.7 and calibrated for each baffle spacing) RTD curves for 1W, 3W, and 5W cases

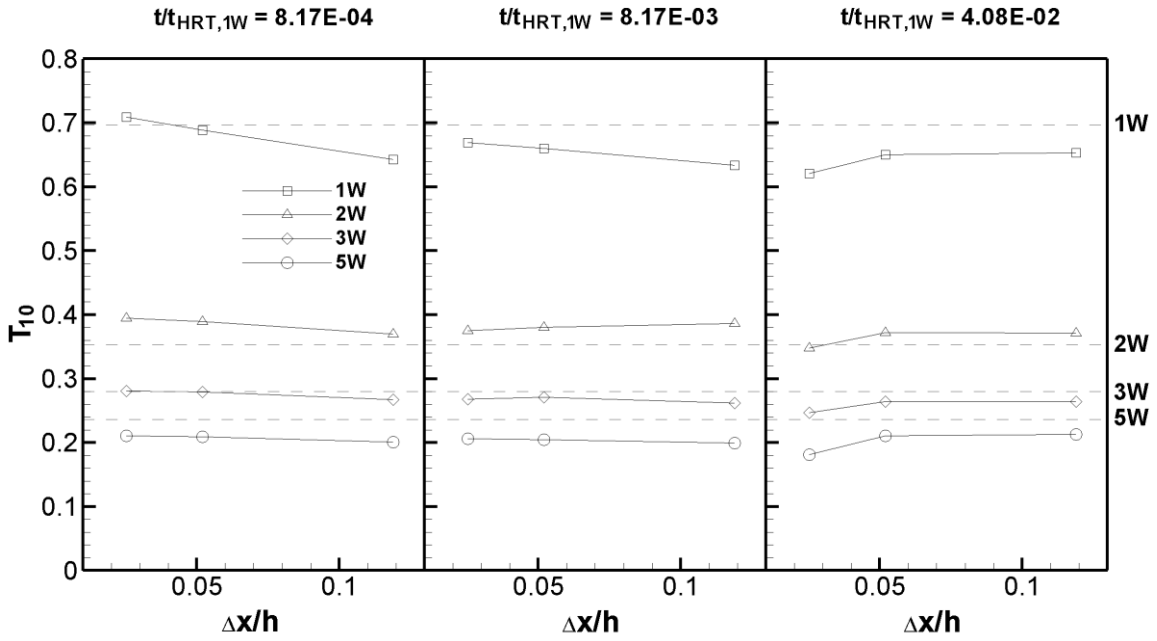

(a)

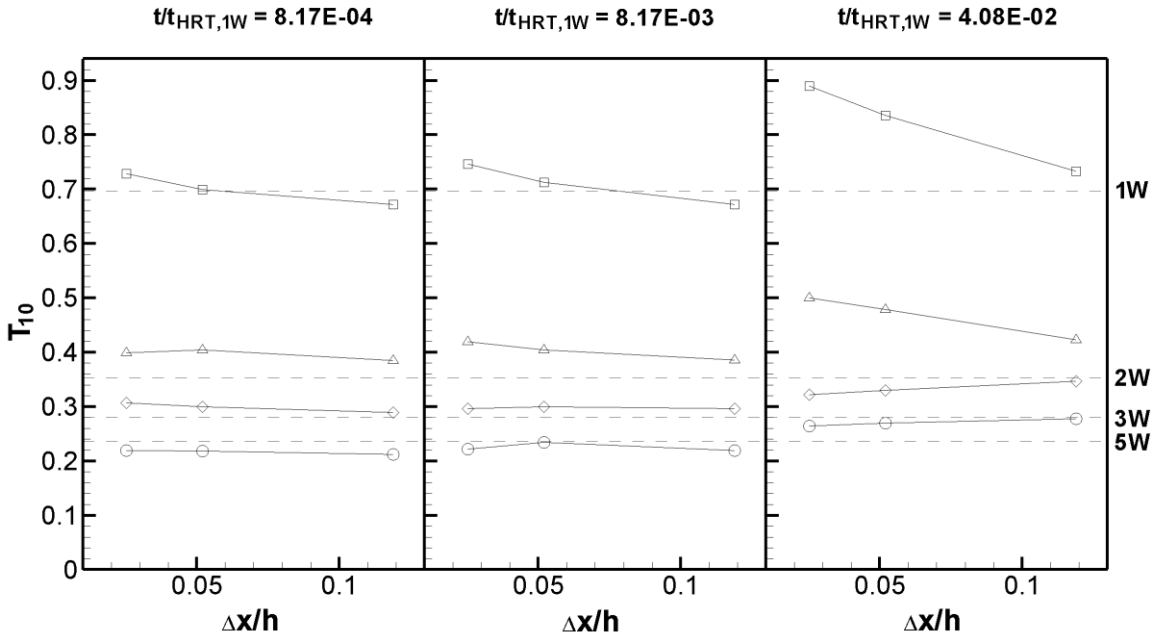

(b)

Figure 7.9 Grid and time step size effect on T_{10}: (a) Sc_t = 0.7 fixed and (b) Sc_t = 0.001 ~ 0.0003

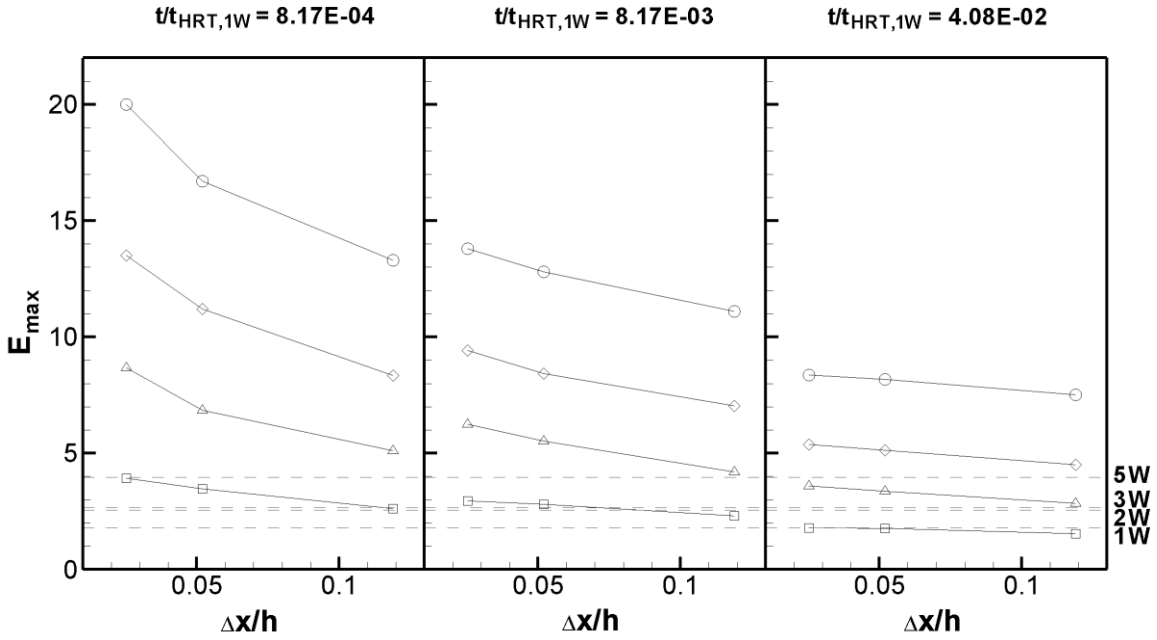

(a)

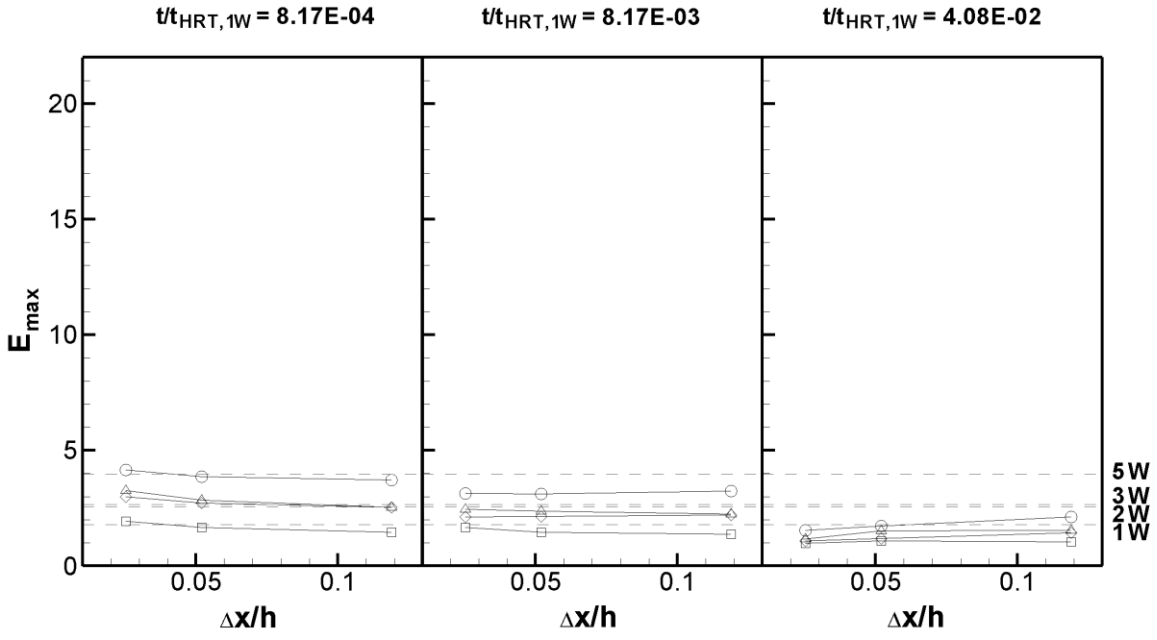

(b)

Figure 7.10 Grid and time step size effect on E_{max}: (a) Sc_t = 0.7 fixed and (b) Sc_t = 0.001 ~ 0.0003

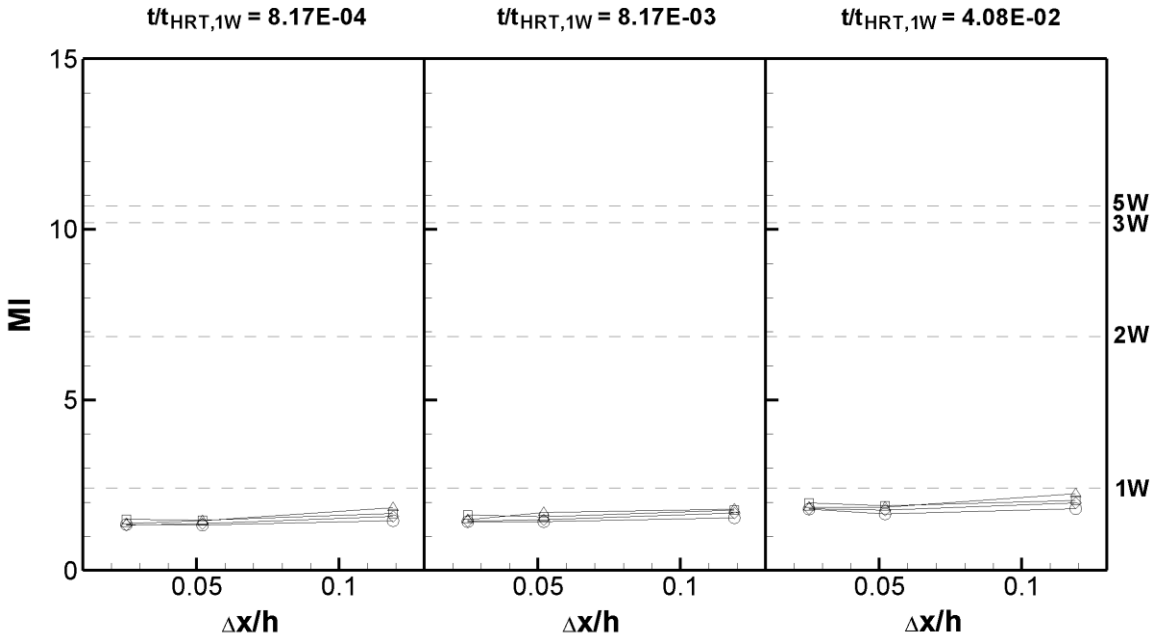

(a)

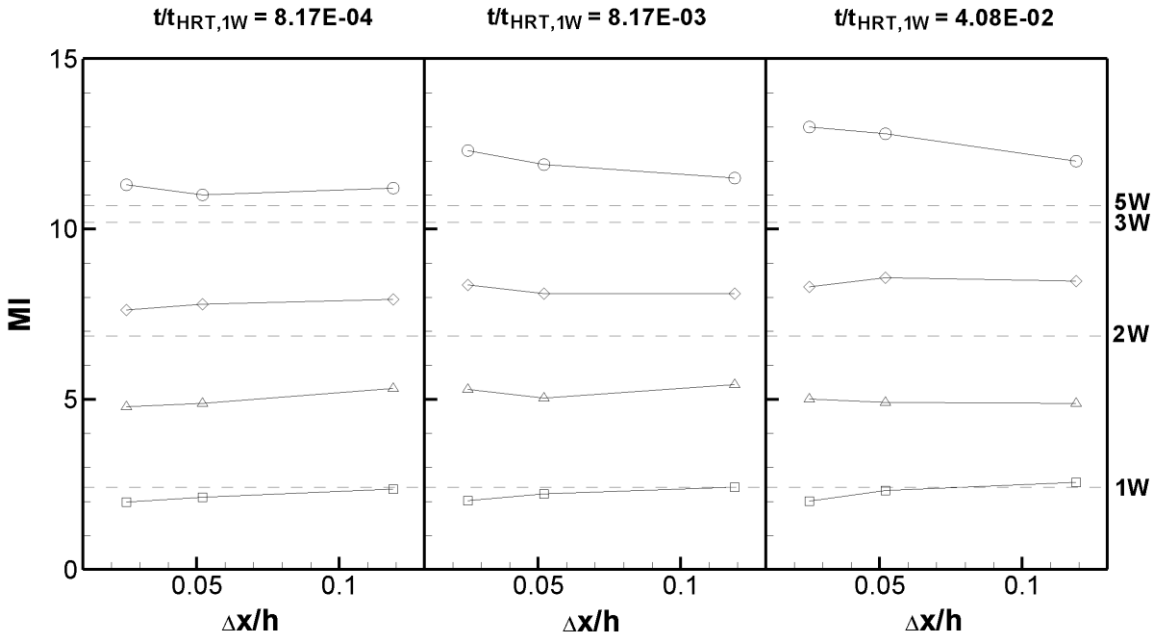

(b)

Figure 7.11 Grid and time step size effect on MI: (a) $Sc_t = 0.7$ fixed and (b) $Sc_t = 0.001 \sim 0.0003$

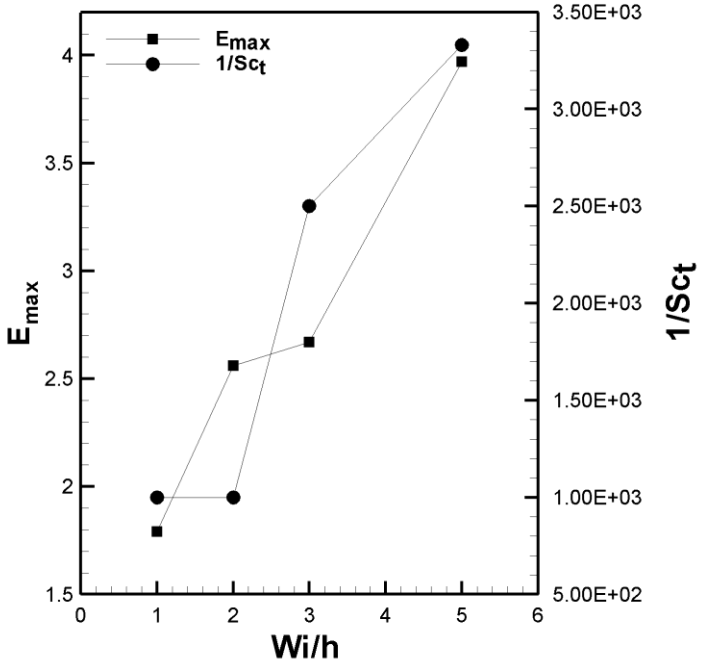

(a)

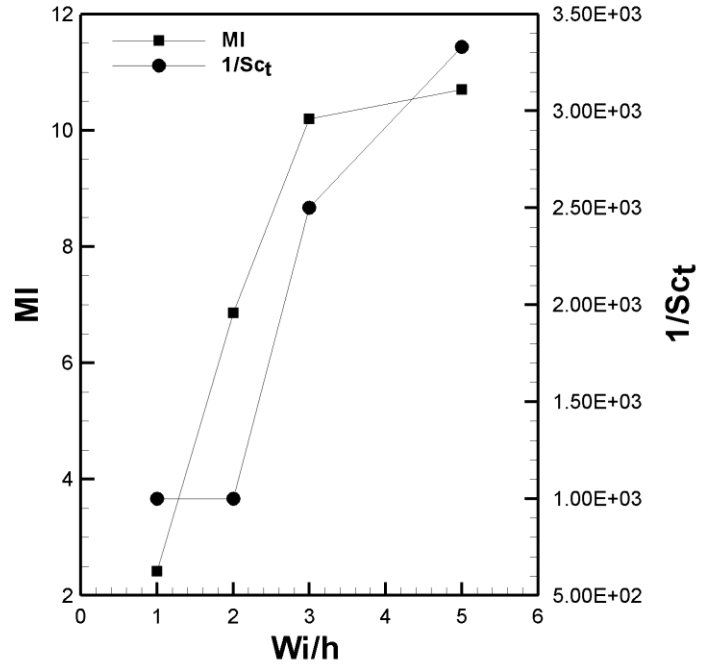

(b)

Figure 7.12 Calibrated diffusivity (1/ Sc_t) vs. (a) E_{max} and (b) MI for each baffle spacing

CHAPTER 8

SUMMARY AND CONCLUSIONS

This dissertation provides a thorough understanding of the hydrodynamics and solute transport phenomena in water treatment ozone contactor models through numerical simulations using large eddy simulation (LES) methods. The thesis also presents modeling and numerical aspects for simulations that are based on the Reynolds Averaged Navier-Stokes (RANS) equations. The contactor geometries investigated in this research were Constant Baffle Spacing Multi-Chamber (CBSMC) ozone contactors and a Variable Baffle Spacing ozone contactor Model (VBSM). Two different baffle spacing, a normal-spacing (NS) and a half-spacing (HS), were considered for the CBSMC study. The VBSM was developed and used to investigate the baffle spacing effect and to suggest the optimal design baffle spacing. The VBSM was also employed examining the optimal turbulent Schmidt number for the RANS simulation. The results of this study are summarized as follows:

LES of Constant Baffle Spacing Multi-Chamber (CBSMC) ozone contactors

The occurrence of deficient flow conditions and non-ideal solute transport behaviors in the two multi-chamber ozone contactors was examined herein. Specifically, the flow through these reactors is characterized by the presence of extensive short-circuiting from one chamber to the next, a large internal recirculation that contributes to mixing and a dead zone in the center of each chamber. The LES results also suggested that the flow is highly three dimensional with a pair of symmetric counter-rotating secondary vortices and nodal points in the centre of the recirculation zones. The hydrodynamic deficiencies could be partially prevented by decreasing the baffle spacing. The present LES was performed for only two representative designs, and other design

options need to be studied further. Nevertheless, this study showed that LES can be a useful tool for new plant design as well as retrofitting existing reactors for better process efficiency.

LES and RANS of Constant Baffle Spacing Multi-Chamber (CBSMC) ozone contactors

The distributions of time-averaged velocity contours of the LES are very similar to those predicted by RANS demonstrating that the RANS turbulence closure model captures the effect of large-scale turbulence on the mean flow reasonably well. The maxima of velocity profiles from RANS are quite similar to those of the instantaneous LES, whereas they are 15 ~ 30% less when compared with the time-averaged LES. The tracer concentration predicted by LES accurately reproduces the measured distribution, while in RANS almost all tracer transports along the short-circuiting path and a relatively small amount of tracer resides in the recirculation area. The periodic boundary condition used in this simulation did not accurately represent the inlet flow condition of the laboratory experiments; however, magnitude and the shape of the LES computed RTD curves matched experimental observations quite well. The RTD curves based on RANS show much more severe short circuiting and exhibit pronounced secondary peaks, and hence the predicted results deviate largely from the ones measured.

LES of Variable Baffle Spacing ozone contactor Model (VBSM)

The LES results confirmed that the baffle spacing is a critical parameter in the design of an ozone contactor. The simulations provided first and second order statistics of the hydrodynamics in several ozone contact chambers with a baffle spacing varied between 0.5 times to 5 times the size of the base chamber. The simulations showed that in each chamber the width of a large recirculation grows at about the same rate as the baffle spacing resulting in only a little increase in the width of the short-circuiting path. The

turbulence statistics are characterized by the flow unsteadiness and elevated levels of turbulence are found in the short-circuiting flow path. The tracer is dispersed along the short-circuiting path and into the recirculation zone due to turbulent mixing. The RTD curves compare very well with experimentally obtained data. The most favorable flow behavior (i.e., a minimum amount of short circuiting and almost no internal recirculation) and propitious tracer transport characteristics were obtained when the baffle spacing corresponded to the chamber entrance gate height. The three dimensional LES has proven to be an accurate, and hence reliable tool for predicting ozone contactor performance without the need for calibration of model constants.

LES and RANS of Variable Baffle Spacing ozone contactor Model (VBSM)

The effect of turbulent Schmidt Number of the RANS simulations for different baffle spacing ozone contactor models were investigated with analogous LES. Regardless of the grid resolution, the RANS model could reproduce reasonable time-averaged hydraulic characteristics in various baffle spacing arrangements. However, there was a significant discrepancy in the tracer RTD curves predicted by RANS when an un-calibrated turbulent Schmidt number was used. The effect of the turbulent Schmidt number for RANS was investigated and accompanied by an examination of the effects of spatial and temporal resolution. The first RTD performance indicator T_{10} was independent of all parameters, and thus not the proper indicator for the calibration of turbulent Schmidt number for RANS simulations. The maximum concentration, E_{max}, was very sensitive to the time step size for all turbulent Schmidt numbers used. E_{max} is independent of grid size when a calibrated turbulent Schmidt number is used. The third indicator, MI value, only showed a dependency on the turbulent Schmidt number. The tracer diffusivity was proportional to the MI and E_{max} value with an increase in baffle spacing.

CHAPTER 9

RECOMMENDATIONS FOR FUTURE RESEARCH

The recommendations for future works are as follows.

Large Eddy Simulation (LES) for Reactive Tracer Transport

The use of ozone in water treatment is generally based on the concept that reactions occur between dissolved ozone with water-soluble substance. The reaction kinetics between the substance and ozone is usually based on the classical first-order Chick-Watson inactivation model (Haas and Karra, 1984). Using the inactivation rate from the model, a convection-diffusion formulation with a sink term representing ozone decay (Van der Walt, 2002) can be used to model the reactive tracer transport. In most of the previous studies, RANS based methods were used (Huang et al. 2004, Wang et al. 1998), but LES based reactive tracer studies are yet to carry out. The application of LES on the reactive tracer test is attractive since the Chick-Watson model, which has been broadly used due to its simplicity, cannot account for deviation from the first-order inactivation kinetics (Carlson 1999, Lawler and Singer 1993). LES which provides accurate hydrodynamics at every time step may be effective in overcoming the aforementioned drawbacks.

Hydrodynamics and tracer transport of the UV reactor using LES

Like Ozone, UV is a promising alternative to Chlorine for wastewater disinfection process. Investigation on the hydrodynamics and conservative and reactive tracer transport in the UV reactor using LES is considered a novel approach (Wols et al. 2010).

Employing intensity distribution and reaction kinetic equation, the effect of the circular lamp on the performance of disinfection with reaction can be investigated.

Particle Tracking Method with LES

For dose analysis in reactive tracer test, a Lagrangian approach to determine the rate of disinfection is more intuitive. In this approach, particles will be numerically introduced into the flow, and their trajectories through the disinfection system will be tracked over time. Different particles on different trajectories will be exposed to different background concentration or UV intensities, and hence will accumulate different exposure doses, and so will differ in the probability of survival or inactivation. Employing particle tracking method on parallel processing programs is not as simple as the concept of the method itself. The effective decomposition of the storages for each particle should be considered. Yet, as shown in this dissertation, accurate prediction without calibration of turbulent diffusivity using LES with effective parallel computing can be a powerful and reliable tool.

Quasi Two Dimensional LES for contactor

There have been efforts to reduce the computational cost of LES method since it is still very expensive for practical and broad applications. Hinterberger et al. (2002) suggested a so-called 2D Depth-Averaged (DA) LES model for shallow water flow using a modified eddy viscosity expressed through the water depth in DA equations. However, this approach is limited to features that are larger than 5 times the water depth, and also there should be minor effect of secondary currents. In order to use such a 2D-DA calculations in the domain with deep water depth, such as ozone contactor, may require additional models including the effects of the unresolved subdepth-scale 3D turbulence.

REFERENCES

Boussinesq (1877). "Essai sur la Théorie des Eaux Courantes." ('Essay on the Theory of Water Flow.') *Mémories présentés par divers savants à l'Académie des Sciences*, Paris, France, 23, ser 3, 1, supplement 24, 1281-1302 (in French).

Breuer, M. (1998). "Large eddy simulation of the subcritical flow past a circular cylinder: Numerical and modeling aspects." *Int. Journal Numer. Meth. Fluids,* 28, 1281-1302.

Courant, R., K.O. Friedrichs, and H. Lewy. (1928). "Über die partiellen Differenzengleichungen der mathematischen Physik", *Mathematische Annalen*, 100(1), 32-74.

Deardorff. (1970). "A numerical study of three-dimensional turbulent channel flow at large Reynolds numbers." *Journal Fluid Mech.,* 41(2), 453-480.

Do-Quang, Z., Ramirez, C. C., and Roustan, M. (2000). "Influence of geometrical characteristics and operating conditions on the effectiveness of ozone contacting in fine-bubbles conventional diffusion reactors." *Ozone-Sci. Eng.,* 22 (4), 369-378.

Dong, Yu-Hong, Lu, Xi-Yun, and Zhuang, Li-Xian. (2003). "Large eddy simulation of turbulent channel flow with mass transfer at high-Schmidt numbers," *Int. Journal Heat and Mass Tran.,* 46, 1529-1539.

de Bruyne M, Clyne P., Carlson J. (1999). "Odor coding in a model olfactory organ: the Drosophila maxillary palp." *J. Neurosci*. 19, 4520-4532.

Ferziger, J.H. (1993). *Estimation and reduction of numerical error*. Presented at ASME Winter Annual Meeting, Washington.

Ferziger, J.H. and Peric, M. (2002). *Computational Methods for Fluid Dynamics*. Springer-Verlay, third-edition.

Fischer-Antze, T., Stoesser, T., Bates, P. and Olsen, N.R.B. (2001). "3D numerical modelling of open-channel flow with submerged vegetation", *IAHR Journal of Hydraulic Research*, No. 3.

Fluent™ user's guide ver. 6.1, http://202.185.100.7homepagefluenthtml/ugnode314.htm (Accessed June 11, 2009)

Germano, M., Piomelli, U., Moin, P., and Cabot, W.H. (1991). "A dynamics subgrid-scale eddy viscosity model.", *Phys. Fluids A*, 3, 1760-1765.

Gualtieri, C. (2006a). "Numerical simulations of flow and tracer transport in a disinfection contact tank." *iEMSs 2006*, Burlington, Vermont, USA.

Gualtieri, C. (2006b). "Numerical simulation of RTD in contact tanks with COMSOL multiphysics." *COMSOL User Conference 2006*, Napoli, Italy.

Gualtieri, C. (2007). "Analysis of the effect of baffles number on a contact tank efficiency with multiphysics 3.3." *COMSOL User Conference 2007*, Napoli, Italy.

Hart, F.L., and Gupta, S.K. (1978). "Hydraulic analysis of model treatment units." *Journal of the Environmental Engineering Division, ASCE,* 104(EE4), 785-798.

Haas, C.N. and Karra, S.B. (1984). "Kinetics of Microbial Inactivation by Chlorine-I: Review of Results in Deman-Free Systems." *Water Research*, 18(11), 1443-1449.

He, Y., Guo, Y., Hsu, A.T. (1999). "The effect of Schmidt number on turbulent scalar mixing in a jet-in-crossflow." *International Journal of Heat and Mass Transfer*, 42, 3727-3738.

Heathcote, G. R. (1994). "Development of an ozone disinfection contactor using a physical scale model." *Ozone-Sci. Eng.,* 17(1), 15-24.

Henry, D.J., and Freeman, E.M. (1995). "Finite element analysis and T-10 optimization of ozone contactors." *Ozone-Sci. Eng.*, 17(6), 587-606.

Hinterberger, C., Frohlich., J., and Rodi., W. (2002). "Depth-averaged large eddy simulation of shallow water flows-modeling aspects." Proc., 9th European Turbulence Conf. Advances in Turbulence IX, I.P. Castro and P.E. Hancock, eds., CIMNE, Barcelona, Spain, 211-214.

Huang, T., Brouckaert, C.J., Pryor, M., and Buckley, C.A. (2004). "Application of computational fluid dynamics modeling to an ozone contactor." Water SA, 30, 1, 51-56.

Jimmenez, C., Ducros, F., Cuenot, B., and Bedat, B. (2001). "Subgrid scale variance and dissipation of a scalar field in large eddy simulations." *Phys. Fluids*, 13(6), 1748-1755.

Kim, C.J. (1998). *Guide – Computational Fluid Dynamics: Basic to 3D Non-Orthogonal Grid Modeling*. Moonoondang. Seoul.

Kim, J. H., von Gunten, U., and Mariñas, B. J. (2004). "Modeling bromate formation and *Cryptosporidium parvum* inactivation in synthetic waters." *Environ. Sci. Technol.*, 38 (7), 2232-2241.

Kim, D. I. (2007a). "Development and application of integrated ozone contactor design and optimization tools." PhD. Thesis, Georgia Institute of Technology., Atlanta, Georgia, USA.

Kim, D. I., Tang, G., Hasan, S., Mariñas, B. J., Couillard, L., Shukairy, H. M, and Kim, J. H. (2007b). "Simultaneous simulation of pathogen inactivation and bromate formation in a full-scale ozone contactor by computer software." *J. Am. Water Works Ass.*, 99(8), 77-91.

Kim, D., Kim, J.H., and Stoesser, T. (2009) "LES and RANS modeling of Flow in an Ozone Contactor: Mean and Instantaneous Turbulent Flow Characteristics." 33rd International Association of Hydraulic Engineer Research (IAHR) Congress.

Kim, D.I., Elovitz, M., Roberts, P. J., and Kim, J. H. (2010a). "Investigating multi-chamber ozone contactor using 3D Laser Induced Fluorescence." *J. Am. Water Works Ass.*

Kim, D., Kim, D.I., Kim, J.H., and Stoesser, T. (2010b). "Large Eddy Simulation of Flow and Tracer Transport in Multi-Chamber Ozone Contactors." *J. Env. Eng.,* 136(1), 22-31.

Launder, B.E. (1972). *Mathematical models of turbulence*, Academic, New York.

Launder, B.E. and Spalding, D.B. (1974). “The numerical computation of turbulent flows.” *Computer Methods in Applied Mechanics and Engineering*, 3(2), 269-289.

Launder, B.E. (1978). "Heat and Mass Transport" in Turbulence, Chapter 6, Bradshaw, Ed., Springer-Verlag, Berlin.

Lawler, D.F., and Singer, P.C. (1993). “Analyzing disinfection kinetics and reactor design: a conceptural approach versus the SWTR.” *J. Am. Water Works Assoc.* 85, 67-76.

Leonard, A. (1974). “Energy cascade in large eddy simulations of turbulent fluid flows.” *Adv. Geophys*., 18A, 237.

Leonard, B.P. (1979). “A stable and accurate convection modeling procedure based on quadratic upstream interpolation.” *Comput. Meth. Appl. Mech. Engrg.*, 19, 59-98.

Levenspel, O. (1972). *Chemical Reaction Engineering*, 2nd Edition, John Wiley and Sons Inc., New York.

Lilly, D.K. (1966). “On the application of the eddy viscosity concept in the inertial sub-range of turbulence.” NCAR Manuscript No. 123, National Center for Atmospheric Research, Boulder, CO.

Lilly, D.K. (1992). “A proposed modification of the Germano subgrid-scale closure method.” Phys. Fluids A, 4(3), 633-635.

Mason, P.J. and Callen, N.S. (1986). “On the magnitude of the subgrid-scale eddy coefficient in large-eddy simulations of turbulent channel flow.” *J. Fluid Mech.*, 162, 439-462.

Murrer, J., Gunstead, J., and Lo, S. (1995). “The development of an ozone contact tank simulation model.” *Ozone-Sci. Eng.*, 17(6), 607-617.

Nekrasov, P.A. (1885) The Lagrange series and approximate expressions of functions of very large numbers. MS. 12, 49-188.

Nezu, I. and Nakagawa, H. (1993). *Turbulence in open channel flows.* Balkema, Rotterdam, The Netherlands.

Oertel, H. and Laurien, E. (1995). Numerical Stroemungsmechanik. Springer Verlag. Berlin, Heidelberg, New York, Tokyo.

Olsen, N.R.B. (2005). SSIIM User's Manual. Department of Hydraulic and Environmental Engineering, The Norwegian University of Science and Technology. <http://www.ntnu.no/~nilsol/ssiimwin/manual3.pdf>

Peaceman, D.W. and Rachford, H.H. (1955). "The Numerical Solution of Parabolic and Elliptic Differential Equations." J. Soc. Indust. Appl. Math. 5(1), 28-41.

Piomelli, U., Moin, P., and Ferziger, J.H. (1988). "Model consistency in large eddy simulation of turbulent channel flows." Phys. Fluids, 31(7),

Pope, S. B. (2005). *Turbulent Flows*, Cambridge University Press*, Cambridge, UK*, 219-249, 581-582.

Prandtl, L. (1920). "Uber die Harte plastischer Korper." Nachr. Ges. Wissensch, Gottingen, math.-phys. Klasse, 74-85.

Rebhun, M. and Argaman, Y. (1965). "Evaluation of Hydraulic Efficiency of Sedimentation Basins." *J. Sanit. Eng. Div.*, 91(SA5), 37

Rodi, W. (1980). Turbulence Models and Their Application in Hydraulics. A State of the Art Review. Presented by the IAHR-Section on Fundamentals of Division II: Experimental and Mathematical Fluid Dynamics, Delft, Netherlands.

Rodi, W., Ferziger, J. H., Breuer, M., Pourquie, M. (1997). "Status of large eddy simulation: results of a workshop." *ASME Journal of Fluids Engineering*, 119(2), 248-262.

Rogallo, R.S., and Moin, P. (1984). "Numerical simulation of turbulent flows." *Annu. Rev. Fluid Mech.,* 16, 99-137.

Roustan, M., Beck, C., Wable, O., Duguet, J.P., and Mallevialle, J. (1993) "Modeling hydraulics of ozone contactors." *Ozone-Sci. Eng.*, 15(3), 213-226.

Ruether, N. and Olsen. N.R.B. (2005). "Three dimensional modeling of sediment transport in a narrow 90° channel bend", *ASCE Journal of Hydraulic Engineering*, 131, 917-920.

Schlichting, H. (1979). *Boundary-Layer Theory*. McGraw-Hill.

Sepp, E. (1981). "Optimisation of chlorine disinfection efficiency." *Journal of Environmental Engineering Division, ASCE,* 107,(EEI),139-153.

Shiono, K. and Teixeria, E.C. (2000). "Turbulent characteristics in a baffled contact tank." *Journal of Hydraulic Research*, 38(6), 403-416.

Smagorinsky, J. (1963). "General circulation experiments with the primitive equations, part I: The basic experiment," *Mon. Weather Rev.*, 91(3), 99-164.

Spalding, D.B. (1972). "A novel finite-difference formulation for differential expressions involving both first and second derivatives." *Int. J. Num. Methods Eng.*, 4, 551.

Stoesser, T. and Nikora, V.I. (2008). "Flow s structure over square bars at intermediate submergence: Large Eddy Simulation study of bar spacing effect." *Acta Geophysica*, 56(3), 876-893 (2008).

Stoesser, T., Ruether, N. and Olsen, N.R.B. (2009) "Calculation of Primary and Secondary Flow and Boundary Shear Stresses in a Meandering Channel", Advances in Water Resources, doi:10.1016/j.advwatres.2009.11.001.

Stone, H.L. (1968). "Iterative Solution of Implicit Approximations of Multidimensional Partial Differential Equations." *SIAM Journal on Numerical Analysis*, 5(3), 530-558.

Sturm, T.W. (2010). Open Channel Hydraulics, 2nd Ed. McGraw Hill, 504.

Tang, G., Adu-Sarkodie, K., Kim, D., Kim, J.H., Teefy, S., Shukairy, H.M., and Mariñas, B.J. (2005) "Modeling Cryptosporidium parvum oocyst inactivation and bromate formation in a full-scale ozone contactor." *Environ. Sci. Technol.*, 39(23), 9343-9350.

Tominaga, Y. and Stathopoulos, T. (2007). "Turbulent Schmidt numbers for CFD analysis with various types of flow field." *Atmospheric Environment*, 41, 8091-8099.

USEPA (1986) "Design Manual: Municipal Wasterwater Disinfection." EPA-625-1-86-021.

USEPA (1991). "Guidance manual for compliance with the filtration and disinfection requirements for public water systems using surface water sources. Washington.

USEPA (1999). "Disinfection profiling and benchmarking guidance manual, Appendix A." EPA-815-R-99-013.

Van der Walt, J.J. and Haarhoff, J. (2000). "Is a reservoir really that simple? A CFD investigation into the internal hydraulics of reservoirs." Proceedings of WISA 2000 conference, Sun City, South Africa

Versteeg, H.K., and Malalasekera, W. (2007). *An Introduction to computational fluid dynamics: The finite volume method*, Pearson Education Limited, England, 273-275.

Wang, H., and Falconer, R. A. (1998a). "Simulating disinfection processes in chlorine contact tanks using various turbulence models and high-order accurate difference schemes." *Water Res.*, 32(5), 1529-2543.

Wang, H., and Falconer, R. A. (1998b). "Numeri.cal modeling of flow in chlorine disinfection tanks." *J. Hydraul. Eng.-ASCE,* volume(issue), 918-931

Willimson, J.H. (1980). "Low-Storage Runge-Kutta Schemes." Journal Comp. Phys., 35, 48-56.

Wilson, C.A.M.E., Stoesser, T, Olsen, N.R.B., and Bates, P.D. (2003). "Application and Validation of Numerical Codes in the Prediction of Compound Channel Flows." Proceedings of the Institution of Civil Engineers, UK, Water and Maritime Engineering, No. 153, 117-128.

Wols, B.A., Uijttewaal, W.S., Rietveld, L.C., Stelling, G.S., van Dijk, J.C., and Hofman, J.A.M.H. (2008). "Residence Time Distributions in Ozone Contactors", *Ozone-Sci. Eng.*, 30(1), 49-57.

Wols, B.A., Shao, L., Uijttewaal, W.S., Hofman, J.A.M.H., Rietveld, L.C., and van Dijk, J.C. (2010). "Evaluation of experimental techniques to validate numerical computations of the hydraulics inside a UV

Zhang, J., Huck, P.M., Anderson, W.B., and Stubley, G.D., (2007). "A Computational Fluid Dynamics Based Integrated Disinfection Design Approach for Improvement of Full-scale Ozone Contactor Performance", *Ozone-Sci. Eng.*, 29(6), 451-460.

Zhu, J. (1991). "A low diffusive and oscillation-free convection scheme." *Commun. Appl. Numer. Methods*, 7, 225-232.

VITA

Dongjin Kim was born in Daejeon in South Korea. He received a B.S. degree in Automotive Engineering from Keimyung University in 2000 and a M.S. degree in Mechanical Engineering from Kyungpook National University in 2002, both located in Daegu, South Korea. Prior to joining Georgia Tech to pursue a doctorate in Civil and Environmental Engineering in 2007, he worked at Korea Powertrain Company in Advanced Research and Development Team as an Automotive Torque Converter developer for four years. His research was focused on the numerical simulation of turbulent flows and solute transport in an ozone contactor using steady/unsteady Reynolds-Averaged Navier-Stokes Simulation and Large Eddy Simulation codes.